Mechanical Properties of Coating Materials for Use in the Mirrors of Interferometric Gravitational Wave Detectors

Matthew Robert Abernathy

School of Physics and Astronomy

Institute for Gravitational Research

University of Glasgow

Contents

List of Figures

List of Tables

To begin, I would like to thank my supervisors, Professors Sheila Rowan and Jim Hough for their excellent guidance throughout my Ph.D. program. I had an excellent time studying in Glasgow, and I would not have had the opportunity to do so without their generous support. I would also like to thank Dr. Iain Martin for his guidance and support as both an advisor and friend.

The work presented in this thesis was carried out under a studentship by the Scottish Universities Physics Alliance (SUPA). I am very thankful to SUPA and to the director of the SUPA graduate school, Mrs. Avril Manners, for granting me this opportunity.

I offer my thanks to all of the Institute of Gravitational Research (IGR) for the great times and informative discussions, and for all the friends I have made. I would especially like to thank my office mates, Paul Campsie, Nicola Beverage, Riccardo Bassiri, Karen Haughian, Keith Evans, Kieran Craig, Chris Bell, Rahul Kumar, and Peter Murray, for all the good times and distracting conversations we've had over the years. I enjoyed the discussions and pranks from the early days in 461 with Paul and Nicola, all the way through the noisier times in 427A.

The list of members in the IGR that I would like to thank are too long to list, but I will include a few more names: first of all, Jean Greig, without whom nothing would ever get done; Jamie Scott and Brian Barr, the two friendliest port drinkers I know; Craig Lawrie, who's always game for some football talk; and Nacho Santiago Prieto for being a good friend who commiserates with me about being away from North America. I should also thank Liam Cunningham, Alan Cumming, and Stuart Reid, both for their help in the lab, and for just generally being good guys.

The people outside the office, but still in Glasgow, who have given me the most support include my fellow football players. I'll thank Euan Bennet for organizing the games, and probably taking a big hit to the wallet for it. Also Gail Penny, who I'm certain doesn't collect enough money for all the games she puts together. Fraser Watson is the best goalie I've ever played with. Eric

Yao is pretty good at scoring goals when he's having a good day, but he's always fun to play with. Colin Gill doesn't play much anymore, but when he does he's both fun and dangerous. The same goes for Satoru Sakai, but with less danger. Others I've already mentioned above for other reasons, and still others I can't be bothered to write down. In any case, thanks to all of my Glaswegian friends and team mates for making my time in Glasgow so great.

Finally, I want to thank the people in my personal life that have supported me for so long. Thank you to my parents, Richard and Linda Abernathy, for raising me to be such an upstanding gentleman. Thank you to my brother, Patrick Abernathy, for being an even greater influence on my development. Thank you to Mary Hempel and her entire family, for being such wonderful friends. And thank you to Vincent Henning for being my best friend in the entire world, and for keeping me company on the phone no matter where I am. I would also like to thank all of my friends from MIT for staying in touch and having a great time whenever we get together: in no particular order; Levi Lalla, Jay Miller, Nicola Tan, Mike Berry, Kenall Werts, Phil Janowicz, and Kavitha Kadambi. Everybody mentioned, and many who have not been mentioned, have helped to make me who I am today, and for that, I am especially thankful.

Preface

This thesis is an account of work carried out in the Institute for Gravitational Research at the University of Glasgow between October 2008 and May 2012, involving studies of the mechanical properties of optical materials for use in future gravitational wave detectors.

Chapter 1 presents an introduction to gravitational waves and their detection. The science aims of the gravitational wave detection community are discussed, and current and future gravitational wave detectors are introduced.

In chapter 2, thermal noise is discussed as a limiting noise source to second-generation detectors. The dependence of thermal noise in interferometric gravitational wave detectors upon the mechanical properties of the optical coatings is introduced.

Chapter 3 presents characterization of cryogenic mechanical loss measurements and measurements of the mechanical loss of hafnium dioxide coatings. These experiments were carried out at the suggestion and under the guidance of Prof. Sheila Rowan and Dr. Iain Martin. Some mechanical loss measurements of samples SN1, SN8, and SN 10 were made by Dr. Stuart Reid and Dr. Eleanor Chalkley. Data-taking software was written by Dr. Ronny Nawrodt. Measurements of the coating structure were made by Dr. Riccardo Bassiri with the assistance of Mr. Keith Evans and Dr. Ian MacLaren.

Chapter 4 presents measurements of the mechanical loss of Ti-doped tantalum pentoxide coatings. These experiments were carried out at the suggestion and under the guidance of Prof. Sheila Rowan and Dr. Iain Martin. Measurements were made with the assistance of Dr. Iain Martin, Mr. Kieran Craig,

and Dr. Stuart Reid.

Chapter 5 presents measurements of the Young's modulus of various thin films using nano-indentation. Measurements were made with the assistance of Dr. Michelle Oyen and her students: Mr. Oliver Hudson, Mr. Daniel Strange, and Ms. Tamaryn Shean. Samples were measured using a Hysitron TI-700 Ubi, operated by the group run by Dr. Michelle Oyen at the University of Cambridge. Measurments and analysis were also done with the assistance of Ms. Courtney Linn.

Chapter 6 presents the development of a technique for determining the Young's modulus, thermal expansion coefficient, and Poisson's ratio of various thin films. These measurements were undertaken at the advice of Prof. Sheila Rowan. Development of the experiment and measurements were done with the assistance and guidance of Prof. Jim Hough and Prof. Jim Faller. Measurements were made with the assistance of Miss Courtney Linn, Mr. Zachary Pierpoint. Mr. Ross Wilson and Mr. Chris Moeller reconstructed the apparatus, made additional measurements, and began the finite element modelling.

Chapter 7 concludes the thesis with a discussion of the results herein and their relationships to one another and relevance for gravitational wave detection.

Summary

Gravitational waves are fluctuations in the curvature of space-time predicted by the theory of General Relativity to result from an asymmetric acceleration of mass. These changes in the gravitational field propagate outward at the speed of light. As the gravitational field strength is weak compared to the other fundamental forces, the only gravitational waves that may be detected here on Earth arise from the movements of dense astronomical systems such as coalescing black holes and neutron stars, and rapid accelerations of large masses, such as in supernovas and rotating neutron stars.

Gravitational waves have yet to be directly detected. However, there is strong evidence for their existence through the success of General Relativity in predicting the observed behaviour of the Hulse-Taylor binary pulsar, whose orbit has been shown to be decaying in a manner consistent with energy being lost through the radiation of gravitational waves. This evidence was enough to win Hulse and Taylor a Nobel Prize, and to provide a strong basis on which to search for gravitational waves using a number of gravitational wave detectors worldwide.

One of the most promising methods for detecting gravitational waves involves the use of large-baseline interferometric gravitational wave detectors. These detectors use Modified Michelson-type interferometers with arms ranging from several hundred metres to a few kilometres in length in order to detect the asymmetric strains in space caused by the passage of a gravitational wave. There are currently four kilometre-scale interferometric gravitational-wave de-

tectors in the world: two four-kilometre detectors in the United States (LIGO), one three-kilometre detector in Italy (Virgo), and the Geo 600 detector in Germany, which has 600-metre arm cavities with a folded-arm configuration, giving it an effective 1.2-km arm length. These detectors are all undergoing upgrades to increase their sensitivities, and there are more detectors which are expected to come online within the next decade. Chapter 1 gives an overview of the field of gravitational wave detection with a focus on interferometric gravitational wave detectors.

There are a number of noise sources which limit the sensitivity of the detectors, of different relative significance in different frequency ranges. At low frequencies, up to a few tens of Hertz, one of the most significant noise sources is seismic noise from the surrounding environment coupling into the detectors. At higher frequencies, from a few hundred Hertz and upwards, the detectors are limited by statistical and quantum noise sources, and at mid-frequencies, from a few tens of Hertz to a few hundred Hertz, the detectors are limited by thermal noise. Chapter 2 contains a discussion of thermal noise in interferometric gravitational wave detectors.

Thermal noise arising from the materials used in making the mirror-test masses is the limiting noise source in the most sensitive frequency band of the detectors. Understanding and reducing thermal noise is of utmost importance in improving the sensitivity of large-baseline interferometric gravitational wave detectors. The research presented in this thesis covers the measurement of material properties that are necessary for both calculating the thermal noise contribution of mirror-coating materials and understanding the mechanisms contributing to this thermal noise, mainly mechanical loss of the materials, their Young's moduli, and coefficients of thermal expansion.

First generation interferometric gravitational wave detectors use mirrors composed of fused-silica substrates coated with multiple ion-beam-sputtered (IBS) layers of alternating silica ($Si0_2$) and tantala (Ta_2O_5). Research has

shown that the mechanical loss of these mirrors arises predominantly in the tantala layers, and that doping the tantala with titania (TiO_2) can reduce the mechanical loss by as much as 40%. Further research indicates that the titania dopant acts to increase the activation energy of the loss mechanism in tantala, therefore making it less likely to be activated, and reducing loss. However, the actual loss mechanism is not yet fully understood.

Second generation detectors currently being built will utilize tantala layers doped with 25% titania (by cation) to reduce thermal noise. However, the interferometers will still be limited by coating thermal noise, and future detectors will need even further reductions. It is therefore necessary to understand the mechanical loss mechanisms in titania-doped tantala in order to seek ways of reducing mechanical loss even further, and to evaluate alternative optical materials that might intrinsically have lower loss. Measuring the mechanical loss of materials at cryogenic temperatures gives insights into the loss mechanisms and is also necessary for ascertaining the usability of the materials in planned future cryogenic detectors.

Chapters 3 and 4 cover mechanical loss measurements of IBS hafnia (HfO_2) and of 25 and 55% titania-doped tantala coatings at cryogenic temperatures. Hafnia is a promising alternative to tantala as a high index-of-refraction optical coating in gravitational wave detectors. As such, its mechanical loss must be understood before it can be considered in future designs. Additionally, hafnia is an amorphous metal-oxide like tantala and silica, and knowledge of its loss may contribute to a general theory of mechanical loss in these materials. Post-deposition heat-treatment has been shown to affect the mechanical loss of tantala, so the loss of hafnia has been measured on a number of hafnia samples with different heat-treatments in order to investigate the effects on hafnia. The titania-doped tantala samples were not heat-treated, as measurements of as-deposited titania-doped tantala have not been previously made. The wide variation in doping concentration was selected in order to better understand

the effects of doping on the mechanical loss. The results indicate that hafnia can have lower loss than tantala at temperatures below ∼100 K, even when the hafnia coating is partially crystalline, a state which has been shown to cause excess loss in tantala. The measurements of mechanical loss in the titania-doped tantala samples gave similar losses for both samples, but a large difference in the activation energy or the loss mechanism due to the different doping concentrations.

The room temperature Young's modulus of amorphous IBS coatings were measured using nanoindentation, as documented in chapter 5. Knowledge of the Young's modulus of a coating material is necessary for the proper extraction of the coating mechanical loss from the measurements made in chapters 3 and 4. The Young's modulus is also necessary for the calculation of thermal noise in the interferometer from the measured mechanical loss. It is therefore important that Young's modulus be accurately known. The Young's moduli of IBS coatings are often different from those of the bulk materials, and in some cases, the materials may not even exist in a bulk form, so it is necessary to measure them directly from the coatings. Given the small coating thicknesses involved, nanoindentation is one of the few methods available for directly measuring these values. The Young's modulus of undoped tantala and titania-doped tantala coatings as a function of post-deposition heat-treatment are measured in chapter 5. The results indicate that heat-treatment has a measurable effect on the Young's modulus which is dependant upon the titania concentration. The moduli of hafnia and amorphous silicon coatings are also measured.

Another method of measuring Young's modulus, along with coefficient of thermal expansion and Poisson's ratio of coating materials is through the measurement of stress in the coating/substrate system brought about by deposition and thermal mismatch effects. Coefficient of thermal expansion and Poisson's ratio are also important parameters used in the calculation of various compo-

nents of the thermal noise in an interferometer, so it is important that they are directly measured. It has been postulated that the mechanical loss may be influenced directly by the stress in the coatings, so the stress measurement may be a valuable component of future analyses. Chapter 6 describes the development of an apparatus for making stress measurements on coated cantilevers by measuring the curvature of the cantilever after the coating has been applied. The stress measurements, combined with the Young's moduli measured in chapter 5, are used to calculate the coefficient of thermal expansion as a function of post deposition heat-treatment for IBS hafnia and for tantala doped with 25 and 55% titania. The results indicate that heat-treatments of the type studied here appear to have no significant effect on the coefficient of thermal expansion in the doped-tantala samples, but the coefficient of thermal expansion of the hafnia samples show a dependence on heat treatment.

Chapter 1

Gravitational Wave Detection

Gravitational waves were first postulated by Einstein as a consequence of his General Theory of Relativity [1]. The force of gravity can be thought of as a curvature in space-time brought about by the presence of mass, where any asymmetric acceleration of masses should produce fluctuations in the curvature of space-time with these gravitational waves propagating at the speed of light. However, due to the relatively weak nature of gravitation, only large masses and accelerations like those found in certain astrophysical events are likely to create waves of detectable amplitude [2].

The first attempts to detect gravitational waves were made in the 1960's by Joseph Weber [3]. Weber used resonant bar detectors—long aluminium bars whose resonant modes might be excited by a passing gravitational wave. His early claims of discovery brought great interest to the field of gravitational wave detection, but were eventually found to be unreproducible [4]. Interest in the field, however, remains, and has given rise to more advanced detector designs.

Most current gravitational wave detectors use a kilometre-scale Michelson interferometer design with Fabry-Perot arm cavities. These interferometers are designed to measure the separation between widely separated masses with phenomenal accuracy: measuring length differences as small as 10^{-19} metres over 4 kilometres. As a gravitational wave passes through an interferometer,

travelling perpendicular to the two arms, one arm will get shorter and the other arm will get longer; the resulting change in the interference pattern shows the change in relative lengths of the arms.

A number of these detectors have been built throughout the world. In Washington state in the US, there is one 4km long interferometer and until recently, one 2km long interferometer, and in Louisiana state, there is another 4km long interferometer. These detectors are collectively called The Laser Interferometer Gravitational Wave Observatory (LIGO) [5]. After completing a number of science runs, they are currently being upgraded to more advanced designs, called Advanced LIGO. There is also the 3 km Virgo detector located in Italy [6] which will soon be upgraded to form the Advanced Virgo system. The UK and Germany are partners in the GEO600 project, which has a 600m arm length, but with a folded arm design that doubles its effective arm length [7]. The GEO600 interferometer is currently being upgraded (GEO-HF) which will make it more sensitive at higher frequencies [8]. In addition, there is TAMA, in Japan, which has 300 metre arms, and has made contributions to the search for gravitational waves [9]. These detectors all make scientific contributions as well as paving the way for future detectors such as the planned Einstein Telescope (ET) [10] and the Large-scale Cryogenic Gravitational wave Telescope (LCGT) [11], recently renamed KAGRA [12].

1.1 Introduction

The detection of gravitational waves is one of the greatest scientific pursuits today. The fluctuations in the fabric of space brought about by gravitational waves are so small that the technology needed to detect them is only now coming to maturity. Once detected, gravitational waves will open a new window on the universe. Unlike electromagnetic radiation, gravitational radiation is largely unaffected by matter due to it's low interaction cross-section [13]. This means that gravitational waves are not blocked by dust clouds or intervening

matter. The behaviour of matter inside supernovae and neutron stars may thus be revealed through observations of gravitational waves produced by the accelerations of mass associated with these objects. Through observations of gravitational waves, we expect that General Relativity will be tested at new limits, and the early universe will be further revealed through relic gravitational waves from times even before the emission of the cosmic microwave background radiation.

To date, evidence for gravitational waves exists from the observations of the binary pulsar PSR1913+16 [14], also known as the Hulse-Taylor binary pulsar, as well as from the many successful tests of General Relativity that have been carried out ([15] and sources therein). These do not directly confirm the existence of gravitational waves, but do strongly confirm the theory which predicts them. Hulse and Taylor were rewarded the Nobel prize in physics in 1993 for their observations of the pulsar system and for demonstrating that its orbit is decaying exactly as predicted by the emission of gravitational waves under General Relativity.

Since this discovery, numerous projects have been advanced in the hopes of a direct detection. Some of the most promising detectors are those based on interferometric techniques. These detectors use km-scale modified Michelson interferometers in order to detect the extremely small changes in the lengths of the interferometer arms, caused by the passage of a gravitational wave. They have been combined as part of a global collaboration, along with dozens of institutions and hundreds of researchers with the goal of successfully detecting gravitational waves in the near future.

This chapter presents the theory of gravitational waves and some of the core technical aspects of gravitational wave detectors. The current status of interferometric gravitational wave detection will also be discussed.

1.2 Gravitational Waves and Their Production

This section introduces the fundamental physics behind gravitational waves including their derivation and effects. This section also contains a description of possible astrophysical sources of gravitational waves, including pulsars, black hole binaries, neutron star binaries, supernovae, and asymmetric neutron stars.

1.2.1 Nature of GW Radiation

Gravitational radiation is a natural consequence of General Relativity. Just as electromagnetic radiation is created by acceleration of charge, gravitational radiation is produced by the acceleration of mass. In electromagnetic radiation, a dipole moment can exist because there are two electric charges. In gravitational radiation, there is only one charge of mass, so a dipole moment is not allowed through the conservation of momentum. The conservation of mass disallows any odd-numbered polarities, so the only allowed polarities are even-numbered and greater than $n = 2$. It is generally assumed that most gravitational radiation would be emitted at the simplest polarity, so gravitational waves are expected to be quadrupolar [16].

This implies that gravitational waves can only be generated by an asymmetric acceleration of mass, such as the orbits of binary objects or the rotation of non-spherical bodies. In these cases, the gravitational radition would be emitted at twice the natural frequency of the system.

The effect of a passing gravitational wave on two adjacent free-falling masses, separated by a distance L and oriented perpendicular to the wave's direction of travel, is to change their separation by a distance, ΔL, such that the amplitude of the wave (h) is

$$h = \frac{2\Delta L}{L}. \tag{1.1}$$

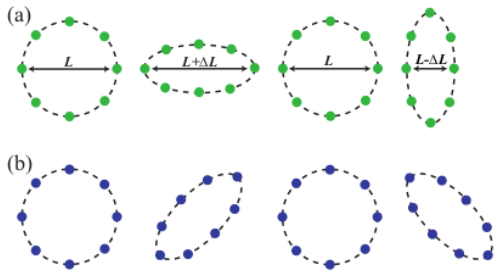

Figure 1.1: The effects of a gravitational wave travelling perpendicular to the page on a ring of free-falling test particles. a) The h_+ polarization. b) The h_x polarization (Image from [17]).

The quadrupolar nature of the gravitational wave can be more clearly seen by the effect of a wave passing through a ring of free-falling masses, like that seen in figure 1.1. This figure also illustrates the two possible polarizations of a quadrupolar gravitational wave–the x and $+$ polarizations–each rotated 45^o from the other. As the gravitational wave travels in the direction perpendicular to the ring of particles, it causes a positive change in length in on direction and a negative change of length in the perpendicular direction, showing the quadrupolar nature of the oscillation.

1.2.2 Sources of GW Radiation

In [18], the authors consider a man-made source of gravitational radiation. It quickly becomes clear that earthbound sources of detectable gravitational radiation are implausible. The authors calculate the gravitational wave amplitude for a rotating beam 10 m long with a 10^3 kg mass at each end. If the rotational frequency of the beam is 10 Hz, the frequency of the gravitational radiation will be at 20 Hz, since the mass distribution is equal at every half-rotation. At a distance greater than one wavelength from the source, the calculated gravitational wave amplitude is on the order of $h \sim 10^{-43}$! At this point it is obvious why Einstein did not believe that gravitational waves would ever be detected.

Fortunately, the terrestrial limits placed on man-made experiments do not hold in the astrophysical laboratory. There are a number of astrophysical

sources with orders-of-magnitude larger masses, densities, velocities, and accelerations than anything available on earth. So much so, that even though they are also orders-of-magnitude farther away from earth-bound detectors, it is expected that these sources will produce detectable levels of gravitational radiation. This section lists some of the more promising and well-understood astrophysical sources of gravitational radiation. Of course the greatest excitement may come with the detection of unexpected sources, which could lead to a whole new understanding of the universe.

1.2.2.1 Compact Binaries

Compact binary systems are much like the man-made device imagined above, only on a much larger scale. In this case, two dense stellar remnants, two black holes (BHBH), two neutron stars (NSNS), or a black hole/neutron star pair (NSBH), orbit each other at such a close distance that a significant amount of their orbital energy is radiated as gravitational waves. An example of this sort of system is the Hulse-Taylor binary pulsar, PSR1913+16, discussed above.

Following [19], a compact binary a distance R away from Earth should produce a strain amplitude at Earth of

$$h_{binary} \sim 10^{-23} \left(\frac{100 \text{ Mpc}}{R}\right) \left(\frac{M_b}{1.2 \text{ M}_\odot}\right)^{\frac{5}{3}} \left(\frac{f}{200 \text{ Hz}}\right)^{\frac{2}{3}}, \tag{1.2}$$

where f is the frequency of the orbit and M_b is the binary mass parameter:

$$M_b = \frac{(M_1 M_2)^{\frac{3}{5}}}{(M_1 + M_2)^{\frac{1}{5}}}, \tag{1.3}$$

and M_1 and M_2 are the masses of the two compact objects. Of course, as energy is lost to gravitational radiation, the orbits will shrink and the frequency will increase as

$$f(t) \approx 2.1 \text{ Hz} \times \text{M}_\text{b}^{\frac{5}{8}} \left(\frac{1 \text{ day}}{\tau}\right)^{\frac{3}{8}}, \tag{1.4}$$

where τ is the time until the objects 'collide' [2]. This effectively produces a 'chirp', wherein the frequency and amplitude of the gravitational wave signal increases until the objects collide, releasing more complicated signals caused by the merger and ring-down of the excited resonant modes of the resulting body [20].

It is this 'chirp' which is expected to fall within the sensitivity range of ground-based detectors, when the frequency is between 10 and 1000 Hz, and the strain amplitude for the average source is expected to be as much as $h \sim 10^{-21}$. These signals are promising because the inspirals are relatively well understood, and they can be filtered from the noise in the detector using a matched filtering technique [21], allowing the detection of even fainter signals than other sources. Additionally, as the waveforms can be so accurately modelled, they can be used as standard candles for determination of the Hubble Constant, requiring only the redshift of the host galaxy as additional information [19].

1.2.2.2 Gravitational Collapse

The formation of the compact objects discussed above can sometimes produce a measurable gravitational wave signal. These objects are formed by the gravitational collapse of a highly evolved star or the core collapse of an accreting white dwarf, such as in a type II supernova. If the collapse is not spherically symmetric, perhaps from strong rotation, a fraction of the energy can be released as gravitational waves.

To date, the physical mechanisms of gravitational collapse are not fully understood, and models to predict even the electromagnetic signatures of supernovae are computationally intensive and have numerous uncertainties. However, there are some simulations that suggest that between 10^{-5} and 10^{-7} of the total available mass-energy may be radiated as gravitational waves in the frequency range of ground-based detectors [22; 23].

If one assumes the energy released as gravitational waves during a gravitational collapse (E), the gravitational strain at frequency f, measured at a

distance R can be approximated as

$$h \sim 6 \times 10^{-21} \left(\frac{E}{10^{-7}\ \mathrm{M}_\odot} \right)^{\frac{1}{2}} \left(\frac{1\ \mathrm{ms}}{T} \right)^{\frac{1}{2}} \left(\frac{1\ \mathrm{kHz}}{f} \right) \left(\frac{10\ \mathrm{kpc}}{R} \right), \tag{1.5}$$

where T is the elapsed time of the collapse [18]. For reasonable estimates, this is within the detection sensitivity of ground-based detectors; however, the event rate is less than one event per two decades within the Milky Way and local group. If the reach of the detectors were to cover a few megaparsecs, one might expect a rate of about 0.5 per year: a reasonable expectation for advanced detectors [24].

1.2.2.3 Neutron Stars

A neutron star without a compact partner can also be a source of gravitational waves. Much of the angular momentum of the neutron star's progenitor is retained by the neutron star, only with a much reduced moment of inertia, so the neutron star's angular velocity can be very large. If there is a non-axisymmetric mass distribution, the rotational energy can be radiated away in the form of gravitational waves.

Non-axisymmetric mass distributions could develop on a neutron star in a number of ways. After a violent formation, the neutron star's internal modes may be excited, and these deformations may be frozen into the surface as it cools and forms a crust [25; 26]. Additionally, a young neutron star may posses a strong magnetic field, which may not be aligned with the spin-axis. This would produce bulges at the magnetic poles [27]. Finally, the neutron star could be a member of a low mass x-ray binary (LMXB) where the neutron star's companion is a main sequence or red giant which has overfilled its Roche lobe and deposits matter onto the neutron star. The accreted matter would add angular momentum and 'spin-up' the neutron star and simultaneously contribute to any asymmetry [28].

The strain amplitude of such a spinning neutron star can be approximated as,

$$h \approx 6 \times 10^{-25} \left(\frac{f_{\text{rot}}}{500 \text{ Hz}}\right)^2 \left(\frac{1 \text{ kpc}}{d}\right) \left(\frac{\epsilon}{10^{-6}}\right) \tag{1.6}$$

where ϵ is the equatorial ellipticity, d is the distance at observation, and f_{rot} is the rotational frequency of the neutron star [29]. For a neutron star in free-precession, i.e. where the axis of symmetry is different from the axis of rotation[30], the strain amplitude can be calculated as:

$$h = 10^{-27} \left(\frac{\theta_w}{0.1}\right) \left(\frac{1 \text{ kpc}}{d}\right) \left(\frac{\nu}{500 \text{ Hz}}\right)^2. \tag{1.7}$$

In this case, θ_w is the amplitude of the free precession in radians, and ν is the frequency of precession.

The gravitational wave amplitudes from such single neutron star emitters seems quite low; however, the signal is continuous and can be coherently summed over long periods of observation. This makes spinning neutron stars interesting sources of gravitational waves. Studies of recent data runs by the LIGO, Virgo, and GEO600 detectors have been able to place experimental limits on the emission of gravitational waves from several nearby pulsars [31; 32; 33], in many cases beating the theoretical limits placed by electromagnetic observations.

1.2.2.4 Stochastic Background

It is expected that there will be a stochastic background of gravitational radiation from random, unresolved sources, and from events early in the universe, such as the big bang. A number of possible sources and detection mechanisms are discussed in [34] and [35]. Relic gravitational waves could come from as early as 10^{-35} seconds after the big bang, and those made just 10^{-25} seconds after the big bang would be red-shifted into the frequency band of today's

ground-based detectors. The expected strain amplitude would be,

$$h \approx 4 \times 10^{-22} \sqrt{\Omega_{\rm gw}} \left(\frac{f}{100 \text{ Hz}} \right)^{-\frac{3}{2}} \text{ Hz}^{\frac{1}{2}}. \tag{1.8}$$

Here, $\Omega_{\rm gw}$ is the energy density required for a closed universe. The only observational limit on $\Omega_{\rm gw}$ is that it must be less than 10^{-5} in order to agree with big bang nucleosynthesis [36]. The most direct way to detect a stochastic background is by correlating output between multiple detectors, separated enough as to have uncorrelated instrument noise.

1.3 Interferometric Gravitational Wave Detectors and Their Limits

As discussed in 1.2.2, gravitational waves are expected to produce minute strains in space over a broad frequency band. A promising detector would offer broadband sensitivity with extremely low noise. Just such an apparatus was suggested by Gertsenshtein and Pustovoit in 1962 [37] in the form of a laser interferometer. Other researchers also developed the idea, independent of one another, including Pirani [38] and Weiss [39]. Laser interferometers are very sensitive to changes in the length of their arms, and since gravitational waves produce a strain in space, interferometers, up to some limit, can be made more sensitive by increasing the length of their arms.

Modern gravitational wave interferometers are based on an enhanced Michelson-type topology. A basic Michelson interferometer can be seen in Figure 1.2. A laser beam is split in two at the beam splitter, travels down both perpendicular arms, and is reflected back towards the beam splitter by the end mirrors. The beams are recombined at the beam splitter, and the resultant interference pattern is sensed using the photodetector at the output port. If the end mirrors are freely suspended, a passing gravitational wave would shorten one arm and

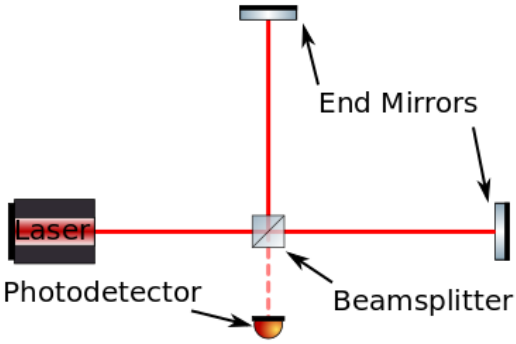

Figure 1.2: A basic Michelson interferometer. The laser beam is split by the beamsplitter, reflects off the end mirrors, and recombines at the beamsplitter. The interference pattern is observed at the photodetector.

lengthen another, altering the interference pattern at the output port.

The sensitivities of long-baseline interferometers to the passage of gravitational waves are limited by a number of fundamental noise sources, such as quantum noise, gravitational gradients, and thermal noise. These noise sources are discussed below, along with enhancements to the basic Michelson interferometer design which are used to reduce these noise sources in advanced detectors.

1.3.1 Limits to Detectors

Interferometric gravitational wave detectors are effected by a number of noise sources. Many of them are of a technical nature. For an introduction to basic interferometry and noise sources, see [2], [40], and references therein. The noise sources discussed in this section are those especially relevant to advanced detectors and in many cases are fundamental limiting sources.

1.3.1.1 Seismic Noise

The surface of the Earth is a noisy place, especially if one is looking to detect movements on the order of 10^{-20} metres. Noise at frequencies below 1 Hz is dominated by natural sources such as ocean waves and large-scale meteorological phenomena. Around 1 Hz, smaller meteorological effects add to the noise,

such as wind and smaller storms, and above 1 Hz, seismic noise is dominated by 'anthropogenic noise', noise caused by people. Such anthropogenic noise includes movements of people and vehicles around the site. Even a quiet site on the surface will have a noise spectrum close to $10^{-7}\ f^{-2}$ m/Hz$^{1/2}$ in each direction [2]. At 30 Hz, this is a factor of 10^9 greater than that required for gravitational wave detection. This noise certainly needs to be eliminated in the horizontal direction, but as there is often a level of coupling between vertical and horizontal motion, seismic noise in the vertical direction needs to be damped as well.

Fortunately, there is a fairly simple technique for isolating the detector from seismic noise; namely, the simple pendulum. It is well known that above the resonance of the simple pendulum, the transfer function for horizontal motion of the mass falls as frequency$^{1/2}$ [41]. Isolation in the vertical direction can be similarly reduced by suspending the mass from a spring. By appropriately choosing the resonant frequencies of the respective pendulums and springs and placing them in series, the effects of seismic noise on the motion of the interferometer mirrors can be reduced to below the level of motion expected from astrophysical gravitational waves. Each of the existing interferometric gravitational wave detectors has a different arrangement of springs and pendulums. For a discussion of each detector, see section 1.4.

Additional active and low-frequency damping is also employed, in part to further remove very low frequency motions caused by the micro-seismic peak, which can affect the control of the interferometer. This additional isolation can take the form of tall inverted pendulums and reduced-stiffness springs [42], or special mechanical linkages and torsion bars [43]. Active isolation is often in the form of seismometer/actuator feed-forward systems [44; 45].

1.3.1.2 Gravitational Gradient Noise

Gravitational gradient noise, otherwise known as Newtonian noise, is a fundamental source of noise in gravitational wave detectors that limits ground-based

interferometers below ~ 10 Hz. It arises from the direct gravitational coupling between the test masses and mass density fluctuations outside the detector. The dominant source of gravity gradients are expected to come from seismic surface waves, but can arise from any change in mass density around the detector, from people moving near the test masses, to clouds passing overhead [46].

The rms magnitude of the interferometer test mass motion due to gravitational gradients, $\tilde{x}(\omega)$, can be shown to be [47]:

$$\tilde{x}(\omega) = \frac{4\pi G\rho}{\omega^2}\beta(\omega)\tilde{W}(\omega). \tag{1.9}$$

Here, ρ is the density of the Earth near the test mass, G is the gravitational constant, ω is the angular frequency, $\beta(\omega)$ is a dimensionless reduced transfer function that correlates the motion of the interferometer test masses and accounts for the separation of the masses from the Earth's surface, and $\tilde{W}(\omega)$ is the rms-average of the Earth's displacement over all three dimensions. It is impossible to avoid this noise source, as it is a natural consequence of trying to measure gravitational effects; however, it is possible to minimize the effects.

There are three ways to reduce the effects of gravitational gradient noise. To passively reduce the effects, one can simply move to where the noise spectrum is lower. A seismically quiet location is a good start: it has been predicted that gravitational gradient noise can be reduced by going ~ 150 metres underground, where there is less effect from seismic surface waves. This can reduce noise for frequencies down to around 1 Hz [48]. Another way to avoid large gravitational gradients is to go into space, as in the proposed NGO space telescope, the successor to the previously studied LISA gravitational wave detector design [49], currently under assessment by ESA. Finally, the effects may be actively managed using an array of seismometers arranged around the detector to monitor the the relevant ground movement and compression. Given this information, it may be possible to create a subtraction signal to remove the

effects of the noise from the signal data [50].

1.3.1.3 Thermal Noise

Thermal noise is typically the dominant noise source in the most sensitive region of detectors, between a few tens of hertz to a few hundred hertz. This noise arises from the thermally driven motion of the molecules in the test masses, mirror coatings and suspensions. The magnitude of these noise sources in the detection band is related to the intrinsic mechanical loss of the test mass and suspension materials and the level of thermoelastic damping [51].

Thermoelastic noise arises from statistical differences in the temperature of a material. If one section of the material is warmer than another, a temperature gradient is created, and the flow of heat from the warmer to the cooler region becomes a source of loss. If the material is excited by an external force, the temperature difference is created by heating and cooling due to contraction and expansion, but even absent external influences, the natural statistical temperature fluctuations give rise to a thermal noise profile for the material.

Each resonant mode has an average thermal energy of $k_b T/2$ per degree of freedom, as arises from natural thermodynamic processes. This energy cannot be eliminated without reducing the temperature of the masses—a difficult proposition when considering the requirements for seismic isolation. Instead, the masses and suspensions can be designed so that the resonant modes are outside the frequency band where the detector is most sensitive, and materials with low mechanical loss can be chosen so that the thermal energy is concentrated around the resonant mode frequencies. This way, the thermal noise is not eliminated, but moved to a frequency band where its effect on the sensitivity of the detector is minimised.

The thermal noise inherent in the suspensions, test masses, and mirror coatings are all important noise sources in gravitational waved detectors. The use of fused silica for the test masses, and quasi-monolithic suspensions are

partially motivated by the need for reduced thermal noise, as silica has a low thermal noise profile due largely to its low mechanical loss. The mirror coatings, however have a larger contribution to the thermal noise, and they cannot be made entirely of silica. Chapter 2 gives a more detailed description of thermal noise, and especially coating thermal noise.

1.3.1.4 Standard Quantum Limit

The Standard Quantum Limit (SQL) is a fundamental limit, corresponding to the Heisenberg Uncertainty Principle, which limits the sensitivity of interferometric gravitational wave detectors. Classically, it can be understood as the balance between two seemingly unrelated noise sources: Photon Shot Noise, and Radiation Pressure Noise.

Photon Shot Noise: Photon shot noise arises from statistical fluctuations in the number of photons reaching the photodetector at the output port of the gravitational wave detector. Detectors are operated at a 'dark fringe', where the arm lengths are positioned such that the beams cancel at the output. This provides the largest signal to noise for a detection [52]. It also means that only a small number of photons reach the detector at any one time. The number of photons detected will follow Poisson statistics and have an associated $\sqrt{N}$ uncertainty, which gives rise to a limit to detector sensitivity.

The effects of photon shot noise on the strain sensitivity, $h_{\rm shot}(f)$ of a basic Michelson interferometer can be calculated from [53]:

$$h_{\rm shot}(f) = \left(\frac{\pi\hbar\lambda}{2P_{\rm in}\epsilon c}\right)^{\frac{1}{2}} \frac{f}{\sin(\pi f\tau)}. \tag{1.10}$$

Here, $\hbar$ is the reduced Planck's constant, λ is the wavelength of the photons, $P_{\rm in}$ is the input power of the laser, ϵ is the quantum efficiency of the photodetector, c is the speed of light, f is the frequency, and τ is the time that the light is within the detector. It can be seen from this equation that one can reduce

the effects of the photon shot noise on detector sensitivity by increasing $P_{\rm in}$, ϵ (which is limited to $\epsilon \leq 1$ by definition), and τ (up to $\tau = 1/(2f)$). As it scales approximately linearly with f, photon shot noise is an important sensitivity limit at high frequencies.

Radiation Pressure Noise: Radiation pressure noise arises from the transfer of momentum from the photons in the arms of the interferometer to the interferometer test masses. The limit to detector sensitivity, $h_{\rm rp}(f)$, set by this noise source can be shown to be [53]:

$$h_{\rm rp}(f) = \frac{N}{mf^2L}\sqrt{\frac{2\hbar P_{\rm in}}{\pi^3 \lambda c}}. \tag{1.11}$$

Symbols here have the same meanings as in equation 1.10, L is the length of the interferometer arms, m is the mass of the test mass, and N is the number of times the light impinges on the test mass, discussed in section 1.3.2.1. From this equation, it can be seen that increased laser power increases the noise. The effects of radiation pressure noise can be reduced by increasing m and L. As it scales as $1/f^2$, this noise is most significant at low frequency.

SQL: As photon shot noise decreases with laser power and radiation pressure noise increases with laser power, it is possible to choose an optimum laser power the minimizes both at a certain frequency, where $h_{\rm shot} = h_{\rm rp}$. This is known as the Standard Quantum Limit and exists in any interferometer configuration as a direct consequence of the Heisenberg Uncertainty Principle [52; 54; 55]. In a more coherent quantum treatment, the SQL can be understood as arising from a single source: vacuum fluctuations in the electromagnetic field entering through the output port of the interferometer [54; 56]. In essence, the shot noise arises from the uncertainty in the phase quadrature of the vacuum field entering the output port, and radiation pressure noise arises from uncertainty in the amplitude quadrature. It is possible to reduce the uncertainty in one

quadrature by 'squeezing' it into the other by injecting squeezed vacuum into the output port [57]. This allows, for example, the increase of laser power in order to reduce photon shot noise without the corresponding increase in radiation pressure noise.

1.3.2 Additions to the Standard Michelson Interferometer

The standard Michelson interferometer by itself would not be sensitive enough to detect gravitational waves [2]. Detector sensitivity increases with the amount of time the light is stored in the arms, either by making them longer or by storing the light in optical cavities in order to increase the light's exposure to passing gravitational waves. Sensitivity also increases with the amount of energy stored in the arms, up to the limit set by the SQL, but as discussed in section 1.3.1.4, there are methods for reducing even the SQL. Finally, there are ways to increase the actual gravitational wave signal by recycling it back into the interferometer. All of these techniques have been verified and tested in detectors, and most, if not all, will be included in future second- and third-generation detectors.

1.3.2.1 Fabry-Perot Cavities and Folded Arms

The simplest way to increase the light-storage time in the arms is to simply make the arms longer; however, as the beam tubes need to be in vacuum, simply elongating the beam tube becomes costly, and the curvature of the Earth becomes a problem. Instead, it is possible to fold the arm and send the beam back down the beam tube to an end mirror near the beamsplitter as in figure 1.3a. Alternatively, mirrors can be shaped so that beams can enter through a narrow aperture in the mirror near the beamsplitter and reflect back and forth between that and the end mirror along a complicated path, as seen in figure 1.3b [39; 58].

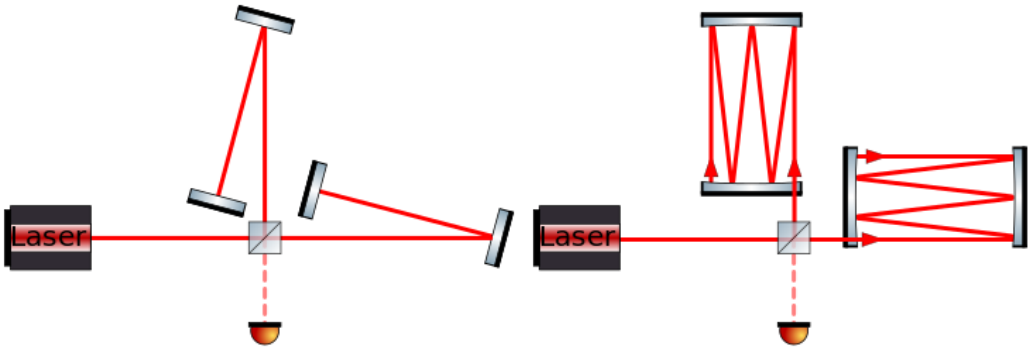

(a) Folded Arms (b) Delay Line

Figure 1.3: a) An example of the folded-arm interferometer topology. The arm lengths are effectively doubled, and the beam can be returned along the same vacuum tube as the outgoing beam. b) An example of a delay-line configuration. Here, the beam enters through a narrow slot in the first mirror, and reflects back and forth between the two curved mirrors until exiting out through the same slot.

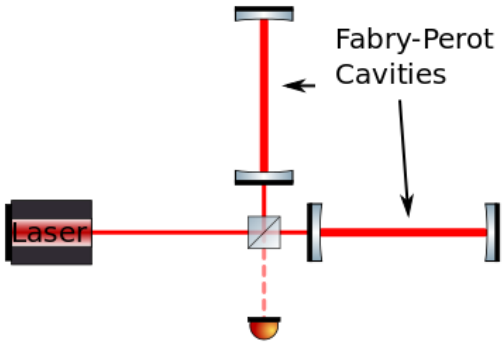

Figure 1.4: A Michelson interferometer with added Fabry-Perot cavities. The laser power resonating within the arm cavities is much higher than in a simple Michelson, with a much larger light storage time.

Another way to increase the light-storage time in the arms it to put the light into a Fabry-Perot cavity [59]. In a Fabry-Perot cavity, the light is stored in a resonating optical cavity, as in figure 1.4. The light leaves the beamsplitter and passes through the input mirror, which is partially transmitting. The far mirror acts as the test mass and is highly reflective. The cavity is held at resonance to allow the amount of energy stored within the arm cavities to become much greater than that of a standard Michelson. Eventually, the light leaks out through the input mirror and returns to the beamsplitter.

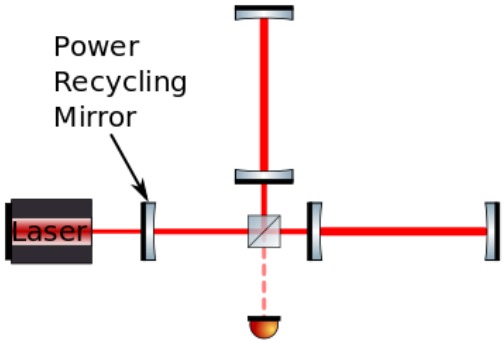

Figure 1.5: A Michelson interferometer with added Fabry-Perot cavities and a power recycling mirror. The power recycling mirror creates an additional cavity between the itself and the interferometer, increasing the power stored within the arm cavities.

1.3.2.2 Power Recycling

Power recycling is another way to increase the amount of light stored in the arm cavities. As the interferometers are held so that the output is at a dark fringe, the interferometer as a whole acts as a mirror at the input port. This means that essentially all light that is sent into the detector, in the absence of a gravitational-wave signal, exits back out of the input port. Placing another mirror, the power recycling mirror, at the input port creates another optical cavity with the added power recycling mirror at one end, and the interferometer at the other. This cavity can then be controlled so that no light is reflected back to the laser [60]. The recycled light is instead injected back into the arm cavities, increasing the power stored there.

1.3.2.3 Signal Recycling

Signal recycling is a method for increasing the strength of the gravitational wave detector as sensed at the photodetector at the expense of the bandwidth across which the interferometer is most sensitive. In this case, a partially transmissive mirror is placed at the output port. It causes the gravatitional wave signal to resonate within an optical cavity, bounded on one end by the signal recycling mirror and with the interferometer itself acting as the opposite

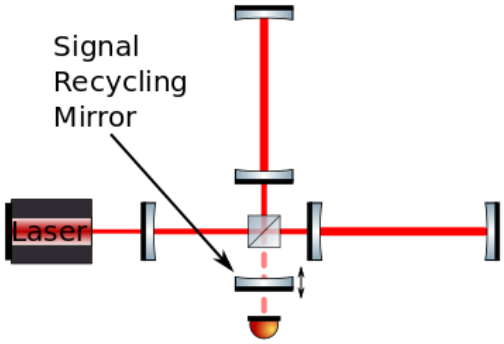

Figure 1.6: A Michelson interferometer with added Fabry-Perot cavities, power recycling mirror, and signal recycling mirror. The signal recycling mirror adds another cavity between itself and the interferometer, allowing the gravitational wave signal to resonate within the cavity and build strength.

mirror, allowing the signal to build [61; 62; 63]. The bandwidth over which the signal enhancement is effective is determined by the reflectivity of the mirror, and the centre of the frequency band is controlled by the length of the cavity formed between the mirror and the interferometer. Therefore, precise, quiet control of the mirror position is required, and the reflectivity must be carefully chosen beforehand to provide the desired detector response.

Signal recycling can be used to provide improved sensitivity over a narrow bandwidth in order to search for continuous wave sources like the neutron stars discussed in section 1.2.2.3. This way, a specific frequency can be picked out by controlling the cavity length for a short time instead of integration at a lower detector sensitivity for a long time. Alternatively, a broadband signal recycling scheme can be used to allow for a greater sensitivity to chirping signals like inspirals or burst sources like supernovae.

1.3.2.4 Squeezed Vacuum

Injecting squeezed vacuum states into the interferometer is a way to reduce the effects of the Standard Quantum Limit (Section 1.3.1.4). While not a direct addition to the interferometer like the methods discussed above, injecting squeezed vacuum through the output port requires intimate interaction with

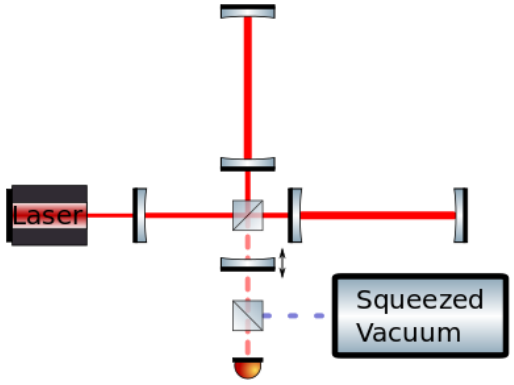

Figure 1.7: A squeezed vacuum state is injected into an advanced Michelson interferometer with Fabry-Perot cavities, a signal recycling mirror, and a power recycling mirror. The squeezed vacuum allow for the suppression of the SQL, allowing the benefits of increased laser power without the associated increase in radiation pressure noise.

the interferometer to insure that the squeezed vacuum is in phase and properly locked with the input laser [64; 57; 65]. However, once the squeezed vacuum is properly injected into the interferometer, existing detector configurations could expect up to 6 dB reduction in shot noise [66].

1.4 The Current State of Gravitational Wave Detection

Kilometre-scale interferometric gravitational wave detectors are now into their second decade of operation, and there exists a world-wide collaboration linking ground-based interferometric detector projects working towards making the first observation of gravitational waves. This collaboration contains the instruments of the Laser Interferometer Gravitational-wave Observatory (LIGO) in the United States, Virgo in Italy, GEO600 in Germany, and TAMA300 in Japan. The first generation of detectors have completed a set of science runs, setting interesting upper limits on a range of gravitational wave sources, and now, after a short phase of 'enhanced' operation, where many second-

generation technologies were tested, most of the detectors are moving on to second-generation upgrades which will almost certainly result in detections. There are further plans for the building of 3rd-generation detectors, whose purpose will be to act as long-term astronomical observatories.

1.4.1 LIGO

The Laser Interferometer Gravitational-wave Observatory (LIGO) is a facility in the United States composed of two widely-separated separated facilities acting together as one observatory. The two facilities are located in Livingston, Louisiana, and Hanford, Washington. The Livingston facility houses one detector with arm cavities of $\sim$ 4 km, and the Hanford facilities have housed two detectors within the same vacuum system: one with arm cavities $\sim$ 4 km long, and another with arm cavities $\sim$ 2 km long. LIGO is managed by groups from the California Institute of Technology and the Massachusetts Institute of Technology. Construction of the LIGO facilities was completed in 1999, and detectors began operating in their initial LIGO (iLIGO) configuration in 2001. Design sensitivity was achieved in 2005. In 2009, the LIGO detectors underwent a partial upgrade to a configuration called enhanced LIGO (eLIGO) and ran for one year at enhanced sensitivity before commissioning began on Advanced LIGO (ALIGO): a complete upgrade with the goal of improving sensitivity by a factor of 10.

iLIGO: The initial LIGO configuration was that of the standard Michelson with Fabry-Perot arm cavities and a power recycling mirror [67]. The detectors used a 10 Watt laser with a wavelength of 1064 nm, which after stabilization and filtering fed $\sim$ 4.5 W to the interferometer. This in turn led to as much as 20 kW of power being stored in the Fabry-Perot cavities in the arms. The test masses were 10.7 kg in mass, and the beam radius at the test masses was about 4 cm. The test masses were suspended as pendulums by a single loop of steel

wire, and were further isolated from ground motion by four-layer mass-spring isolations stacks [68]. The test masses were fused silica masses made reflective at 1064 nm using multilayer dielectric coatings made of alternating layers of silicon dioxide (silica, SiO_2) and tantalum pentoxide (tantala, Ta_2O_5).

The iLIGO detectors were designed to be sensitive to gravitational waves in the frequency band from 40-7000 Hz, and to be capable of detecting a gravitational wave strain amplitude of 10^{-21} at the instrument's most sensitive frequency [5]. The LIGO facilities were constructed in the late 1990's, and ran in commissioning mode in the first 5 years of the 2000's. Five science runs were carried out, the fifth of which (S5) had all detectors running at design sensitivity for over 1 year and taking data coincident with the GEO600 detector and the Virgo detector over parts of the science run.

eLIGO: Between the years of 2007-2009, the two 4-km LIGO interferometers were upgraded under the enhanced LIGO project (eLIGO). This upgrade consisted of two major improvements that increased detector sensitivity by a factor of two at most frequencies: the installation of a more powerful laser, and the transition from a heterodyne to a homodyne readout of the gravitational wave signal. The laser power was increased from 10 Watts to 30 Watts. This also required the replacement of various optical components capable of handling the increased power. To compensate for the effects of the increased laser power on the optics, an improved thermal compensation system was installed, which heats the mirror faces in order to compensate for optical distortion caused by absorption of laser light by the mirrors. In 2009, the interferometers were run for a further science run (S6) in the eLIGO configuration, also in coincidence with the GEO and Virgo detectors.

Advanced LIGO: In early 2011, the LIGO interferometers were taken offline for the commissioning of the second-generation LIGO detectors, the 'Advanced LIGO' system. The Advanced Ligo interferometers will use the same

facilities as the initial LIGO detectors, but with all the major hardware systems upgraded. This includes seismic isolation, suspensions, optics, and laser subsystems. In total, the upgrades are expected to improve the sensitivity by a factor of 10 over that of iLIGO, and provide a larger bandwidth, usable at frequencies as low as 10 Hz. The upgrades will include the addition of a signal recycling mirror, the installation of a 200 Watt laser, larger optics to allow for larger beam sizes, larger test masses (40 kg), improved mirror coatings (see chapter 2), monolithic silica suspensions, and increased seismic isolation [69].

1.4.2 Virgo

The Virgo detector, located in Cascina, Italy, is operated by a joint consortium of scientists from Italy, France, the Netherlands, Poland, and Hungary. The initial detector had a similar topology to iLIGO's, with a power-recycling mirror and Fabry-Perot arm cavities; however, at 3 km long, the arm cavities are slightly shorter than LIGO's. The Virgo detector design differed from that of LIGO in the low frequency range due to the use of a 'super-attenuator' seismic isolation system [70], which provides the detector with better sensitivity in the 10-40 Hz band than any other detector.

Virgo entered into a data sharing agreement with LIGO and GEO600 prior to its first science run, VSR1, in 2007. This agreement has allowed the three collaborations to organize periods of coincident data-taking, substantially increasing the likelihood of detections. After VSR1, Virgo made some enhancements to the interferometer. These upgrades included the installation of monolithic fibre suspensions, similar to those planned for use in Advanced LIGO, and a thermal compensation system. As of June 2011, the Virgo detector has been in a joint science run with the GEO600 detector, after which, a series of upgrades are planned to further increase sensitivity as part of the Advanced Virgo project.

The Advanced Virgo project will involve a series of hardware enhancements

to the existing Virgo facilities and detector with the goal of increasing Virgo's sensitivity by a factor of 10. This includes the installation of a signal-recycling mirror, a 165 Watt laser, larger mirrors (42 Kg from 21 Kg), an improved thermal compensation system, and a vacuum system 100 times better than that of the initial Virgo system [71]. Advanced Virgo is expected to begin taking data in 2014 [72].

1.4.3 GEO

GEO600 is a British/German gravitational-wave detector located in Germany, close to the town of Ruthe, near Hannover. Originally planned to be a 3 km underground detector, lack of funds forced the collaboration to build a smaller, 600 metre, above ground detector using more advanced methods to compensate for the lack of arm length. Construction started in 1995, and commissioning continued until 2001. Although the arms are only 600 m long, GEO600 uses a folded-arm configuration like in figure 1.3a, doubling the effective arm length to 1.2 km. Unlike the LIGO and Virgo detectors, the GEO600 detector does not use Fabry-Perot cavities; however, it does use power recycling and detuned signal recycling. GEO600 also has a triple pendulum suspension with the final stage monolithically suspended from silica fibres to reduce suspension thermal noise; it was the first of the detectors to utilize this technology [73].

GEO600 has operated in numerous observation runs with both the LIGO and Virgo detectors. It has also carried out a number of 'Astrowatch' observing runs, remaining online while other detectors are upgrading in order to detect any loud transient signals that might otherwise be missed. In 2009, GEO began an upgrade scheme called GEO-HF, which is designed to improve the detector's sensitivity, especially at high frequency [8]. This includes the addition of tuned signal recycling, a new DC readout, squeezed light injection, and increased light power. These upgrades are scheduled to be done sequentially, interleaved with Astrowatch observations.

1.4.4 Japanese Detectors

The Japanese gravitational wave community has been involved in interferometer operation since the late 1990s. Initially, using the TAMA 300 metre interferometer located near Tokyo [74], and continuing in the near future with the KAGRA detector [12], formerly known as the Large-scale Cryogenic Gravitational wave Telescope (LCGT) [11]. In addition, a test interferometer, named the cryogenic laser interferometer observatory (CLIO), was built in order to test cryogenic methods of the type planned for KAGRA. See [75] for discussion of all the Japanese detectors.

TAMA and CLIO were both designed as test-beds for the techniques intended for eventual implementation in KAGRA. The KAGRA detector will be a 3 km interferometer with a similar topology to that used in first-generation detectors with the addition of cryogenic sapphire mirrors for test masses, and it will be positioned underground in order to reduce seismic noise. The detector will have power recycling and Fabry-Perot arm cavities, as well as a three-stage seismic isolation system similar to Virgo's super-attenuator. The TAMA detector was designed as both a practising gravitational wave detector and for testing and training for longer baseline Japanese detectors. As such, the TAMA detector has the same suspension system and readout scheme as that planned for KAGRA. It has been involved in a number of science runs, many in coincidence with the LIGO, Virgo, and GEO600 detectors. The CLIO detector is located in the Kamioka mine, the future location of KAGRA, in order to test the seismic isolation of the underground location, as well as perfecting the cryogenic cooling of the mirrors. Aside form only having arm lengths of 100 m, CLIO uses all the same hardware as KAGRA.

1.4.5 ET

The Einstein gravitational wave Telescope (ET) [76], is a proposed third-generation gravitational wave detector which has just finished a design study

funded by the European Union. The design study focussed on developing a conceptual design for a detector with a sensitivity at least 10 times that of second-generation detectors. The design study proposes an observatory built 100-200 m underground, composed of three detectors in an equilateral configuration, each detector will be composed of two interferometers, one optimized for lower frequencies (2-40 Hz), and one for higher frequencies. Both interferometers will be dual-recycled with Fabry-Perot arm cavities, but the low-frequency interferometer will utilize greater seismic isolation and cryogenically cooled test masses to reduce thermal noise, while the high-frequency interferometer will have room-temperature test masses and higher laser power to reduce high-frequency shot noise. The facilities are designed to allow rapid improvements to the detectors as interferometer technology progresses.

1.5 Conclusion

Gravitational wave detectors are now entering their second generation, with the first direct detection and non-upper-limit astrophysical measurements expected to be achieved with this generation of instruments. The sensitivities of second-generation detectors, like Advanced LIGO and Advanced Virgo, will be limited mostly by noise sources such as gravity-gradient noise and the standard quantum limit. However, at their most sensitive frequency range, they will still be limited by thermal noise. Thermal noise may be considered a technical noise source, as there seems to be room for improvement over the current state of the art, but we are limited by our knowledge of the material properties involved. Thus, studies of the properties of the materials which make up the mirrors and their suspensions in the interferometric gravitational wave detectors is of particular interest when considering how to achieve the sensitivities desired for possible third-generation detectors such as ET, or for upgrades to the advanced detectors. The next chapter covers the theoretical basis of the

various types of thermal noise, and the remainder of this work chronicles the laboratory research into the material properties involved.

Chapter 2

Coating Thermal Noise

As was discussed in the previous chapter, one of the most sensitive tools in the search for gravitational waves, the gravitational-wave interferometer, can be limited across its most sensitive frequency band by thermal noise in the mirror coatings. First generation interferometers like LIGO and Virgo were limited by a set of technical noise sources (e.g., seismic noise, photon shot noise, etc.), but as the field of interferometry for gravitational wave detection has improved, these technical noise sources have been reduced to the point where enhanced and advanced versions of these detectors require the use of alternative techniques, like expanding the beam size on the mirrors, to keep the coating thermal noise floor at an acceptable level [69]. Second-generation detectors are expected to have sensitivities such that coating thermal noise is a strong limiting noise source, and if there are to be any further improvements to their sensitivity in the mid frequency range (a few tens of Hz to several hundred Hz), this noise will need to be fully understood and reduced. Third generation detectors will require even further reduction of coating thermal noise. The design concept for the Einstein Telescope utilizes cryogenic cooling and a xylophone configuration in part because of this requirement, and the Japanese KAGRA and CLIO detectors have been designed to include cryogenic cooling suspensions partly for this purpose. Understanding the underlying

cause of thermal noise, and the material properties that give rise to it are of great importance in all attempts to reduce thermal noise to the levels desired for future detectors.

2.1 Introduction

Thermal noise in an interferometric gravitational wave detector arises from thermally driven statistical processes within the mirror substrates, coatings, and suspensions. It can be classified into three groups: Brownian, thermoelastic, and thermo-refractive. Thermoelastic and thermo-refractive noise are closely related and can be combined as Thermo-optic noise [77]. Thermo-optic noise in general is not a large concern, as the effects are small in detectors with silica substrates, but may become important in detectors utilizing silicon or sapphire substrates [77]. Brownian noise, on the other hand, can have a significant effect in any detector. In many cases, the most prominent component of thermal noise across the operating band of ground-based gravitational wave detectors comes from the Brownian motion of the mirror coatings themselves, as noise sources nearest to the reflecting surface sensed by the interrogating laser beam have a greater impact on the interferometer signal. Finally, the magnitude of all of the thermal noise components is dependent upon the material properties of the coatings. The reduction of thermal noise in gravitational wave interferometers relies upon the accurate measurement and understanding these properties.

2.2 Brownian Noise

2.2.1 Origins of Brownian Noise

The name for Brownian noise comes from the fundamental process that lies at it's heart: the thermal motion of particles first described by Brown in 1828 [78]

and explained by Einstein in 1905 [79]. Through the Fluctuation-Dissipation theorem, the magnitude and frequency spectum of the Brownian fluctuations are related to the dissipative part of a mechanical system's impedance, $\mathbf{Z}(f)$, where $\mathbf{Z}(f)$ is defined as [80]:

$$\mathbf{Z}(f) \equiv \mathbf{F}(f)/v(f), \tag{2.1}$$

for a force $\mathbf{F}(f)$ applied to the system resulting in a motion with a velocity of amplitude $v(f)$. The power spectral density, $S_f(f)$, of such a force acting on a mechanical system is given by

$$S_f(f) = 4k_{\mathrm{B}}T\Re\{\mathbf{Z}(f)\}, \tag{2.2}$$

where k_b is Boltzmann's constant, and T is the temperature of the system. It is sometimes easier to consider the power spectral density of the fluctuation motion of the system,

$$S_x(f) = \frac{k_{\mathrm{B}}T\Re\{\mathbf{Y}(f)\}}{\pi^2 f^2}, \tag{2.3}$$

where $\mathbf{Y}(f)$ is the mechanical admittance of the system, equivalent to $\mathbf{Z}^{-1}(f)$.

Calculating the thermal noise of the system requires knowing the macroscopic mechanical impedance of the system. More specifically, it requires knowing the real part of the impedance, which is more commonly known as the dissipative part, or the damping coefficient. In the case of interferometric gravitational wave detectors, external sources of damping, such as gas damping and recoil damping [81], have been sufficiently reduced by careful design of the mirrors and suspension such that only the internal friction of the materials remains as a limiting source of thermal noise.

Internal friction in a material arises from its inherent anelasticity. When a stress is applied to the material, the strain response is not instantaneous, but develops over a finite relaxation time [82; 51]. If one were to apply an oscillating

stress, σ, with a stress amplitude σ_0 and frequency f to the material in the form [82],

$$\sigma = \sigma_0 e^{i2\pi ft}, \tag{2.4}$$

the resulting anelastic strain would be,

$$\epsilon = \epsilon_0 e^{i(2\pi ft - \phi)}. \tag{2.5}$$

This strain is periodic like the stress, and possesses the same frequency, but has a phase lag of ϕ. This phase lag is also known as the mechanical loss angle, or the mechanical dissipation factor, and represents the internal friction of the material. The mechanical loss can arise from many internal factors, such as the density of point defects, dislocations, or grain boundaries in crystalline materials [51]. In amorphous materials like silica, it may arise from changes in molecular arrangement due to stress and temperature [83; 84; 85; 86; 87].

An equivalent definition for mechanical loss angle is that it is a measure of the amount of mechanical energy dissipated per cycle of an oscillation at a particular frequency. This is true for all frequencies, but it is most easily measured at resonance where, for a mechanical system resonating at frequency f_0, the mechanical loss can be defined as [82]:

$$\phi(f_0) \equiv \frac{E_{\text{lostpercycle}}}{2\pi E_{\text{stored}}} \equiv \frac{\Delta f}{f_0}, \tag{2.6}$$

where E_{stored} and $E_{\text{lostpercycle}}$ are the total energy stored in the system and the energy lost per cycle, respectively, and Δf is the full width at half maximum of the resonance peak.

2.2.2 Brownian Noise from Coatings

Initial attempts to calculate the Brownian noise arising from the mirrors in the interferometer assumed that each resonant mode of the mirror masses

could be treated separately and with the right application of the fluctuation-dissipation theorem, summed together to get the total contribution in the interferometer [88; 81]. The mirror coatings were considered only as a source of damping to the much larger substrates. This approach, however, proved to be difficult [89], and is correct only in the case that the mechanical dissipation is homogeneously distributed throughout the mirror–a requirement that is broken when the coatings are applied to the surface.

A more complete application of the Fluctuation-Dissipation Theorem to calculating the mirror thermal noise was proposed by considering the effects on the interferometer readout directly [90; 91; 92]. In this way, the thermal noise is calculated from the power dissipated in the mirror from a notional pressure of the same spatial profile as the intensity of the laser beam illuminating the front face of the mirror. The power spectral density of the thermal displacement, $S_x(f)$, is then calculated using the Fluctuation-Dissipation Theorem to be [90]:

$$S_x(f) = \frac{2k_{\mathrm{B}}T}{\pi^2 f^2}\frac{W_{\mathrm{diss}}}{F_0^2}, \tag{2.7}$$

where F_0 is the peak amplitude of the oscillating force applied to the mirror surface, and W_{diss} is the power dissipated in the mirror. When the laser beam is sufficiently smaller in diameter than the mirror surface, the mirror can be approximated as half-infinite, and the power spectral density of the Brownian thermal noise, $S_x^{\mathrm{ITM}}(f)$, can be calculated as [91]:

$$S_x^{\mathrm{ITM}}(f) = \frac{2k_{\mathrm{B}}T}{\sqrt{\pi^3 f}}\frac{1-\nu^2}{E w_{\mathrm{m}}}\phi_{\mathrm{substrate}}(f), \tag{2.8}$$

where $\phi_{\mathrm{substrate}}(f)$ is the mechanical loss of the mirror material, E and ν are the Young's modulus and Poisson's ratio of the material, respectively, and w_{m} is the radius of the laser beam where the electric field amplitude has fallen to $1/e$ of the maximum value. Corrections to this formula can be made to account for larger beam radius to mirror surface ratios [91; 92]. So far, the contributions

to the thermal noise from the coating materials have still not been taken into account. However, a key outcome of the work was the realisation that the location of the mechanical loss within the mirror is extremely important when calculating the thermal noise.

Since the laser beam is reflected from the surface of the mirror, most of the sensing is done there, and hence, it is the source of most of the thermal noise. It follows that a source of dissipation located on the front face of the mirror would contribute more to the thermal noise than an identical source located far from the front face, which has significantly influence on the reflected signal. It is this realisation that makes it important to correctly include the effects of the dissipation of the mirror coatings.

If a multilayer reflective coating is approximated as a thin surface layer of thickness d and mechanical loss ϕ_{coating}, as in [93], the total power spectral density of the thermal noise from the mirror is given by

$$S_x^{\text{total}}(f) = \frac{2k_{\text{B}}T}{\sqrt{\pi^3}f}\frac{1-\nu^2}{w_{\text{m}}E}\left(\phi_{\text{substrate}} + \frac{2}{\sqrt{\pi}}\frac{(1-2\nu)}{(1-\nu)}\frac{d}{w_{\text{m}}}\phi_{\text{coating}}\right). \tag{2.9}$$

The coatings themselves, however, are not homogeneous. A more careful treatment of the problem, taking into account the multilayer stack organization of the coatings, and carefully employing the direct application of the Fluctuation-Dissipation Theorem as discussed above, gives a power spectral density of the Brownian thermal noise from the coated mirror as [94]:

$$\begin{aligned} S_x(f) =& \frac{2k_{\text{B}}T}{\sqrt{\pi^3}f}\frac{1-\nu^2}{w_{\text{m}}E}\Bigg\{\phi_{\text{substrate}} + \frac{1}{\sqrt{\pi}}\frac{d}{w_{\text{m}}}\frac{1}{EE'(1-\nu'^2)(1-\nu^2)} \\ &\times [E'^2(1+\nu)^2(1-2\nu)^2\phi_{\parallel} \\ &+ EE'\nu'(1+\nu)(1+\nu')(1-2\nu)(\phi_{\parallel}-\phi_{\perp}) \\ &+ E^2(1+\nu')^2(1-2\nu')^2\phi_{\perp}]\Bigg\}. \end{aligned} \tag{2.10}$$

Here, E and ν are the Young's modulus and Poisson's ratio of the substrate,

and E' and ν' are the Young's modulus and Poisson's ratio of the coating. $\phi_\parallel$ and $\phi_\perp$ are the mechanical loss values of the multilayer coating for strains parallel and perpendicular to the mirror surface, respectively. In the case where $E' = E$, $\nu' = \nu$, and $\phi_\parallel = \phi_\perp$, this equation simplifies to equation 2.9. In the case of current detectors, where the mirror substrate is made of silica, and the coating is a multilayer stack of alternating layers of SiO_2 and Ta_2O_5, the Poisson's ratios are small enough that equation 2.10 can be approximated to within $\approx$30% by setting $\nu' = \nu = 0$ [94]:

$$S_x(f) = \frac{2k_\mathrm{B}T}{\sqrt{\pi^3}f}\frac{1}{w_\mathrm{m}E}\left\{\phi_\mathrm{substrate} + \frac{1}{\sqrt{\pi}}\frac{d}{w_\mathrm{m}}\left(\frac{E'}{E}\phi_\parallel + \frac{E}{E'}\phi_\perp\right)\right\}. \tag{2.11}$$

This simplification is useful for quickly estimating the Brownian thermal noise from the detector mirrors. The contribution to the thermal noise power spectral density from the coatings alone are easily extracted from equation 2.11 by expanding the second term:

$$S_x^\mathrm{coating}(f) = \frac{2k_\mathrm{B}T}{\pi^2 f E}\frac{d}{w_\mathrm{m}^2}\left(\frac{E'}{E}\phi_\parallel + \frac{E}{E'}\phi_\perp\right). \tag{2.12}$$

It is from this equation that it is easy to see the effects of the lossy coating layer. The substrate mechanical loss is on the order of 10^{-8}, and the 'effective loss' of the coatings, calculated as the bracketed part of the above equation, is of the same order. As an example, the initial LIGO End Test Mass (ETM) coatings are composed of 19 bilayer stacks, each composed of a 1/4-λ thick tantala layer ($n = 2.07$) and a 1/4-λ thick silica layer ($n = 1.46$), and one 1/2-λ thick silica cap, where $\lambda = 1064$ nm. This gives a total coating thickness of $\sim$6 μm. With a coating mechanical loss of approximately 1.5×10^{-4}, and other typical values for the LIGO detectors [67], one calculates a value of $\sim 3 \times 10^{-8}$ for the bracketed part of equation 2.12.

2.3 Coating Thermo-Optic Noise

Thermoelastic and thermo-refractive noise arise from the same fundamental processes [95], which is why they are commonly combined as thermo-optic noise. Thermoelastic noise arises from the thermal expansion of the coating and substrate, and the stresses that arise from the different thermal expansion coefficients of the two. Thermo-optic noise arises from the same thermal variations, but the noise itself comes from the changing refractive indices of the coating materials and their effects on the laser beam in the interferometer.

2.3.1 Thermoelastic Noise

In thermoelastic noise, thermal expansion of a material gives rise to displacements of the front mirror surface. From [95] and [96], the power spectral density from thermoelastic noise arising from a coating of thickness d is:

$$S_x^{\mathrm{TE}}(f) \approx \frac{8k_{\mathrm{B}}T^2}{\sqrt{\pi^3 f}}\frac{d^2}{w_{\mathrm{m}}^2}(1+\nu_s)^2\frac{C_{\mathrm{f}}^2}{C_{\mathrm{s}}^2}\frac{\alpha_{\mathrm{s}}^2}{\sqrt{\kappa_{\mathrm{s}}C_{\mathrm{s}}}}\tilde{\Delta}^2, \tag{2.13}$$

where ν_{s} is the Poisson's ratio, C is the heat capacity, α is the thermal expansion coefficient, κ is the thermal conductivity, and the subscript s represents values for the substrate, while the subscript f represents the average properties of the coating materials. $\tilde{\Delta}^2$ is a dimensionless average of material properties that vanishes when the film and substrate are identical:

$$\tilde{\Delta}^2 \equiv \left\{\frac{C_{\mathrm{s}}}{2\alpha_{\mathrm{s}}C_{\mathrm{f}}}\left[\frac{\alpha}{1-\nu}\left(\frac{1+\nu}{1+\nu_{\mathrm{s}}}+(1-2\nu)\frac{E}{E_{\mathrm{s}}}\right)\right]_{\mathrm{avg}}-1\right\}^2, \tag{2.14}$$

where the bracketed average is over the unsubscripted values in the following way:

$$[X]_{\mathrm{avg}} \equiv \frac{d_{\mathrm{a}}}{d_{\mathrm{a}}+d_{\mathrm{b}}}X_{\mathrm{a}}+\frac{d_{\mathrm{b}}}{d_{\mathrm{a}}+d_{\mathrm{b}}}X_{\mathrm{b}}, \tag{2.15}$$

for the two coating materials of thickness d_{a} and d_{b}, respectively.

2.3.2 Thermo-refractive Noise

In a gravitational wave interferometer, the laser beam extracts information about the change in the optical length of the arm cavities, as well as fluctuations in the surface of the mirror. These fluctuations lead to fluctuations in the phase of the sensed optical field. It is these fluctuations in phase that are monitored to search for gravitational wave signals. Brownian thermal noise and thermoelastic noise are responsible for the fluctuations of the mirror surface, but there is another way to introduce phase noise into the reflected field. The high reflectivity of the mirror coatings is provided by high-quality multilayer coatings of alternating $\lambda/4$ thick high index of refraction (n_{H}) and low index of refraction (n_{L}) materials. The reflecting beam penetrates this coating to a certain depth, generally on the order of one pair of layers [97]. If the indices of refraction depend on temperature, i.e. $\beta = \mathrm{d}n/\mathrm{d}T$ is nonzero, temperature fluctuations of the coating materials would lead to fluctuations in the optical thickness of the layers, and hence additional phase noise in the interferometer.

In Reference [97], the authors use a similar approach to that of Levin [90] to calculate the spectral density of fluctuations in the phase caused by thermo-refractive fluctuations and the equivalent spectral density of surface displacement for comparison to other thermal noise sources. The equivalent spectral density is calculated to be:

$$S_{x,\beta}^{\mathrm{TO}}(f) = \frac{2\beta_{\mathrm{eff}}^2 \lambda^2 k_{\mathrm{B}} T^2}{w_{\mathrm{m}}^2 \sqrt{\pi^3 \rho C \kappa}}, \tag{2.16}$$

where λ is the wavelength of the laser beam, k_{B} is Boltzmann's constant, w_{m} is the radius of the beam spot on the mirror surface, defined as the point where the electric field amplitude has fallen by $1/e$ of its maximum value, and the following are defined for the substrate: T is the mean temperature, ρ is the material density, C is the specific heat capacity, and κ is the thermal conductivity. β_{eff} is the effective temperature dependence of the combined

indices of refraction:

$$\beta_{\text{eff}} = \frac{n_{\text{L}}^2\beta_{\text{L}} + n_{\text{H}}^2\beta_{\text{H}}}{4(n_{\text{L}}^2 - n_{\text{H}}^2)}. \tag{2.17}$$

2.3.3 Thermo-optic Noise

Since thermoelastic and thermo-refractive noise both arise from the same thermodynamic fluctuations they are often combined as thermo-optic noise [77]. In [77], the authors use the Levin approach to calculate a combined thermo-refractive and thermoelastic noise power spectral density. First, the power spectral density of the temperature fluctuations, $S_{\text{TO}}^{\Delta\text{T}}(f)$, is taken from [98]:

$$S_{\text{TO}}^{\Delta\text{T}}(f) = \frac{2k_{\text{b}}T^2}{w_{\text{m}}^2\sqrt{\pi^3\kappa C_{\text{v}} f}}, \tag{2.18}$$

where κ is the thermal conductivity and C_{v} is the heat capacity per volume. The effect of these thermal fluctuations on the phase noise are then calculated for both effects simultaneously to give the combined thermo-optic power spectral density, $S_{\text{TO}}^{\Delta\text{z}}$,

$$S_{\text{TO}}^{\Delta\text{z}}(f) \simeq S_{\text{TO}}^{\Delta\text{T}}(f)\left(\bar{\alpha}_{\text{c}}d - \bar{\beta}\lambda - \bar{\alpha}_{\text{s}}d\frac{C_{\text{c}}}{C_{\text{s}}}\right)^2, \tag{2.19}$$

where d is the thickness of the coating; λ is the wavelength of the laser beam; C is specific heat capacity; subscripts c and s refer to the coating and substrate, respectively; $\bar{\alpha}$ is an effective thermal expansion coefficient:

$$\bar{\alpha} \sim 2\alpha(1+\nu); \tag{2.20}$$

and $\bar{\beta}$ is an effective $\mathrm{d}n/\mathrm{d}T$ for the coating layer probed by the beam:

$$\bar{\beta} \simeq \frac{B_{\text{H}} + B_{\text{L}}(2(n_{\text{H}}/n_{\text{L}})^2 - 1)}{4(n_{\text{H}}^2 - n_{\text{L}}^2)}. \tag{2.21}$$

In the above equation, n is the index of refraction, subscripts L and H refer to the high index and low index material, respectively, and B is the fractional change in optical path length with respect to temperature,

$$B = \beta + \bar{\alpha} n. \tag{2.22}$$

The most important aspect of equation 2.19 is the negative sign between the thermoelastic ($\bar{\alpha}_c d$) and thermo-refractive ($\bar{\beta}\lambda$) parts of the equation. This demonstrates that the two effects work to cancel each other out, making thermo-optic noise a less important issue in the frequency-range of interest to ground-based gravitational wave detectors. It also indicates that the selection of materials with appropriate material properties could work to completely cancel this noise source.

2.4 Conclusion

Reducing the thermal noise in ground based interferometric gravitational wave detectors is of great importance, and this chapter has supplied the mathematical tools in order to calculate the level of thermal noise and to see how it can be reduced. The equations of note are 2.10, 2.12, 2.13, 2.16 and 2.19. From these, it can be seen that coating thermal noise in a specific frequency band can, on the whole, be reduced by increasing the radius of the laser beam sensing the face of the mirror and decreasing the temperature of the mirror. However, the usable beam radius is limited by the size of the mirror face, which is in turn limited by the availability of pure substrates of sufficient size as well as the requirements of suspending such mirrors. Decreasing temperature can lead to increasingly complicated suspensions and cooling systems. Nonetheless, beam sizes in advanced detectors have been increased over those of initial detectors, and alternative beam shapes have been considered [99; 100; 101]. Reduced temperature methods are already being implemented in the CLIO

and KAGRA detectors (see Section 1.4.4).

There remains a further avenue of research for reducing thermal noise: choosing materials with appropriate material properties. From 2.12, it is apparent that choosing a material with lower mechanical loss will also reduce thermal noise. In fact, mechanical loss has been shown to be temperature dependent ([83], for example), and this can, in some cases, reduce the effectiveness of reducing the mirror temperature. Mechanical loss, especially at cryogenic temperatures, has never been measured for many of the optical materials that may be considered. As more advanced detectors are planned and constructed, it becomes increasingly difficult to reduce temperature and increase beam radius. Ways to reduce the intrinsic mechanical loss in mirror coatings are still poorly understood. Chapters 3 and 4 thus address the measurement of the mechanical loss of two alternative materials under consideration as high index of refraction materials in gravitational wave detectors. Even if these materials are not ultimately used in detectors, the results will aid in the understanding of the mechanisms responsible for mechanical loss in amorphous materials.

Other material properties, such as Young's modulus, Poisson ratio, and thermal expansion coefficient occur throughout the equations governing thermal noise in the detector. For every material under consideration, these properties need to be accurately measured and better understood. This will allow for correctly estimating the level of thermal noise, and will also aid in choosing the most appropriate material to use. Brownian thermal noise, for example, is most likely reduced when the Young's modulus of the coating matches that of the substrate [102]. As will be seen in Chapter 3, knowing the Young's modulus is also necessary in calculating the mechanical loss of a coating material. Thermal expansion coefficient is necessary for calculating thermo-optic noise. Chapters 5 and 6 describe measurements of Young's modulus and thermal expansion coefficient of a number of materials under consideration for use in gravitational wave detectors.

Chapter 3

Temperature Dependence of the Mechanical Dissipation in Hafnium Dioxide Coatings

3.1 Introduction

First generation gravitational wave detectors used mirrors operating at room temperature that were constructed from an amorphous SiO_2 substrate with highly reflective surface created by applying alternating 1/4-λ (where $\lambda = 1064$ nm) layers of low-index-of-refraction Ion-Beam Sputtered (IBS) silica (SiO_2) and high-index tantala (Ta_2O_5). Studies suggest that the dominant source of the mechanical loss, and thus the thermal noise, originates in the Ta_2O_5 layers of the coating [103; 104]. Second-generation 'Advanced' detectors will have similar mirrors, but with the high-index tantala component doped with titania (TiO_2) at a concentration of $\sim 25\%$ [69], referred to as titania-doped tantala, or Ti:Ta_2O_5. Titania doping has been shown to reduce the mechanical loss of the multilayer mirror coatings by as much as 40% [94].

Planned third-generation detectors may utilize cryogenic cooling of the test masses in order the reduce the thermal noise in the suspension, mirror substrates, and coatings [50]. However, both silica and tantala coatings can show

mechanical loss peaks at cryogenic temperatures [105; 106]. The presence of these loss peaks counteract the reduction in thermal noise gained through reduced temperature, making silica and tantala potentially less-than-optimum as coating materials for cryogenic detectors. Various other amorphous oxide coatings are being considered for use in cryogenic gravitational wave detectors. The research presented here suggests that IBS hafnia (HfO_2) may be an interesting candidate as a replacement for tantala as the high-index material for use in cryogenic gravitational-wave detectors.

Studies of the cryogenic loss peak seen in bulk silica postulate that it arises from re-orientations of the Si-O bonds within a double-well potential [107; 108]. The origins of the low-temperature loss peaks observed in IBS tantala and titania-doped tantala coatings are under investigation, with recent results suggesting that these loss mechanisms may also arise from changes in the position of oxygen atoms within the material [105; 109]. The measurement of the temperature dependence of the mechanical loss of hafnia is also of interest to inform these studies as a further example of an IBS amorphous metal-oxide system.

This chapter presents the results of studies of the properties of hafnia in the context of its use as a possible cryogenic coating material. The mechanical loss of IBS hafnia deposited on silicon cantilevers was measured over the temperature range from 11 to 310 Kelvin, and compared to that of titania-doped tantala. As heat-treatment has been shown to affect measured loss [109], the effects of heat-treatment of the hafnia coatings at four different temperatures was also studied. Furthermore, as the onset of crystallization in the coating material has been shown to increase both mechanical loss [109] and optical absorption [110] in other coatings, electron-beam diffraction measurements of hafnia deposited on silica were made, and a discussion of the observed structure is included.

Section 3.2 gives an introduction to measuring mechanical loss in thin films,

while Section 3.3 describes the apparatus used in this research. The samples measured are described in Section 3.4. In-depth characterization of the apparatus and samples determined through the mechanical loss measurements can be found in Section 3.5, with the final mechanical loss of hafnia coatings given in Section 3.6. Finally, the results are discussed in Sections 3.7 and 3.8.

3.2 Technique

Mechanical loss was discussed in Section 2.2.1, where it was defined in equation 2.6 as the amount of energy lost per cycle of oscillation, normalized by the total energy in the system. In order to measure the mechanical loss of the samples, they are excited at their resonant frequencies and the resonances allowed to decay. In this case, equation 2.6 can be rearranged as:

$$A(\omega_0) = A_0 \exp\left(\frac{-\phi(\omega_0)\omega_0 t}{2}\right), \tag{3.1}$$

where A is the amplitude of the oscillation at resonant angular frequency, ω_0, and A_0 is the initial amplitude of the oscillation. The mechanical loss of the sample can be found by first exciting a resonant mode and then observing the amplitude as it decays.

The bending mode frequencies, f_n, of a cantilever of length L and thickness t can be found using the formula [111]:

$$f_n = \beta_n^2 \frac{t}{4\pi\sqrt{3}L^2}\left(\frac{E}{\rho}\right)^{\frac{1}{2}}, \tag{3.2}$$

where n is the order of the mode, E is the Young's modulus of the cantilever material, ρ is the density, and the factor β_n is the solution to $\cos(\beta_n) =$

$-1/\cosh(\beta_n)$, approximated as:

$$\beta_n \simeq \begin{cases} 1.875 & \text{for } n = 1 \\ 4.694 & \text{for } n = 2 \\ 7.853 & \text{for } n = 3 \\ 10.996 & \text{for } n = 4 \\ 14.137 & \text{for } n = 5 \\ \dfrac{(2n-1)\pi}{2} & \text{for } n > 5. \end{cases} \tag{3.3}$$

The values used for E and ρ are 166 GPa and 2330 kg/m^3 [112], respectively.

Once the mechanical loss of a coated substrate, ϕ_{coated}, is measured, it is necessary to separate the loss of the coating, ϕ_{coating}, from the loss of the substrate, $\phi_{\text{substrate}}$. This is because the majority of the energy is stored in the substrate, and only the fraction of elastic energy that is stored in the coating samples the coating mechanical loss. The coating loss is calculated by rearranging the following equation [113]:

$$\phi_{\text{coated}} \approx \phi_{\text{substrate}} + R_{\text{Energy}} \times \phi_{\text{coating}}, \tag{3.4}$$

where R_{Energy} is the ratio of the strain energy stored in the coating to the total strain energy in the system. In the case of a thin cantilever, where the coating is thin in comparison to the substrate, this energy ratio is calculated to be [114]:

$$R_{\text{Energy}} = \frac{3E_{\text{c}}t_{\text{c}}}{E_{\text{s}}t_{\text{s}}}, \tag{3.5}$$

where t is thickness, E is Young's modulus, and the subscripts $_{\text{c}}$ and $_{\text{s}}$ mark values for the coating and substrate, respectively. Combining equations 3.4 and 3.5 and solving for the loss of the coating gives,

$$\phi_{\text{coating}} = \frac{E_{\text{s}}t_{\text{s}}}{3E_{\text{c}}t_{\text{c}}}(\phi_{\text{coated}} - \phi_{\text{substrate}}). \tag{3.6}$$

Using this equation, the loss of the uncoated control samples was used for $\phi_{\text{substrate}}$, and this was subtracted from the loss of the coated samples, ϕ_{coated}, to give the coating mechanical loss, ϕ_{coating}.

The calculated coating mechanical loss, ϕ_{coating}, as it is measured from the bending modes of the cantilever, is a direct measurement of the mechanical loss parallel to the mirror surface, $\phi_{\parallel}$, given in equation 2.12 for a single layer. As there are currently no established methods for measuring $\phi_{\perp}$, and the coatings are amorphous–and therefore assumed isotropic–this value is generally used as a measurement of $\phi_{\perp}$ as well.

3.3 Apparatus

Loss measurements were made in an apparatus like the one shown in figure 3.1. A sample is clamped in a stainless steel clamp, between a large stiff base and a smaller securing bar. This clamping assembly is suspended from the baseplate, which is cooled using liquid helium. The entire assembly is surrounded by a shield cooled using liquid nitrogen. The temperature is monitored by a Lakeshore DT-670-SD silicon diode temperature sensor attached with varnish directly below the sample within the large base of the clamp. The sample is heated using two resistive heaters, one on either side of the large base. The temperature is controlled by a Lakeshore Model 340 PID temperature controller. This setup allows the sample temperature to be reliably controlled between 11 and 310 Kelvin with typical temperature fluctuations less than 0.1 K. Excess loss due to gas damping is reduced to a negligible amount by holding the vacuum chamber at a pressure of $< 1 \times 10^{-5}$ mbar [115].

The cantilever bending modes are excited using an electrostatic drive plate. The drive plate is placed near the free end of the cantilever with a sample-exciter plate separation on the order of 5 mm. A large voltage offset is applied to the drive plate, generally on the order of 1 kV, and the oscillating excitation voltage is applied on top of the offset. The most effective rms voltage is highly

dependent on the mode shape and sample-exciter separation and is chosen through testing before a measurement is made. A photograph of the clamping structure, heaters, and drive plate is shown in figure 3.2.

A laser beam is shone across the thin edge of the cantilever allowing the oscillations to be detected by a split photodiode shadow sensor. The sensing laser is shone through a window on one side of the cryostat, across the edge of the cantilever and through a window on the opposite side of the cryostat. The split photodiode is placed so that the thin shadow of the cantilever falls along the split between the two photodiodes. As the sample oscillates, its shadow moves to cover some of first one photodiode and then the other, and the difference of the two photodiode signals is proportional to the positon of the sample.

The loss measurements are controlled using a program, written in LabView, which feeds temperature control information to the temperature controller, activates the excitation, and records the amplitude ring-down of the excited mode. A typical measurement cycle would run as follows:

1. The sample is clamped in the cryostat.

2. The cryostat is sealed and pumped to $< 10^{-5}$ mbar.

3. Bending resonant modes are located manually using labview program and equation 3.2.

4. The cryostat is cooled using liquid Nitrogen (LN_2) and/or liquid Helium (LHe) to the desired starting temperature, usually $\sim$11 K.

5. The sample is heated to and stabilized at the desired measurement temperature, set in the Labview software.

6. The measurement is made, usually three times at each temperature point and at each mode. The resonant mode is excited by scanning the exci-

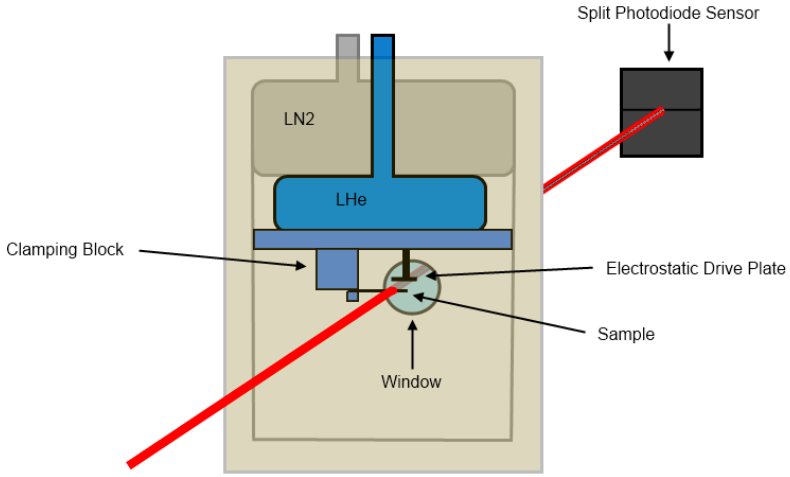

Figure 3.1: Diagram of mechanical loss apparatus. Clamping block is suspended from liquid Helium (LHe) cooled baseplate, and the entire assembly is surounded by a liquid Nitrogen (LN2) cooled shield. The environment is kept at a pressure below 10^{-5} mbar. The bending modes of the sample are excited by the electrostatic drive plate, and the amplitude decay is monitored by the movement of the sample shadow projected upon the split photodiode sensor.

tation frequency around the expected mode frequency until until a maximum amplitude is achieved. When the mode is excited, the excitation voltage is shut off, and the ring-down of the sample is recorded.

7. The above two steps are repeated until the final temperature (usually $\sim$310 K) is reached.

8. The cryostat is returned to room temperature and pressure, and the sample is changed or re-clamped.

3.4 Samples

In order to measure the mechanical loss of the IBS hafnia, coatings were ion-beam sputtered onto silicon cantilevers similar to those used in previous studies

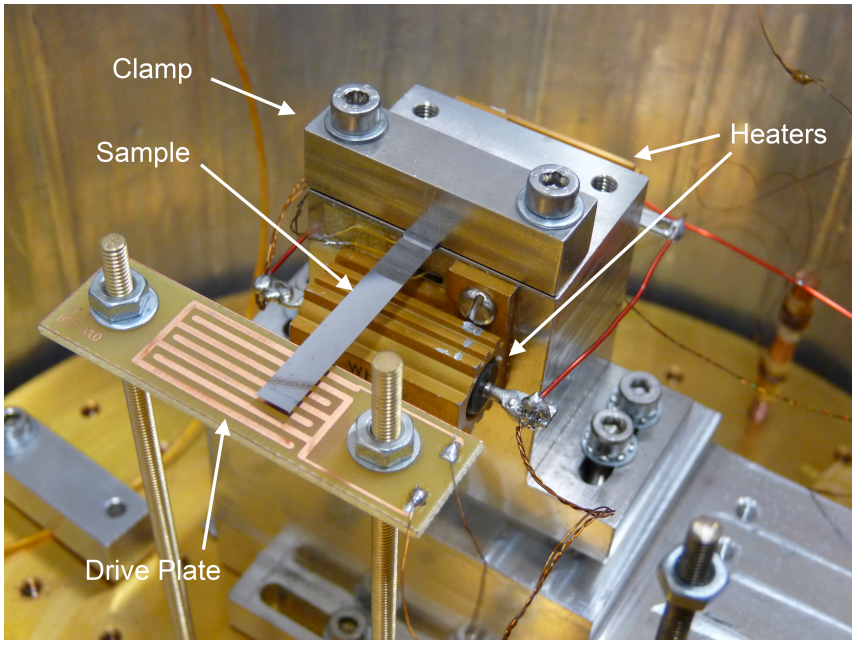

Figure 3.2: Photograph of a sample held within the cryostat. The sample, clamping structure, heaters, and drive plate are shown.

[115]. Cantilevers of dimensions 34 mm long x 5 mm wide and $\sim$115 μm thick were fabricated by chemical etching from a 0.5 mm thick single-crystal silicon wafer, with a 'clamping block' on one end having a thickness of 0.5 mm and 10 mm long x 5 mm wide, as illustrated in figure 3.3. The silicon [100] crystalline axis is oriented perpendicular to the long dimension of the cantilever, and the [110] crystalline axis is oriented parallel to the long dimension of the cantilever. Silicon has been chosen as a suitable substrate material because it exhibits relatively low mechanical loss at low temperatures, minimizing the substrate contribution to the measured loss [116]. Silicon has also been suggested as a mirror substrate material for use in third-generation detectors [10], so its cryogenic properties, and the properties of coatings deposited on it, are of specific interest.

A single layer of hafnia, was deposited on the cantilevers using ion-beam sputtering (IBS) by CSIRO [117]. IBS uses high-energy ions to sputter coating material from a target, creating high-density coatings on the substrate. IBS

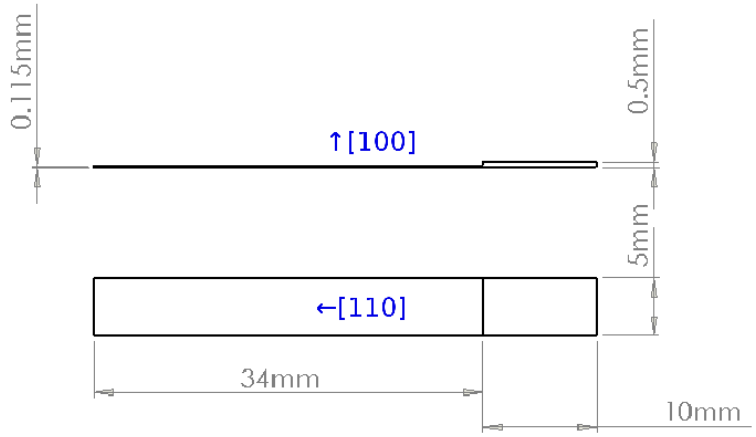

Figure 3.3: Diagram showing cantilever dimensions. Coatings were applied to the side without the clamping block protrusion. The crystallographic orientations of the silicon cantilever are accompanied by arrows.

coatings are known to have higher index of refraction and density than other coating deposition methods [118], and IBS coatings are used in all gravitational wave detectors due to their low optical absorption and low scatter loss. CSIRO reported that the hafnia layers were measured by ellipsometry to be (465 ± 5) nm thick. Post-deposition heat-treatment can be used to improve optical properties of the coating materials [119], and previous studies showed that the mechanical loss characteristics of tantala are modified by heat-treating the samples post-deposition [109]. However, heat-treatment can, at elevated levels, lead to crystallization of an amorphous coating and increased mechanical loss, as well as a degradation of the material's optical properties [110]. In order to study the effects of heat-treatment on the hafnia coatings, samples were heated to 400, 200 or 150° C, respectively, with a sample also left untreated, or 'as deposited'. It should be noted that even without the heat-treatment, each sample is heated to 100° C during the deposition process [120]. Samples were treated by heating the sample at a rate of 2° C/minute to the prescribed temperature and left at that temperature for 24 hours before cooling overnight

Table 3.1: Sample Numbers (SN) of the heat treated samples. Each coated sample was paired with an equivalently heat-treated uncoated control sample.

Coated SN	Uncoated SN	Heat Treatment [°C]
8	12	As Deposited
3	10	150
5	11	200
1	9	400

to 25° C. In order to allow for any effects of the heat-treatment on the loss of the silicon substrate, each coated cantilever had an uncoated control sample which went through the same heat-treatment process. Table 3.1 gives a summary of the heat-treatments of the coated and uncoated samples. By comparing the mechanical loss of the coated and uncoated samples, any systematic substrate effects should be minimized.

Equation 3.2 can be solved for t in order to calculate the thickness of the sample from the bending mode frequencies:

$$t = f_n \frac{4\pi\sqrt{3}L^2}{\beta_n^2} \left(\frac{\rho}{E}\right)^{\frac{1}{2}} . \tag{3.7}$$

This was done using the first three modes, and the resulting values are given in table 3.2. As the mode numbers become greater, there is an increase in the calculated thickness. This may be because lower frequency modes have fewer wavelengths to probe the sample and therefore tend to underestimate the thickness.

The thickness of the cantilevers can also be found directly using an optical profiler, as described in appendix A. These measurements show that cantilevers tend to vary in thickness along the length of the cantilever by as much as 20 percent of the average thickness, with the thinnest regions lying near the clamping block and at the cantilever end. This variation is most likely the result of the cantilever fabrication process. The discrepancy between the measured thickness and the thickness calculated from the resonant modes may arise from the variation in thickness along the length, with different mode fre-

quencies probing different regions of the cantilever. Another effect may arise due to any curvature in the width of the cantilever, which we were unable to measure, but would stiffen the cantilever, causing a higher effective Young's modulus, and lower estimates of thickness from equation 3.2. In calculating the energy ratio from equation 3.5, the thicknesesses calculated using the mode frequencies was used.

Ellipsometric measurements were made of the samples to determine the thickness of the thermal oxide layers that were deliberately grown on the samples during sample preparation and heat treatment. The samples were found to have a layer of amorphous thermal oxide approximately 30 nm thick beneath the coating. It was also discovered that the samples possessed a thin layer of silicon nitride on the uncoated side of the cantilever left over from the cantilever production of approximately 8 nm. Fortunately, such a thin layer would require extremely high loss in order to effect the measured loss. This does not appear to be the case [121]. In any case, the nitride layer was present on both coated and uncoated samples, so any additional loss associated with the layer would be removed in the calculation of the coating mechanical loss.

Table 3.2: Thickness of substrates calculated using equation 3.2 solved for t. Variations in thickness appear to arise due to the deviation from a perfectly flat cantilever, with different mode shapes probing different regions of the cantilever.

Sample	Mode	Frequency	Thickness [μm]
1	1	127	108±4
	2	845	114±4
	3	2387	115±4
3	1	130	110±4
	2	858	116±4
	3	2418	117±4

Continued on next page

Table 3.2 – continued from previous page

Sample	Mode	Frequency	Thickness [μm]
5	1	120	102±4
	2	826	112±4
	3	2355	114±4
8	1	128	109±4
	2	835	113±4
	3	2371	115±4
9	1	121	103±4
	2	779	105±4
	3	2210	107±4
10	1	120	102±4
	2	767	104±4
	3	2175	105±4
11	1	123	104±4
	2	825	112±4
	3	2358	114±4
12	1	128	109±4
	2	850	115±4
	3	2421	117±4

3.5 Data Acquisition and Characterization of Set-Up

3.5.1 Loss Measurement and Data Processing

This section details the procedure of analysing the raw data taken in the mechanical loss measurements and simple characterization of the apparatus and

samples that was done in order to ensure the repeatability of the experiment. A number of experiments were conducted in order to fully understand the apparatus, including the effects of different clamps and clamping conditions.

As discussed in 3.3, a single loss measurement consists of the excitation of a resonant mode and its subsequent amplitude decay, or 'ringdown'. A typical example of this can be seen in figure 3.4. An exponential function is fitted to the ringdown data, giving the mechanical loss of the sample according to equation 3.1. Every ringdown is checked by eye for goodness of fit, to ensure that a bad fit does not give an artificially low loss. In addition, any fits with an R^2 coefficient of determination of less than 0.9 is discarded automatically. This measurement is repeated 2-3 times at each temperature during each measurement cycle. Variations between repeated measurements were on the order of 5%, and the mean of these measurements is taken as the measured loss at that temperature and measurement cycle. Variations in measured loss between repeated measurement cycles, however, had much greater variability, as can be seen in figure 3.5.

The variability between measurement cycles appears to be due to changes in clamping conditions. Evidence of this can be seen in figure 3.5. As most variations in clamping conditions will cause excess loss, every sample is clamped and measured multiple times, and the lowest loss measurement within pre-defined 'temperature bins' is chosen as closest to the true loss. When the lowest loss in a temperature bin is significantly higher than the lowest loss in the bins around it, that measurement is rejected only if it is from a measurement cycle that is generally not selected in the nearby temperature bins, i.e. the measurement has been shown to suffer from poor clamping conditions in the temperature range of interest. This is illustrated in figure 3.6.

To summarize, the process of selecting the best mechanical loss measurements for each sample is as follows:

1. 2-3 ringdowns are made at each of a number of temperatures during a

measurement cycle.

2. Each ringdown is fit with an exponential in order to measure the mechanical loss, with poor fits being rejected.

3. The mean, minimum and maximum loss of the remaining measurements is recorded for each temperature in the measurement cycle.

4. Within a pre-defined range of temperatures, or 'temperature bin', the lowest loss from multiple measurement cycles is chosen as representative of the true mechanical loss of the sample within that temperature bin.

5. When a chosen loss in one temperature bin is much higher than the chosen loss in nearby temperature bins, and that loss is from a measurement cycle that appears to have artificially high loss in the surrounding temperature bins, that loss is rejected, and no mechanical loss data is recorded for that temperature bin.

3.5.2 Comparing Cryostats

Two cryostats, A and B, of the same design as discussed in Section 3.3 were used for taking measurements. While most samples were measured in Cryostat A, samples 1 and 10 were partially measured in Cryostat B, and sample 12 was completely measured in Cryostat B. Figure 3.7 gives an example comparing the loss of the same sample measured in both Cryostat A and Cryostat B. This variation is all within the expected variation of repeated clampings. Furthermore, figures 3.15, 3.16, and 3.17, which compare the measured loss of all the uncoated samples, including samples 12 and 10, show that they have comparable loss to samples 9 and 11, which were measured in Cryostat A.

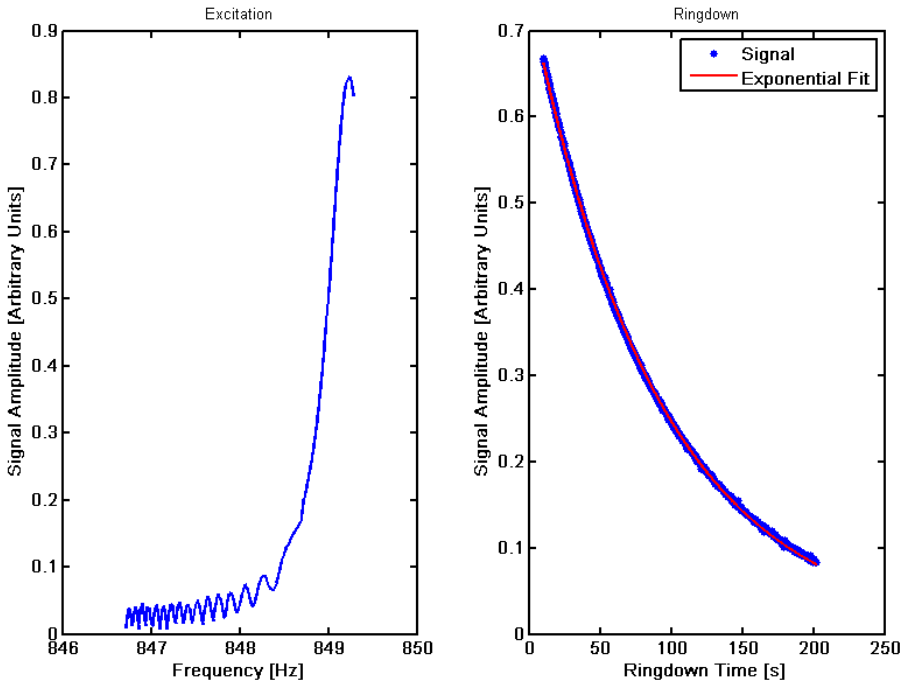

Figure 3.4: Example of a typical excitation and ringdown of a resonant mode. The figure on the left represents the excitation of the resonant mode, after which the excitation signal is removed, and the data displayed on the right is recorded. The red line indicates an exponential fit to the ringdown from which the mechanical loss is extracted according to equation 3.1.

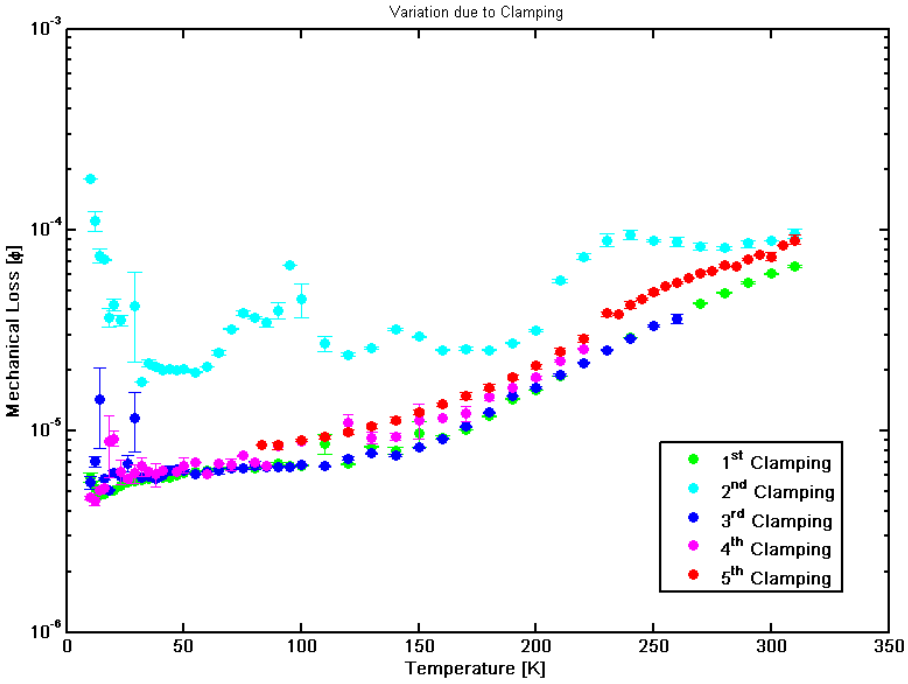

Figure 3.5: Mechanical loss measured for one sample over multiple measurement cycles. Error bars represent minimum and maximum values measured within one measurement cycle, if only one measurement was taken, there is no variation.

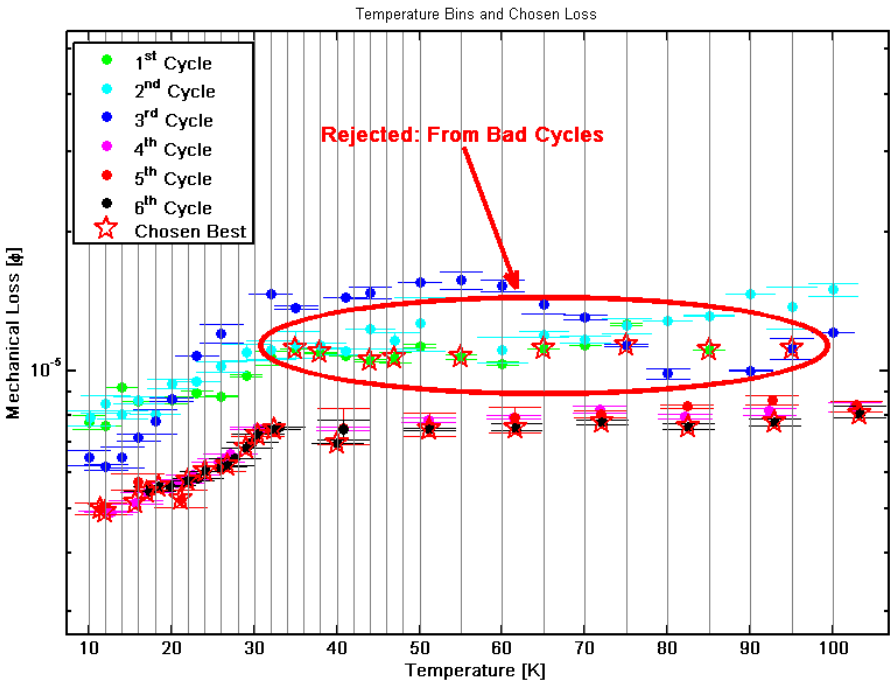

Figure 3.6: Illustration of the selection of the best mechanical loss from multiple measurement cycles. The temperature bins are drawn in grey, with the lowest loss in each temperature bin marked with a pentagram. The circled pentagrams are then removed from the final data set for being selected from a measurement cycle that is generally rejected in surrounding temperature bins.

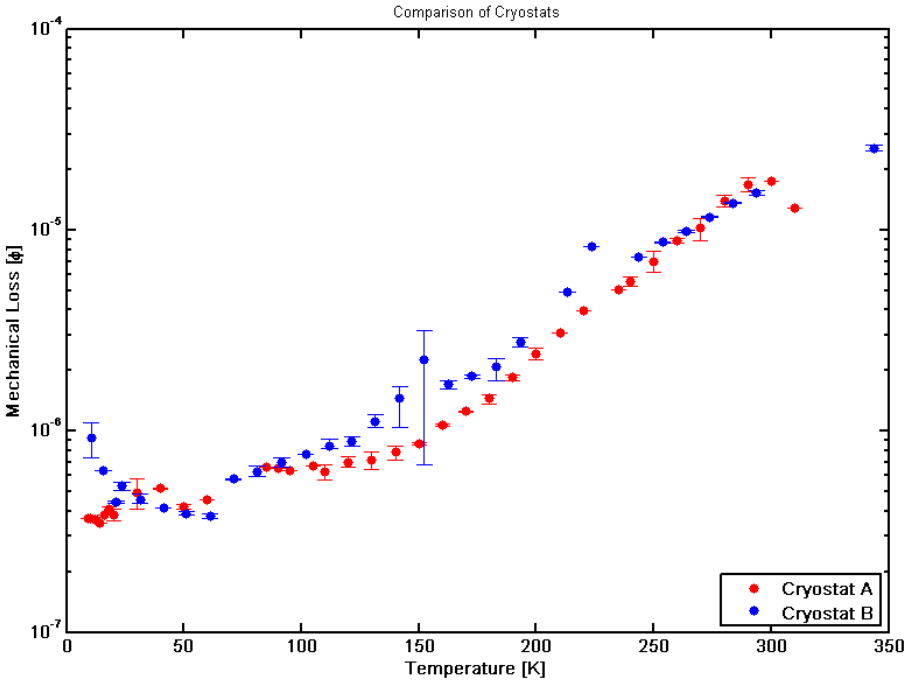

Figure 3.7: Example of the same mode and sample measured in both Cryostat A and Cryostat B. This example shows that the variation between the two cryostats is comparable to the variation between different clampings within the same cryostat.

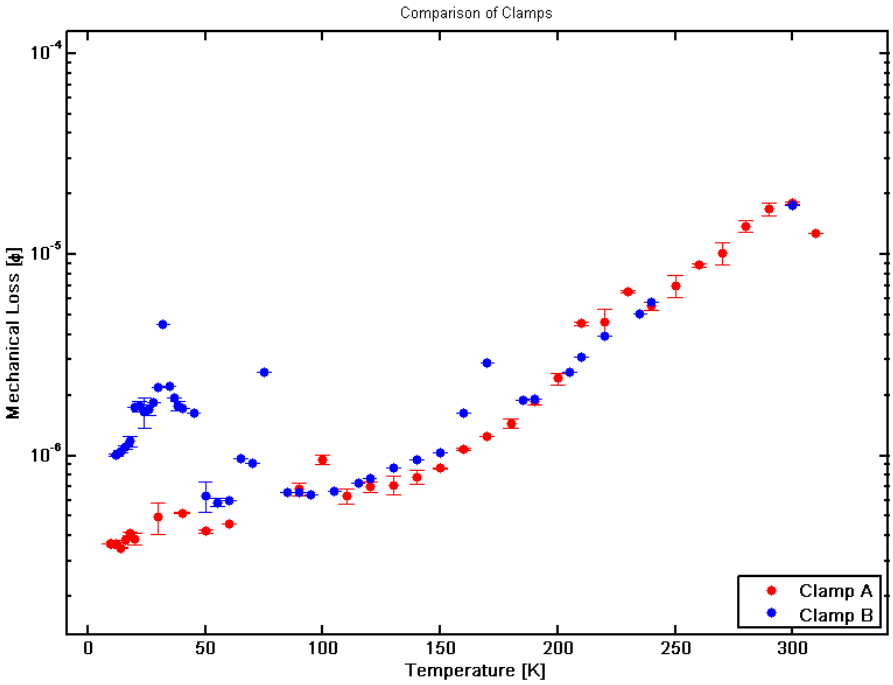

Figure 3.8: Example of the same mode and sample measured in the two different clamps in Cryostat A. This example shows that the variation between the clamps is comparable to the variation between different clampings within the same clamp.

3.5.3 Comparing Clamps

Cryostat A originally had two clamps, designated Clamp A and Clamp B. It was determined early in the research that operating both clamps simultaneously was not feasible due to the temperature control scheme, so the two clamps were tested to ensure that they gave similar results. Loss measurements from the two clamps are presented in figure 3.8. The figure shows that the two clamps yielded comparable results. Clamp A was eventually chosen as it tended to give lower loss measurements at low temperature, and had more stable temperature control.

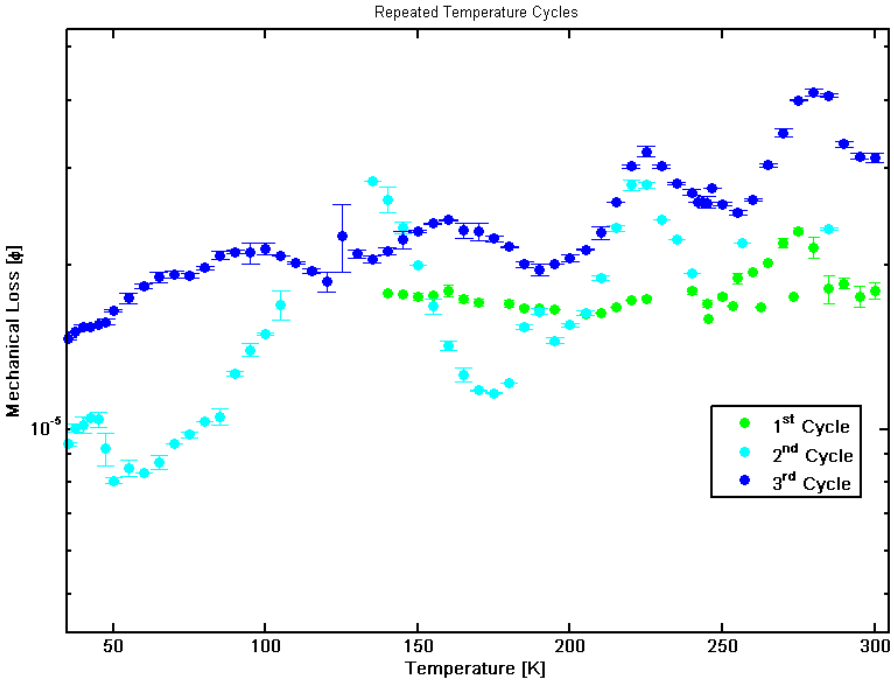

Figure 3.9: Example of the effect of temperature cycling on the measured loss of a sample. Repeated measurement cycles without reclamping leads to variations and higher loss measurements.

3.5.4 Temperature Cycling Effects on Clamping

Loss measurements over repeated measurement cycles without reclamping showed increasing variation with temperature cycling. It is suggested that this variation arose from the screws (visible in figure 3.2) loosening due to variation in thermal expansion between the material in the screws and those of the clamp and sample. An example of the changing mechanical loss with repeated measurement cycles is shown in figure 3.9. This is another reason why it was decided to always re-clamp the sample between measurement cycles.

3.5.5 Heating loss vs. cooling loss

All measurements were made with the cryostat heating up from a minimum temperature, with heaters controlling the rate, and cooling coming from reser-

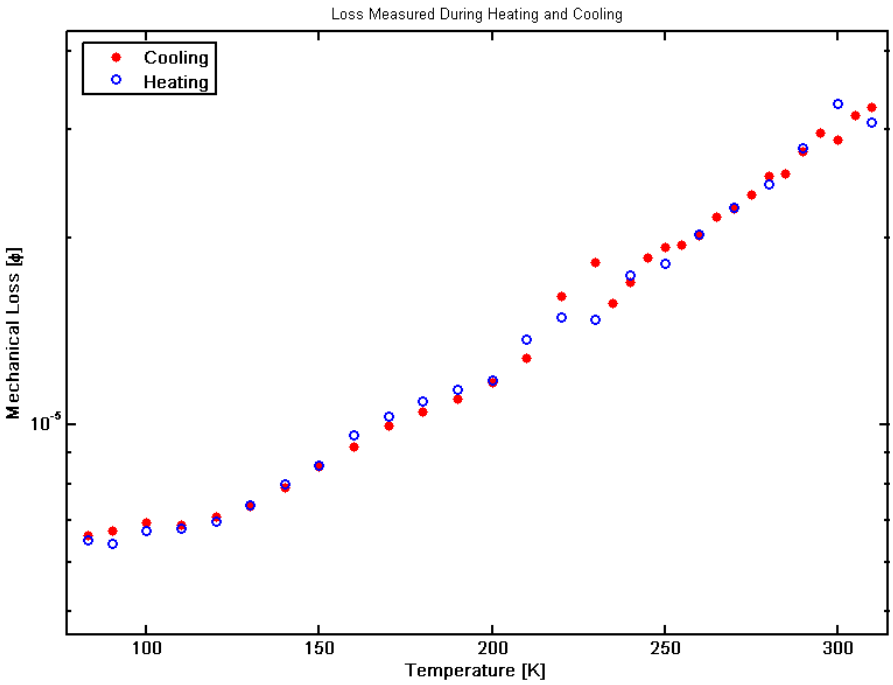

Figure 3.10: Test comparing the loss measured while the sample was cooling versus when it was being heated.

voirs of LN2 and LHe. In order to ensure that the loss was not dependent on the sample's previous thermal condition, a test was made comparing the loss measured at different temperatures while cooling and again while heating. The results of this test are shown in figure 3.10. While this test was only run down to a temperature of 80 K, it shows that within the range of 80 K to 310 K, the mechanical loss is not dependent upon the heating condition. These results also suggest that the effects of thermal cycling on the clamping conditions has no obvious effect at temperatures above 80 K.

3.5.6 Low Temperature Loss from High Voltage

Initial loss measurements were made with only the oscillating excitation voltage removed during the ringdown and the DC offset still in place. These measurements were marked by an unexpectedly large loss at temperatures be-

low $\sim$27 K, and visible only in the first two modes, with the losses dropping steeply back down to expected levels around 27 K. Figure 3.11 shows this effect. It was found that the effect was eliminated by removing the DC offset during ringdown. It was suspected that this effect may be related to the magnetomechanical pole effect [122], which is characterized by excessive loss at low temperatures and frequencies and is caused by damping due to a magnetic field. However, there was no strong magnetic field present in the cryostat. Furthermore, the pole effect is characterized by a deviation of the frequency-temperature relation: $f(T)^2/f_{\mathrm{RT}}^2$, where f_{RT} is the mode frequency at room temperature. The smooth, featureless frequency-temperature relation for the fundamental mode of a sample with the offset engaged is seen if figure 3.12, showing no deviations that might indicate the pole effect.

Another possible effect may be due to the excitation of currents within the silicon substrate, causing loss through increased electrical resistance at low temperatures. A similar effect has been seen in mechanical loss measurements where the mechanical resonances of the sample are excited by a capacitive excitor [123]. In such cases, the movement of the sample changes the capacitance of the exciter, causing a current to flow in the exciter circuit, which is dissipated by the resistance in the circuit [124]. In most cases, this dissipation is much smaller than the mechanical loss of the samples; however, it is expected that the oscillations would also drive a current in the sample, and if the resistance in the sample were large enough, it may come to dominate the mechanical loss.

Using a simple relation for the mechanical loss assuming all measured loss is due to dissipation in the excitation circuit [124],

$$\phi^{-1} = \frac{m\omega_0 x_0^4}{2\epsilon_0^2 S^2 V^2 R}, \tag{3.8}$$

where ϵ_0 is the permittivity of free space, and assuming reasonable values of mass of the sample, m, mode frequency, ω_0, sample-exciter separation, x_0,

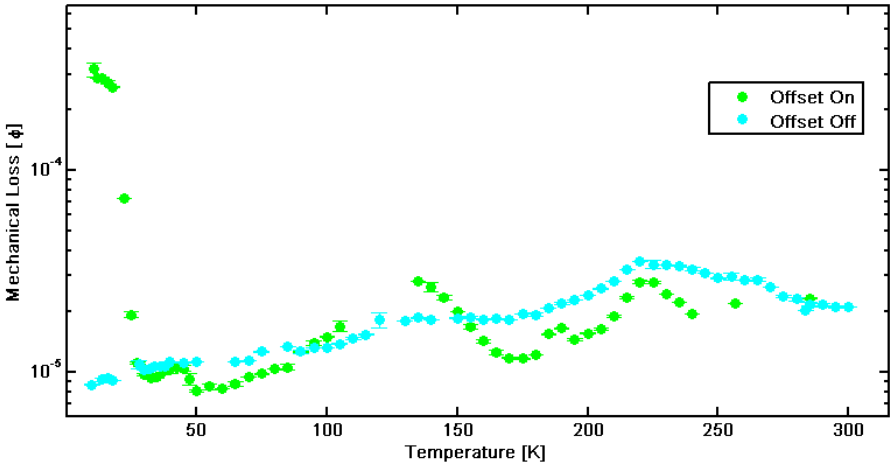

Figure 3.11: Comparison of mechanical loss measurements made with the high voltatge DC offset left on during ringdown and when the DC offset was turned off during ringdown. The DC offset clearly increases loss at temperatures below 27 K.

area of the capacitive plates, S, and offset voltage, V, a mechanical loss of 10^{-4} would be achieved with a resistance of $\sim$400 MΩ. This would require a silicon resistivity on the order of 10^5 Ω cm over the length of the cantilever. This is not impossible, as the resistivity of semiconductors rises exponentially with decreasing temperature. The resistivity of silicon at room temperature is less than 10 Ω cm, but at 20 K, it has been measured to be $\sim 10^4$ Ω cm [125]. The doping of the silicon can vary this value greatly, however, and values can easily reach 10^6 Ω cm [126]. Unfortunately, the doping of the silicon substrates used in the mechanical loss measurements is not known.

3.5.7 The Peak at $\sim$230 K

During measurements, a recurrent peak in mechanical loss appeared around the temperature of $\sim$ 230 K. This peak seemed independent of sample or frequency. However, as can be seen in figure 3.13, the height of the peak appeared to be influenced by clamping condition. A piezo-transducer, similar to that used in [116], was attached to the upper part of the clamp in order

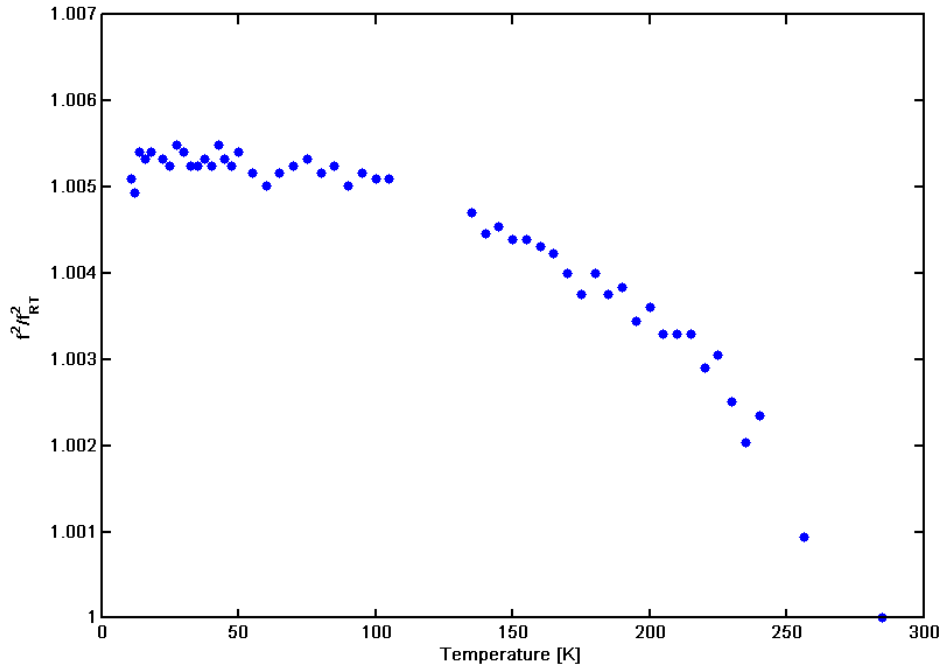

Figure 3.12: Frequency-temperature relation for a mode measured with the DC offset left on during ringdown. There is no obvious deviation around 27 K to indicate any magnetomechanical pole effects.

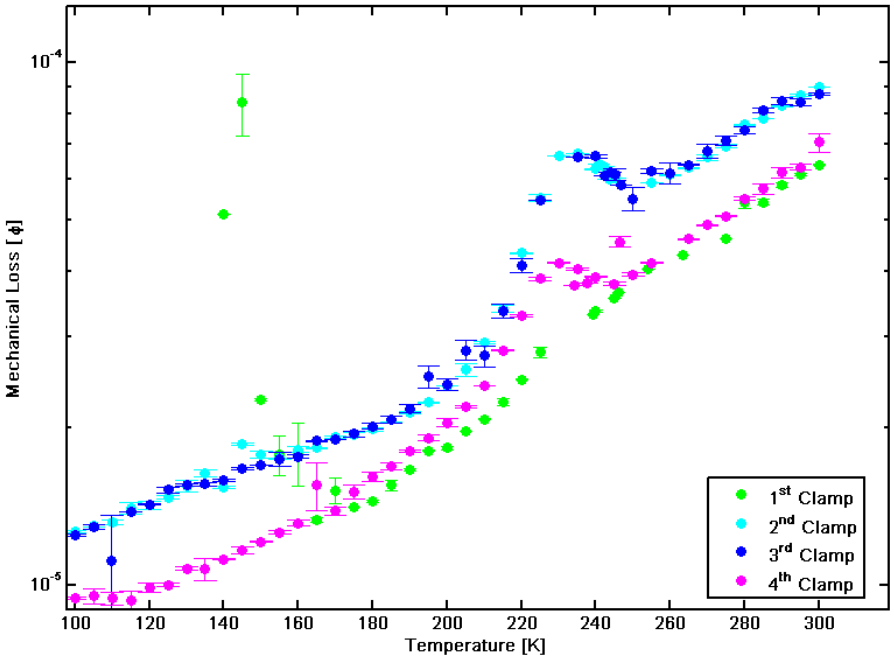

Figure 3.13: Example of the loss peak found near 230 K. Repeated clampings appear to reduce the appearance of the peak.

to test whether the loss peak was associated with energy coupling into the clamp. In a piezo measurement, the loss is measured using the same technique discussed above, however, the piezo signal is measured in parallel by recording the power spectrum of the piezo output taken when the amplitude of oscillation of the sample has reduced by half it's original value. The component of the piezo signal located at the mode frequency is then normalized to the energy of the oscillation by dividing by the initial amplitude of oscillation. In figure 3.14, the mechanical loss and normalized piezo signal are plotted together to demonstrate both the ∼230 K peak and the increased coupling into the clamp at temperatures above 200 K. The peak around 230 K appears to be caused by energy leaking into the clamp, the coupling of which must be dependent upon clamping conditions.

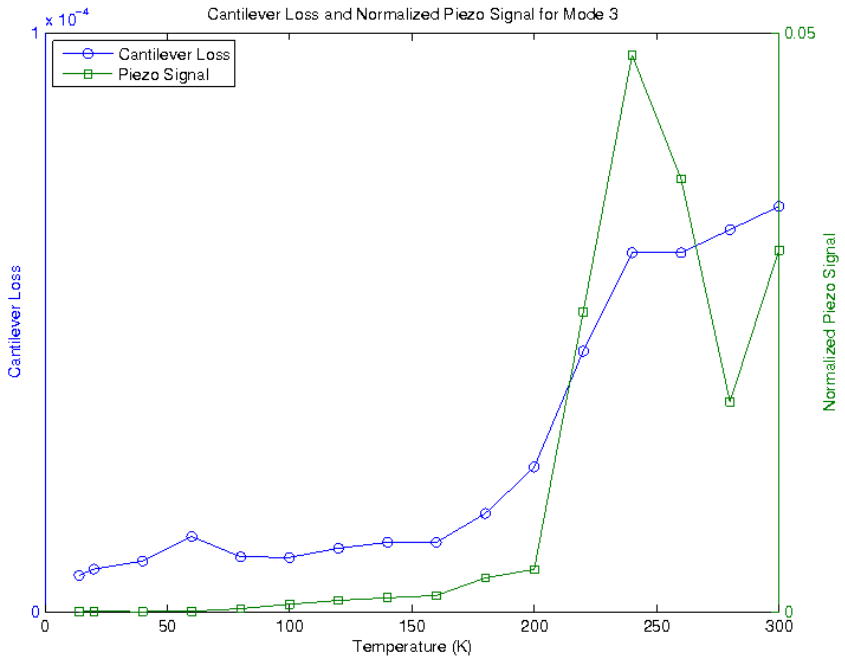

Figure 3.14: Example of piezo-transducer data compared to measured mechanical loss of a cantilever. The increased piezo response indicates that more energy is coupling into the clamp and increasing measured loss. The clamping resonance at ∼230 K is clearly visible, as well as a general increase in coupling to the clamp above 200 K.

3.5.8 Comparison of Uncoated Cantilevers

The best losses measured for each of the uncoated cantilevers can be compared in order to view the effects of heat-treatment. These are shown in figures 3.15, 3.16, and 3.17. First, it is necessary to note that sample number 9 (SN9), heat treated to 400° C, was broken after only one measurement cycle, so its data are not complete, and the mechanical loss may be artificially high due to the variation in clamping conditions discussed above. If SN9 is ignored, the following trends may be noted.

The mechanical loss of all samples is effectively the same at temperatures above 150 K. This is most likely due to the thermoelastic effect dominating the mechanical loss of the samples. The thermoelastic effect was discussed in Section 2.3.1. Here, it arises due to the transfer of heat during oscillation, where one side of the cantilever is in tension, and therefore cooled, and the other side is in compression, and therefore heated, and the flow of heat across the temperature gradient leads to a loss of energy from the oscillation. The equivalent mechanical loss of this effect can be calculated as [127; 128]:

$$\phi(\omega) = \frac{E\alpha^2 T}{\rho C} \frac{\omega\tau}{1+\omega\tau^2}, \tag{3.9}$$

where E is the Young's modulus, α is the thermal expansion coefficient, ρ is the density, and C is the specific heat capacity of the cantilever material. τ is called the relaxation time and is related to the time it takes for the heat to flow across the thickness of the cantilever. This sets a characteristic frequency where the thermoelastic loss is at a maximum, $f_{\text{char}} = (2\pi\tau)^{-1}$. For a cantilever of thickness t_{s}, τ can be calculated as [51]:

$$\tau = \frac{\rho C t_{\text{s}}^2}{\pi^2 \kappa}, \tag{3.10}$$

where κ is the thermal conductivity of the cantilever material. It is important to note that in silicon; α, κ, and C all have a strong temperature depen-

dence, so the values of τ and f_{char} vary with temperature. An example of the thermoelastic loss calculated for the samples is visible in figure 3.18.

At lower temperatures, there appears to be some variation, however it does not appear to be correlated with heat treatment or sample thickness. The mechanical losses of the uncoated cantilevers measured in this region were the lowest measured in the experiment. As such, they are the measurements most affected by variations in clamping conditions. It is at these regions where it is most obvious that these measurements are upper limits on the true loss of the cantilever. Fortunately, as is obvious in figure 3.18, the mechanical loss of the coated samples are at least an order of magnitude larger, so the calculation of the coating mechanical loss in this region will be largely unaffected by variations in this region. As SN9 was broken, and there appears to be no obvious trend in mechanical loss due to heat-treatment, SN11 was chosen as a replacement for SN9 in calculating the mechanical loss of the 400° C heat-treated hafnia coating.

3.6 Results

The mechanical losses of the coated and uncoated cantilevers were measured at the resonant frequencies of the first three bending modes at a range of temperatures between 11 and 310 Kelvin. The mechanical loss of the IBS hafnia coatings was calculated using equation 3.6 and the values in table 3.3. Figure 3.18 shows an example comparing the mechanical loss of a coated and uncoated samples, and the resulting coating mechanical loss. The blue line connecting the points of the uncoated sample shows the third-order spline fit used to calculate the mechanical loss values of the uncoated sample at temperatures corresponding to the values measured for the coated samples. The results of all coating mechanical loss calculations for each mode are shown in figures 3.19, 3.20, and 3.21. Uncertainties in the results are dominated by the uncertainty in the absolute value of the Young's modulus of the coatings.

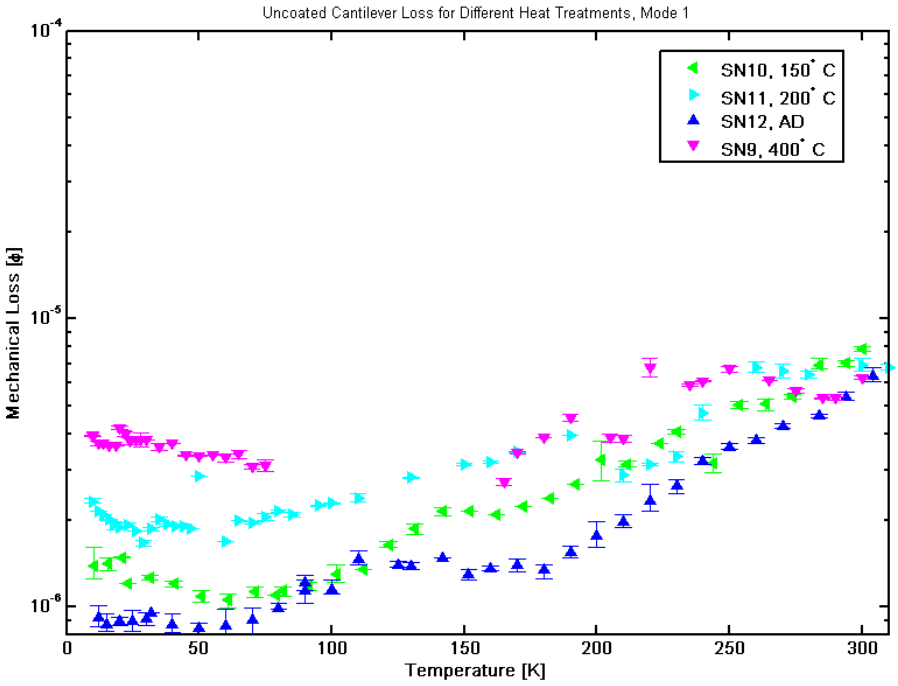

Figure 3.15: Comparison of the mechanical loss measured for the fundamental mode of all uncoated samples.

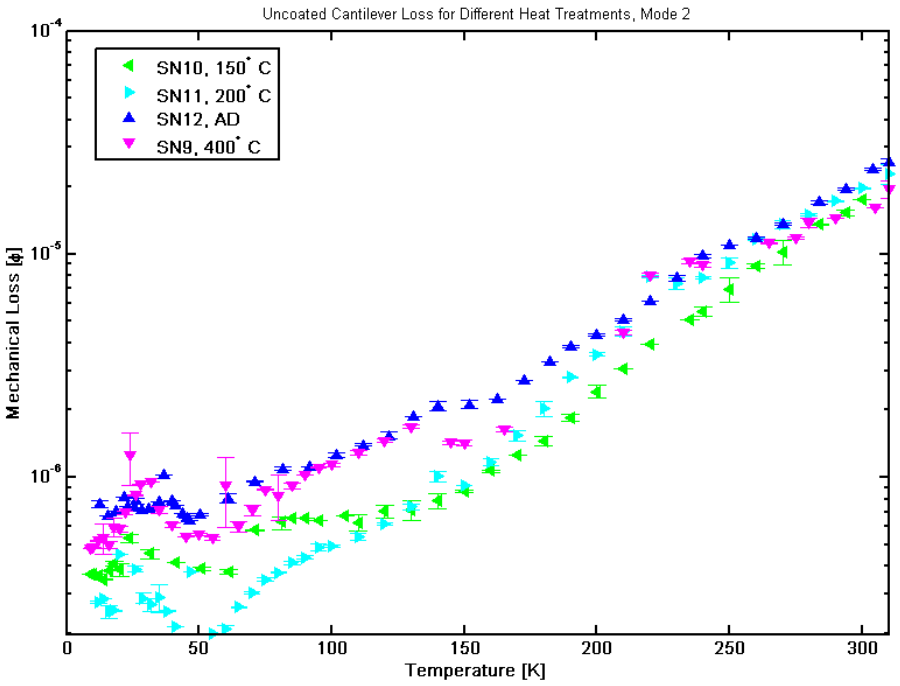

Figure 3.16: Comparison of the mechanical loss measured for the second mode of all uncoated samples.

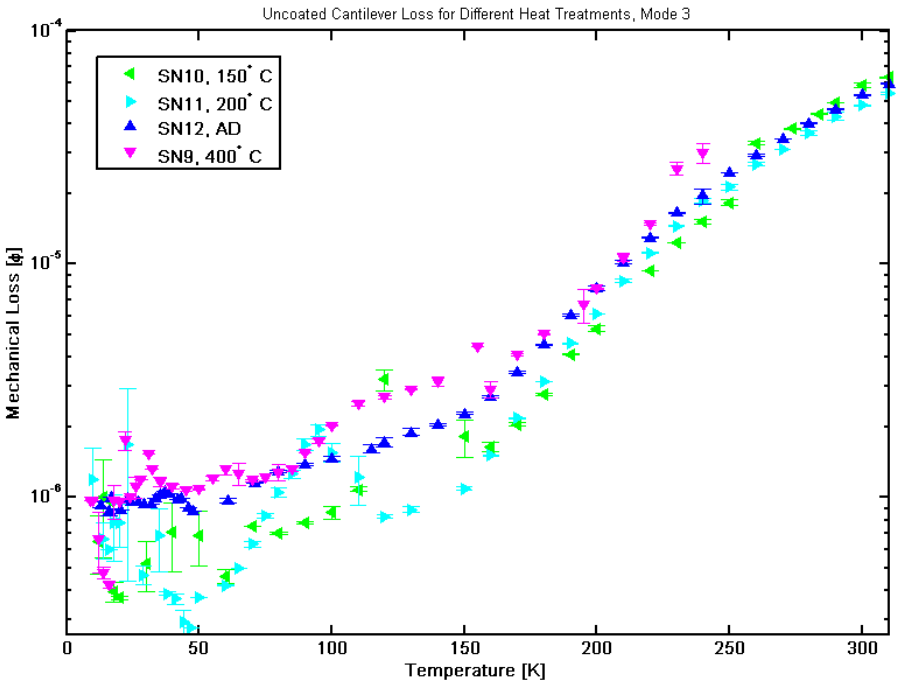

Figure 3.17: Comparison of the mechanical loss measured for the third mode of all uncoated samples.

Table 3.3: Values used in coating loss calculations, equation 3.6.

Parameter	Reference	Notes
$E_s = (164 \pm 3)$ GPa	[129]	
$t_s = 114{-}124\mu$m	3.4	Measured using equation 3.7
$E_c = (216 \pm 16)$ GPa	5	Measured using nano-indentation
$t_s = (465 \pm 2)$ nm	[117]	As ordered

First, consider the losses found for the second and third modes. The first feature of note lies between 10 and ∼120 K. This broad, low bump in the loss data does not appear to show any frequency dependence, and thus does not appear to have the same characteristic behaviour seen in low temperature loss peaks in amorphous silica and tantala. Instead, it may be similar in nature to the loss peak found in polycrystalline tantala films, which also shows no obvious frequency dependence and is centred on ∼90 K [109]. Secondly, the region from 100 K to 200 K shows an interesting temperature trend, with the 100° C heat-treated 'as deposited' sample always showing the highest loss, and the 400° C heat-treated sample showing the lowest loss.

Measurements of the loss of the fundamental mode (figure 3.21) show an apparent peak in the dissipation at ∼ 230 K, which has been identified to be a result of a resonance of the clamp used to hold the samples. This feature can be reduced under specific clamping conditions, and has been removed from the other modes through repeated clampings. Similar clamping effects are responsible for the excess loss seen in measurements above 200 K across all modes where these regions had much greater variability in loss between clampings. The fundamental mode has shown the greatest effects of clamping loss, and it is conceivable that the broad peak at ∼ 150 K seen in the 100 and 150° C heat-treated samples is also caused by clamping loss. That it only appears in the fundamental mode suggests it is unlikely to be an intrinsic characteristic of the material.

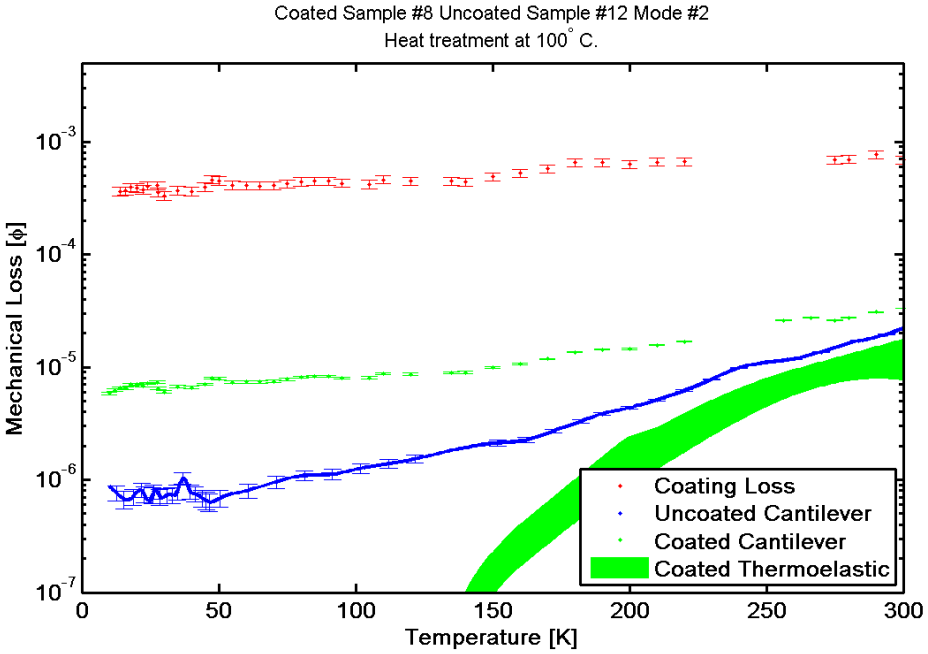

Figure 3.18: Comparison of the mechanical loss of the coated and uncoated cantilevers heat-treated to 100° C (AD). The blue line connecting the uncoated loss values shows the spline fit used to extract uncoated loss values at the temperature points measured for the coated cantilever. The green area shows the calculated thermoelastic loss for a pure silicon cantilever with the thickness of the coated sample substrate. The red points show the calculated coating loss.

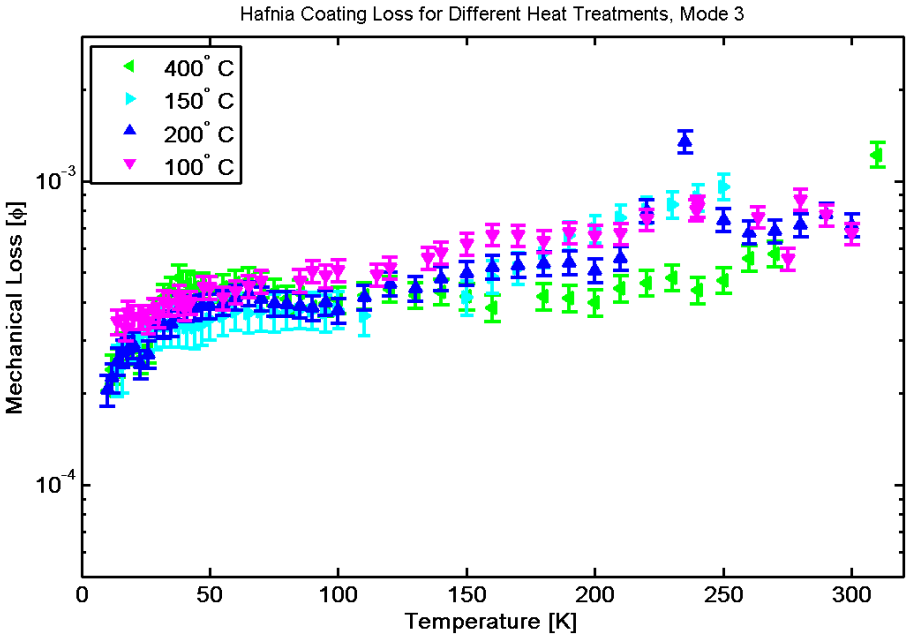

Figure 3.19: Mechanical loss of IBS hafnia coatings for four different heat-treatments at the frequency of the third bending mode at ∼2400 Hz.

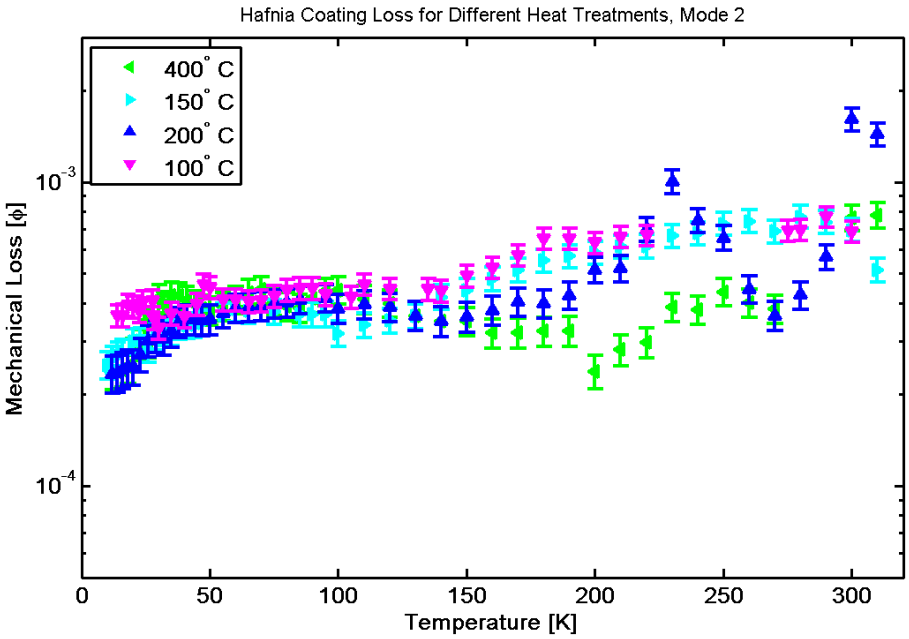

Figure 3.20: Mechanical loss of IBS hafnia coatings for four different heat-treatments at the frequency of the second bending mode at ∼850 Hz.

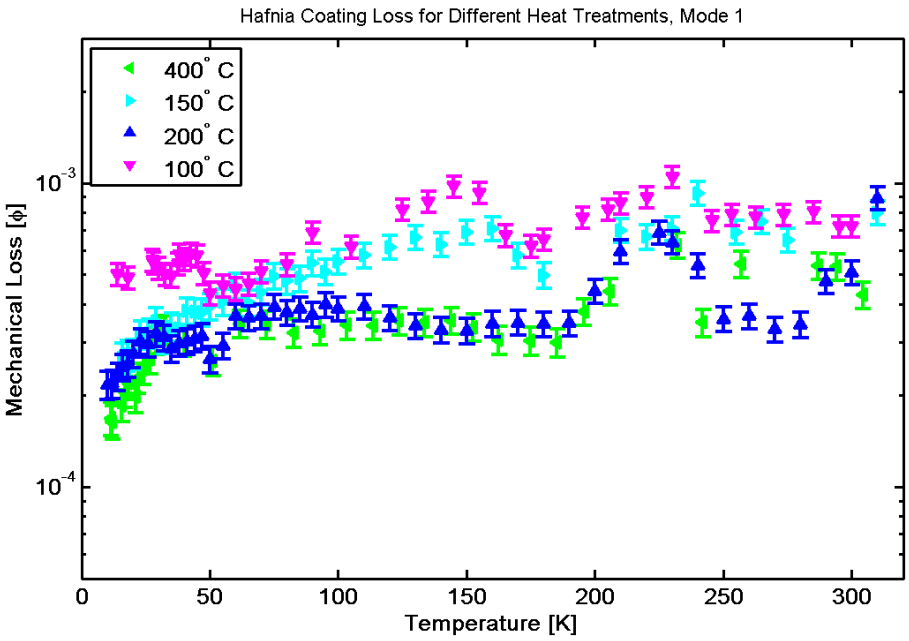

Figure 3.21: Mechanical loss of IBS hafnia coatings for four different heat-treatments at the frequency of the fundamental bending mode at ∼120 Hz.

3.6.1 Coating Structure

The structure of the coatings was studied using dark field Transmission Electron Microscope (TEM) imaging and convergent beam electron diffraction by Dr. Riccardo Bassiri. Figure 3.22 shows dark field TEM images where some crystallised areas of the coatings appear highlighted due to strong Bragg scattering of suitably orientated crystallites. The coatings appear to have partially crystallised, with the crystalline region extending from the coating surface down into the bulk of the coating, but not fully, as all samples show amorphous regions near the coating-substrate interface. From the dark field images there appear to be relatively small changes between the crystallisation from the 'as deposited' 100° C to the 400° C coating; however, there does appear to be a slight increase in the depth to which the crystallisation penetrates as the heat-treatment temperature is increased. The crystals appear to have grown in a columnar fashion, growing inwards from a nucleation point that is most

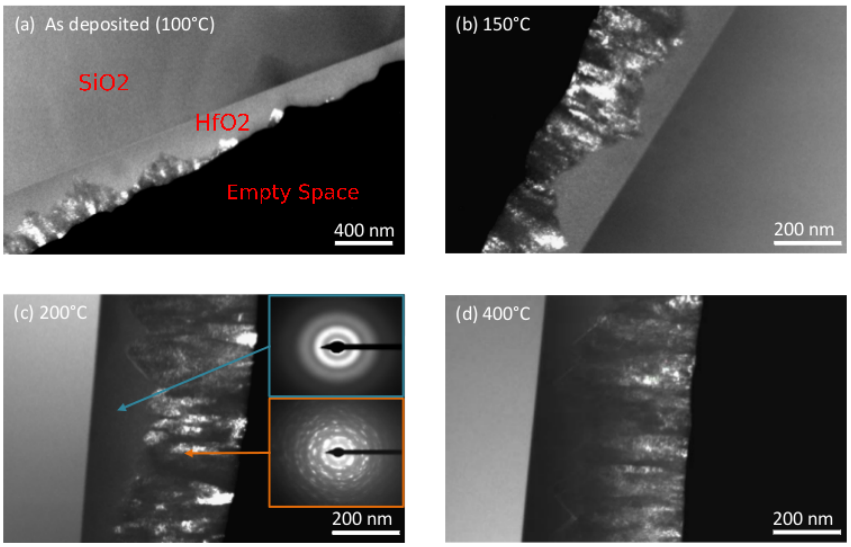

Figure 3.22: Dark-field TEM images taken from the heat-treated HfO2 coatings, showing the (a) 'as deposited' (100° C), (b) 150° C, (c) 200° C and (d) 400° C heat-treated coatings. (c) also highlights the part amorphous part crystalline nature of the coatings by showing the electron diffraction patterns taken from an amorphous and crystalline areas of the coating.

likely the coating surface. Another feature worth noting is the 'saw-tooth' appearance of the interface between the amorphous and crystallised coating. The crystallised areas appear to become better defined with increasing heat-treatment, as does the interface to the lower amorphous area, and is most noticeable in the 400° C coating (figure 3.22 (d)). Figure 3.22 (c) highlights the part-amorphous and part-crystalline nature of the HfO2 coatings, where the crystallised area of the coating appears polycrystalline from an electron diffraction pattern collected in a region near the surface and then fully amorphous in regions closer to the substrate. This result is similar for each of the heat-treated coatings studied.

3.7 Discussion

The mechanical loss of IBS hafnia films has been measured at cryogenic temperatures for four different heat-treatments. These measurements indicate that

the hafnia films do not possess a strong low-temperature loss peak of the type seen in amorphous metal-oxides such as silica and tantala. In the temperature range of 100-200 K, a trend was observed in which the samples heat-treated at successively higher temperatures display a reduced mechanical loss.

TEM measurements indicate that all of the films studied are partially crystalline, including the 'as deposited' sample. This indicates that the IBS process produces partially crystalline films, and that the maximum heat-treatment, to 400° C, is not enough to fully crystallize the films. This is similar to magnetron-sputtered hafnia films, where heat-treatment above 400° C is required to crystallize the film [130].

When compared to losses measured for IBS tantala films of the same thickness, described in [109], and reproduced in figure 3.23, it is clear that the hafnia coatings exhibit lower mechanical loss than tantala at temperatures below ∼100 K. This property suggests that hafnia may be an interesting high-index material for use in low-temperature gravitational-wave detectors such as the Einstein Telescope [10]. However, it should be noted that suitable optical properties, particularly low optical absorption and scatter, would also need to be achieved, which the partially crystalline nature of the specific coatings studied here would inhibit. Furthermore, there is evidence that when tantala is made polycrystalline by heat-treatment [110], it displays similar structure to that observed in the hafnia coatings, and its low-temperature mechanical loss properties become greatly elevated above and distorted from those seen in the amorphous coating [109]. This may also be the case in the hafnia coatings. If so, then a purely amorphous hafnia coating may have significantly reduced low-temperature mechanical loss over those seen here. An amorphous form of hafnia may also have improved optical properties. It is well known that polycrystalline coatings generally have poor optical properties [110], and the partially-crystalline nature of the IBS hafnia coatings may be responsible for the material's high (∼60 ppm) optical absorption, measured using photother-

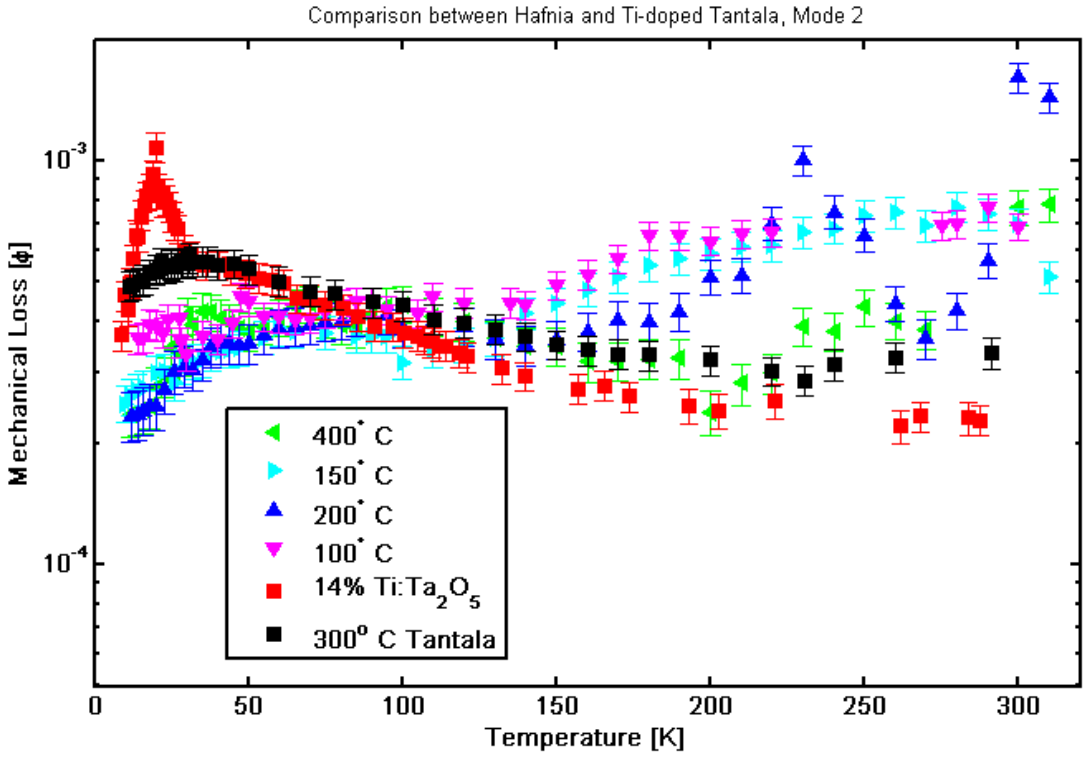

Figure 3.23: Comparison of IBS Ti-doped tantala coating mechanical loss from [109] to IBS hafnia coating mechanical loss measured here.

mal common path interferometry [131].

It has been shown that by doping IBS hafnia with silica during deposition, the material remains amorphous even after heat-treatments as high as 900° C [132]. To date, the mechanical loss of IBS silica-doped hafnia (Si:HfO_2) has only been measured at room temperature and as part of a multilayer stack, with silica as the other coating material, on a silica substrate [133]. This silica-doped hafnia, doped to a 30% Si cation concentration, has been demonstrated to remain amorphous after heat-treatment to 550° C. The mechanical loss of the silica-doped hafnia layers were calculated to be $(3.3 \pm 0.20) \times 10^{-4}$ [133]. Other dopants, such as lanthana (La_2O_3) [132] and Alumina (Al_2O_3) [134], have also been shown to reduce crystallization in hafnia films; however, the mechanical loss properties of these films have not been measured.

3.8 Conclusion

The mechanical loss of IBS hafnia coatings deposited on silicon has been measured over the temperature range of 11 K to 310 K. Samples have been heat-treated to 150, 200, 400° C and 'as deposited' (100° C). Measurements exhibit a broad loss peak similar in form to that seen in polycrystalline IBS tantala coatings but with lower loss. Electron microscope and electron diffraction measurements show that the hafnia coatings are partially crystalline in all samples. The mechanical loss measurements also show a heat-treatment-dependent trend in the temperatures between $\sim$ 100-200 K, with higher temperature heat-treatment yielding lower loss. At temperatures below $\sim$100 K, the mechanical loss of the hafnia coatings is lower than that seen in amorphous IBS Ti-doped tantala coatings of similar thickness. If a detector operating at 20 K were to use hafnia coatings with the loss given here, the coating thermal noise would be reduced to $\sim$70% of what would be achieved using titania-doped tantala coatings at the same temperatures. Doping of the hafnia coatings with silica has been suggested as a viable method for preventing the crystallization of the hafnia coatings, possibly improving their mechanical loss and optical properties. Further measurements of IBS Si-doped hafnia coatings are currently underway.

Chapter 4

Temperature Dependence of the Mechanical Dissipation in Ti-doped Tantalum Pentoxide Coatings

4.1 Introduction

As discussed in Section 3.1, the tantala layers of the reflective coatings used in current detectors dominate the Brownian thermal noise contribution of the coatings by having a significantly higher mechanical loss than the silica layers [103]. Research has shown that doping the tantala with titania (TiO_2) can reduce the mechanical loss of multilayer coatings by up to $\sim$40% [135]. For this reason, second-generation gravitational wave detectors will utilize multilayer coatings of silica and titania-doped tantala, doped at 25% titania (cation %) [69].

The reasons for the reduction in mechanical loss seen in titania-doped tantala (ti:tantala, Ti:Ta_2O_5) over that of pure tantala are still poorly understood. Measurements comparing the loss of 14.5% Ti:Ta_2O_5 heat-treated to 600° C

and that of pure tantala similarly heat-treated indicate that the tantala doping alters the distribution of activation energies associated with the low temperature dissipation peak associated with loss in amorphous tantala [106]. The nature of this dissipation is postulated to be similar to the peak seen in silica [107; 108; 84].

In the initial exploration of the effect of titania concentration on the mechanical loss of tantala, doping concentrations of $\sim$ 5, 10, 15, 20, 25, and 55% titania cation were studied. However, these samples were largely multilayer samples, and their mechanical losses were measured only at room temperature [135]. In order to more fully understand the effects of titania doping, it is important to study a wide range of doping concentrations as single-layers and at low temperatures.

Measurements of pure tantala have shown that post-deposition heat-treatment also has an effect on mechanical loss. Studies of pure tantala [109] show that heat treatment also effects the distribution of activation energies associated with the low temperature dissipation peak. In order to fully explore the reductions to tantala mechanical loss gained by titania doping, the study of the effects of heat-treatment on Ti:Ta_2O_5 at different concentrations is necessary.

In this chapter, the first measurements in a multi-staged experiment to study the effects of both heat-treatment and titania-dopant concentration on the mechanical loss of Ti:Ta_2O_5 are described. Here, we present measurements of mechanical loss between the temperatures of 10 and 310 K of 25 and 55% titania-doped tantala with no post-depostion heat-treatment, and the analysis of the low temperature dissipation peak associated with this heat-treatment. Planned future measurements will study the effects of 300, 400, and 600° C heat-treatments on the mechanical loss of samples with the same titania concentrations as the samples studied here.

4.2 Sample Preparation

The samples were nearly identical in form to those described in Section 3.4. The cantilever substrates were the same dimensions as those used to study hafnia coatings, with the exception that the cantilever thickness was reduced to 50 μm in order to further reduce any back-action into the clamp, which might lead to enhanced clamping losses. Coatings of 25 and 55% titania-doped tantala were deposited by the coating vendor, CSIRO, to a thickness of 500 ± 10 nm. Samples were heat-treated in the same way as the previously studied hafnia samples: AD, 300, 400, and 600° C, However, this chapter will only deal with the AD samples. The effect of other heat-treatments will be the subject of future work.

An additional variable associated with the deposition of the coatings was investigated. Whereas all of the hafnia coatings were deposited on the flat side of the sample, called the 'Bottom', one set of ti:tantala samples had the coatings deposited on the 'Bottom', and another identical set had the coatings deposited on the opposite side of the cantilever, the 'Top'. Figure 4.1 more clearly shows the difference in the location of the coatings. This variation allowed testing of any effects of the substrate surface preparation on measured loss, as the Top surface was chemically etched, while the Bottom surface is mechanically polished. A surface roughness of a similarly prepared cantilever has been previously measured to have an RMS surface roughness of 527 nm on the top surface, and 4 nm RMS surface roughness on the bottom surface [116]. Comparing the loss of Top and Bottom coated samples may provide information about any loss effects related to the coating-sample interface. Table 4.1 shows information on the sample preparation including the location of the coating on the sample.

Sample thickness was measured using the optical profiler and mode frequency methods discussed in Section 3.4 and in Appendix A. The substrate thicknesses calculated using the resonant mode frequencies were used in sep-

Table 4.1: TiO_2 cation percentages and Sample Numbers of the titania-doped tantala samples. Samples labelled 'Top' had coatings deposited on the side with the protruding clamping block. Samples labelled 'Bottom' had coatings deposited on the flat side of the cantilever, as illustrated in figure 4.1. 'AD' indicates sample was not heat-treated after deposition.

TiO_2 %	Sample Number	Treatment
25	7-1	AD, Bottom
25	7-2	AD, Top
55	4-1	AD, Bottom
55	4-2	AD, Top
–	4-9	AD, Uncoated

arating the mechanical loss of the coating from that of the substrate. These values are listed in Table 4.2. As with the substrates of the Hafnia samples in Section 3.4, the variation in thickness along the cantilevers leads to the thickness calculated from the bending modes to be slightly different depending on the regions probed by the resonant mode.

Table 4.2: Thickness of substrates calculated using equation 3.7. Discrepancies in thickness between modes appear to arise due to the deviation from a perfectly flat cantilever.

Sample	Mode	Frequency	Thickness [μm]
4-1	1	61	52±2
	2	439	59±2
	3	1225	59±2
	4	2398	59±2
	5	3956	59±2
	6	5899	59±2
	7	8232	59±2
	8	10952	59±2
4-2	2	321	43±2
	3	908	44±2

Continued on next page

Table 4.2 – continued from previous page

Sample	Mode	Frequency	Thickness [μm]
	4	1783	44±2
	5	2945	44±2
	6	4392	44±2
	7	6128	44±2
	8	8139	44±2
	9	10443	44±2
4-9	1	51	43±2
	2	340	46±2
	3	975	47±2
	4	1897	47±2
	5	3153	47±2
	6	4688	47±2
	7	6537	47±2
7-1	1	75	64±2
	2	505	68±2
	3	1410	68±2
	4	2750	68±2
	5	4532	68±2
	6	6793	68±2
	7	9435	67±2
7-2	1	67	57±2
	2	443	60±2
	3	1230	59±2
	4	2401	59±2
	5	3956	59±2

Continued on next page

Table 4.2 – continued from previous page

Sample	Mode	Frequency	Thickness [μm]
	6	5682	57±2
	7	8257	59±2
	8	10073	54±2
	9	12816	54±2
	10	17346	58±2
	11	21119	58±2

Visual inspection of the samples shows that the thickness of the ti:tantala coatings appears to vary across the surface of the cantilever when deposited upon the Top surface, as is visible in figure 4.1, where different thicknesses are indicated by different colours of the coating. Ellipsometric measurements were made in order to directly measure the variation. Accurate ellipsometric measurements of thickness require a reliable model of the material's complete complex index of refraction; unfortunately, such a model does not exist for titania-doped tantala. Instead, a pure tantala model was used as an approximation. While this fit may not provide an absolute measure of the thickness, it should be usable as a comparative measure between samples with the same coating.

Using the pure tantala model, it was not possible to fit thickness to the 25% titania-doped samples; however, the 55% titania-doped samples fit surprisingly well. Therefore, samples 4-1 and 4-2 were measured at four different points, shown in figure 4.2. On sample 4-1, the Bottom coated sample, fits to the ellipsometric data give roughly equivalent results for each of the four positions: a mean thickness of 488 nm with a maximum variation of only 3 nm. Sample 4-2, the Top coated sample gave much greater variation: a mean of 468 nm, and a maximum variation of 27 nm. These measurements indicate that the

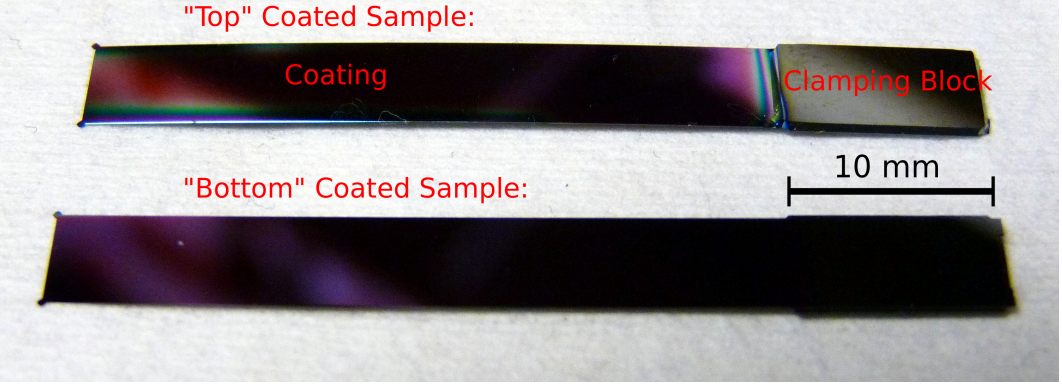

Figure 4.1: Image comparing two cantilevers coated on different sides. The top cantilever has the coating applied to the side with the projecting clamping block ('Top'), and the bottom cantilever has the coating applied to the opposite side of the substrate ('Bottom'). The coating applied to the Top shows greater variation in thickness, visible as a variation in colour across the surface.

coatings on the Top coated samples may be thinner and have a larger variation in thickness than their counterparts on the Bottom coated samples. This is consistent with information from the coating vendor's claims that it is much more difficult to apply coatings onto the top part of the cantilevers [120].

If one assumes that the ratio of thicknesses given by the tantala fits to the ellipsometer data is the same as the ratio of true thicknesses, and that the bottom coated thickness is indeed the 500 ± 10 nm specified by the coater, a ratio of $468/488 \simeq 96\%$ can be used to calculate a thickness for the coatings deposited on the Top position of the cantilevers of $0.96 \times 500 \simeq 480$ nm. In practice, the effect of using a 4%-thinner coating on the Top coated samples in equation 3.6 is to reduce the calculated coating loss by 4%. This variation is systematic and small compared to uncertainties in the coating Young's modulus and the measured mechanical losses of the coated and uncoated cantilevers. The added uncertainty in the thickness of the coatings serve to increase the uncertainties in the calculated coating losses from $\sim$14% to $\sim$19%.

Figure 4.2: Image showing the location of ellipsometry measurements made on samples 4-1 and 4-2. Locations are shown as red circled numbers.

4.3 Results

Loss measurements were made on the five samples listed in table 4.2 at the bending modes also listed in that table. Measurements were made using the same procedures discussed in Section 3.6, and at temperatures between 10 and 310 Kelvin. Of the modes that were measured on all cantilevers, only modes 3, 4, and 5 offered the full coverage of the temperature range described, especially at low temperatures, and only these three modes will be evaluated here.

4.3.1 Loss Calculations

Coating loss was calculated using the procedure described in Chapter 3. The mechanical loss of the titania-doped tantala coatings was calculated using equation 3.6. In contrast to Chapter 3 however, the difference in thickness between the coated samples and the uncoated sample (i.e. sample 4-9) lead to a discrepancy between the levels of the thermo-elastic loss of the substrates, which is not accounted for in equation 3.6. The differencing of measured mechanical losses carried out in equation 3.6 over the temperature regions where substrate thermoelastic loss is a significant fraction of the measured mechanical loss would not yield realistic values of coating mechanical loss.

In order to counteract this effect, an additional factor was added to the measured mechanical loss of the uncoated cantilever before calculating the coating mechanical loss. First, the expected thermoelastic loss of a cantilever with the same dimensions as the uncoated substrate was calculated using equation 3.9 and values from [129]. The same was done for a cantilever with the

Table 4.3: Values used in coating loss calculations, equation 3.6. Subscripts 'top' and 'bottom' refer to top and bottom coated samples, respectively. Subscripts '55%' and '25%' refer to 55% and 25% TiO_2 dopant concentrations, respectively.

Parameter	Reference	Notes
$E_s = (164 \pm 3)$ GPa	[129]	
$t_s = 43$to68 μm	See Section 4.2	From mode frequencies
$E_{c,\,55\%} = (148 \pm 5)$ GPa	See Chapter 5	From nano-indentation
$E_{c,\,25\%} = (146 \pm 3)$ GPa	See Chapter 5	From nano-indentation
$t_{s,\,top} = (480 \pm 10)$ nm	[117]	see Section 4.2
$t_{s,\,bottom} = (500 \pm 10)$ nm	[117]	see Section 4.2

same dimensions as the coated substrate. The difference between the expected thermoelastic losses was added to the measured mechanical loss of the uncoated cantilever before calculating the coating mechanical loss. An example of the expected thermoelastic losses can be seen in Figure 4.3. The spread in the expected thermoelastic loss values comes from the variation in the measured values of thermal conductivity, κ, and specific heat capacity, C, of silicon [129]. Figure 4.3 also shows the mechanical loss of the coated and uncoated cantilevers, as well as the calculated coating mechanical loss. The values used in calculating the coating mechanical loss are given in table 4.3.

The calculated coating loss for each mode can be seen in figures 4.4, 4.5, and 4.6. While the data in these plots exhibit some scatter, they can be used to discern a few features. First, the error bars are predominantly due to the uncertainty in the thickness of both the coating and the substrate. These uncertainties are systematic within each sample. Second, all coatings have broadly-similar loss values, at least within uncertainties, this suggests that for the doping levels studied, doping does not significantly alter mechanical loss at this heat-treatment. All coatings also show a broad loss peak in the 10-100 K range, similar to that found in 300° C heat-treated pure tantala coatings [109]. Finally, it appears that sample 7-2 has a lower loss at low (< 100 K) temperatures, but the loss varies greatly at higher temperatures and is often the highest at room temperature. Looking at the loss of the coated cantilever

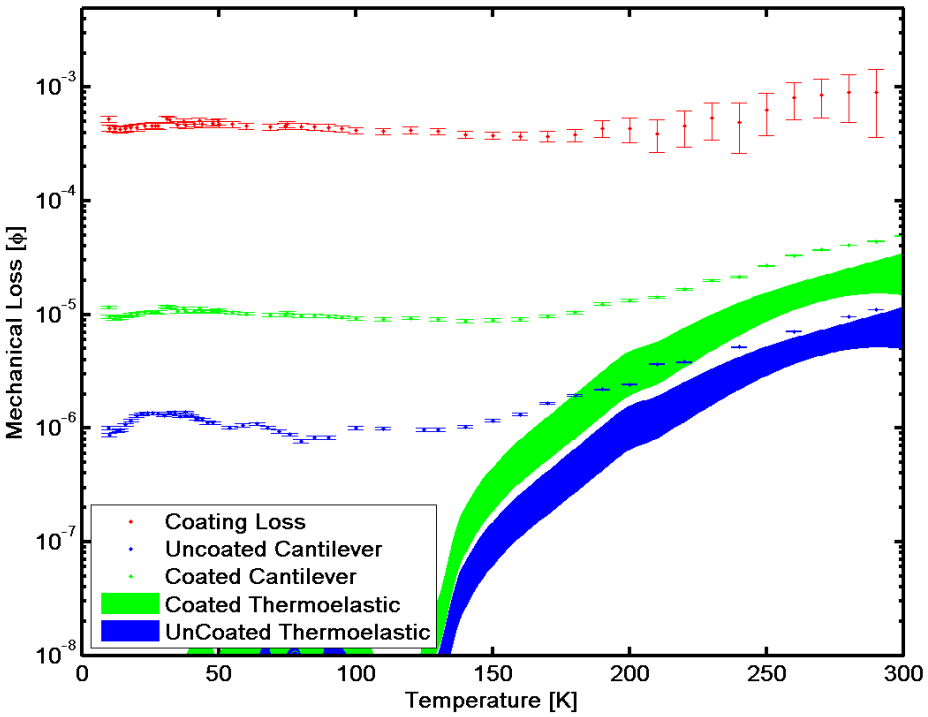

Figure 4.3: Example of the calculated coating mechanical loss compared to the measured mechanical loss of the coated and uncoated cantilevers. In order to account for differences in substrate thickness, the difference between the calculated thermoelastic losses was added to the uncoated cantilever loss before calculating the coating loss. This explains the increased uncertainty at higher temperatures, where the measured loss is dominated by the thermoelastic loss.

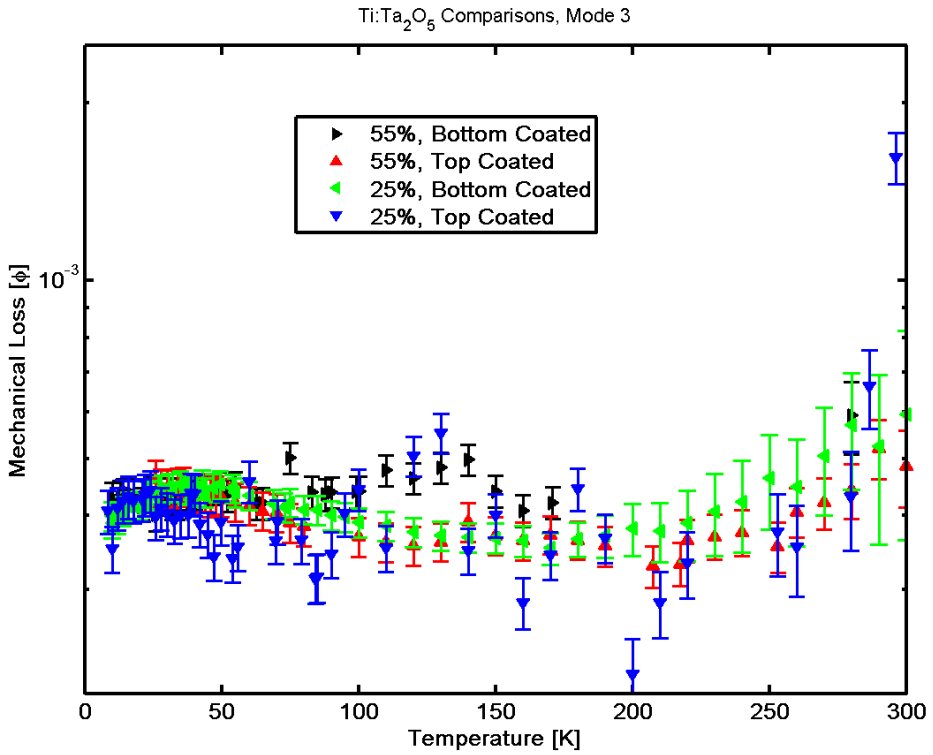

Figure 4.4: Comparison of calculated coating loss for samples 7-1, 7-2, 4-1, and 4-2 for mode 3; $f \approx 1000$ Hz.

gives some information regarding this case. Figure 4.7 shows the repeated loss measurements of one mode of sample 7-2. From this plot, it is apparent that the higher-temperature loss measurements of 7-2 were quite variable, and that the higher-temperature points come from only one clamping: a clamping that is shown to be bad at other temperatures. Sample 4-1 also may also have lower quality measurements due to the sample breaking after only one clamping. Before these two samples can be excluded from further analysis, it is important to compare them to the other samples to ensure that the coating side does not significantly impact the loss of the coating.

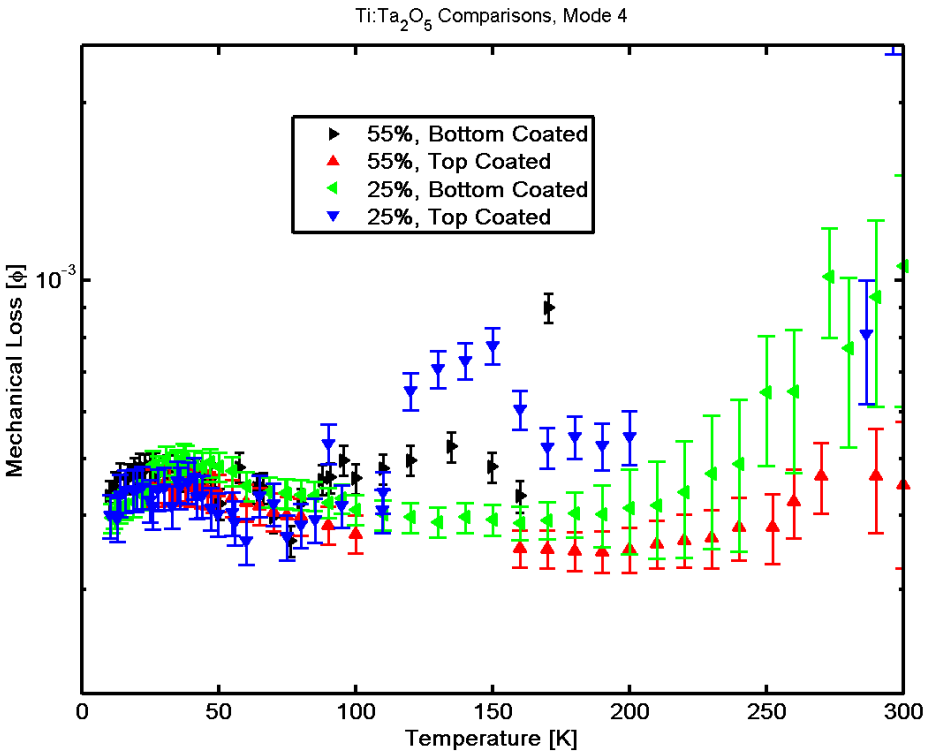

Figure 4.5: Comparison of calculated coating loss for samples 7-1, 7-2, 4-1, and 4-2 for mode 4; $f \approx 2000$ Hz.

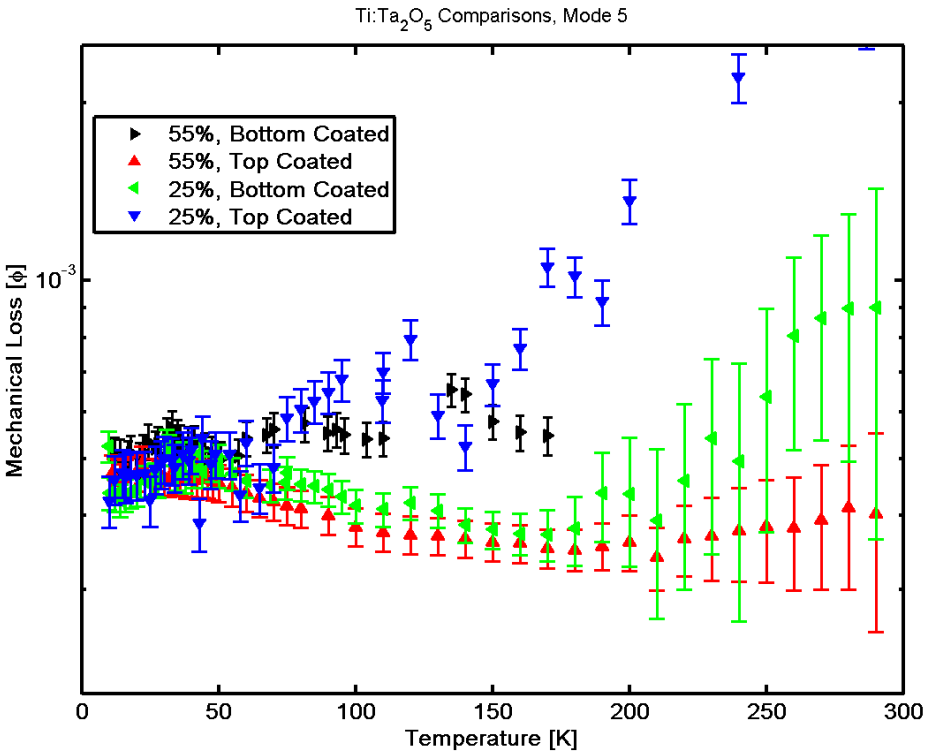

Figure 4.6: Comparison of calculated coating loss for samples 7-1, 7-2, 4-1, and 4-2 for mode 5; $f \approx 4000$ Hz.

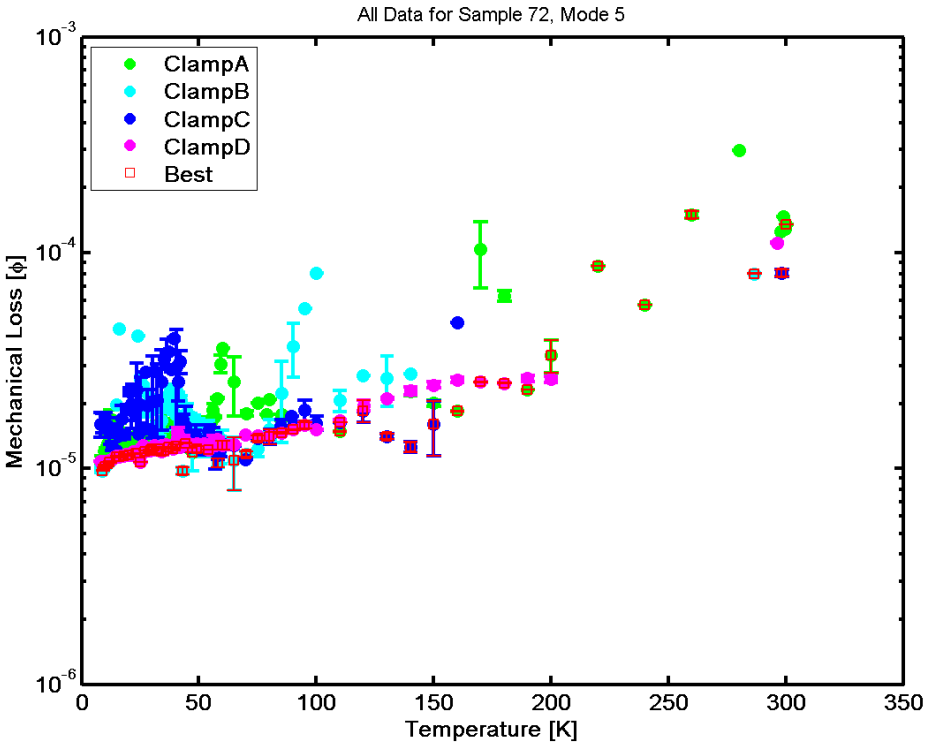

Figure 4.7: Repeated measurement cycles of mode 5 of sample 7-2 showing that the measured loss at temperatures greater than ≈ 100 K are of fairly poor quality. Measurements show great variability and are chosen from Clamp A, a clamping that is not generally selected in lower temperature regions, an indication that is is a poor clamping.

4.3.2 Comparing Top and Bottom Coatings

Comparing the calculated coating mechanical loss between top and bottom coated samples can give an indication of the effects of surface treatment on the mechanical loss of the coating. In addition, as it has been shown, the thickness of the coatings deposited on the top-coated samples is of greater variability, and this too might have an effect on the coating mechanical loss. Figures comparing the coating mechanical loss calculated for the fourth bending mode of the samples can be seen in figure 4.8 for 55% titania-doped tantala (Samples 4-1 and 4-2), and in figure 4.9 for 25% titania-doped tantala (Samples 7-1 and 7-2).

Comparing samples 4-1 and 4-2, it is apparent that there is no significant difference in mechanical loss between the two samples, especially at temperatures below 100 K, where the loss peak is located. Although the data from sample 4-2 only go as low as 27 K, they are generally cleaner and allow better analysis of the loss peak.

The Comparison between 7-1 and 7-2 is slightly more difficult. Individual temperature points for sample 7-2 all tend to lie reasonably close to their counterparts taken from sample 7-1; however, the data from sample 7-2 are more variable, and generally of lower quality, as discussed above. At low temperatures, the calculated mechanical losses for the coating on sample 7-2 are lower than those on sample 7-1 for all modes. It is important to remember, however, that the ellipsometric measurements used to calculate the relative thickness of the coatings was made on samples 4-1 and 4-2, and the ratio of thicknesses might not be the same on these samples. If the coating on sample 7-2 is thinner than the estimated 480 nm, the mechanical loss would be higher. In the analysis that follows, however, the magnitude of the loss is not as important as the position of the loss peak, which does not appear effected by the deposition side.

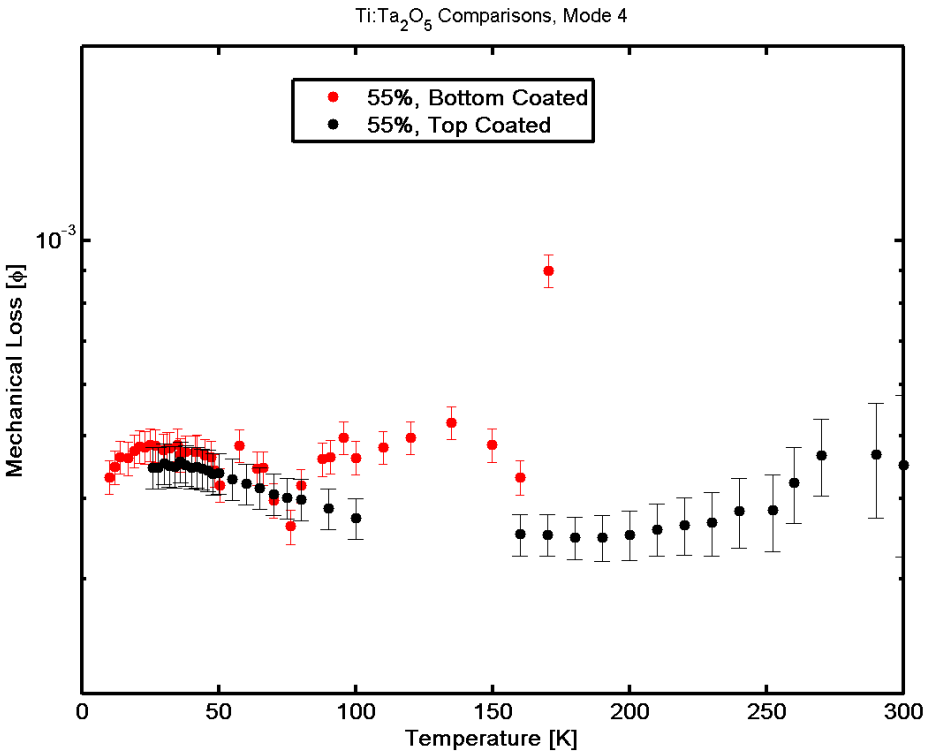

Figure 4.8: Comparison between the calculated coating loss of top and bottom coated 55% Ti:Ta_2O_5 samples. This mode is representative of all three modes measured.

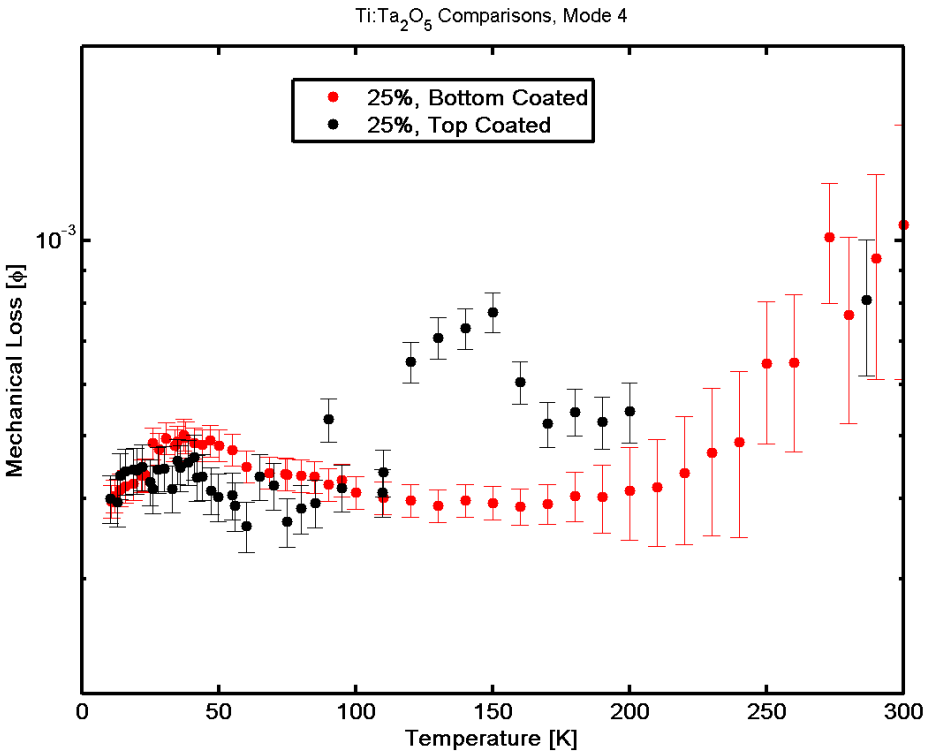

Figure 4.9: Comparison between the calculated coating loss of top and bottom coated 25% Ti:Ta_2O_5 samples. This mode is representative of all three modes measured.

4.4 Analysis

In the above sections, the mechanical loss of 25 and 55% TiO_2 doped Ta_2O_5 coatings has been measured and compared between two different substrate surfaces (top and bottom) and apparent deposition conditions (flat face vs. face with clamping block). These results seem to indicate that besides the increased variation in coating thickness associated with coating on the top side of the cantilevers, the coating mechanical loss does not seem to vary beyond the current sensitivity of loss measurements. This being the case, further analysis can be done on the best representatives of each of the two titania doping samples: 4-1 and 7-2. Comparing the data from these two samples clearly shows the broad loss peak around 30 K, as in Figure 4.10.

If one assumes that this peak is a type of arises from Debye-like processes, the loss, $\phi(\omega)$, for the peak should follow the relation [51]:

$$\phi(\omega) = \Delta \frac{\omega\tau}{1 + (\omega\tau)^2}, \tag{4.1}$$

where Δ is a constant related to the magnitude of dissipation, and τ is described by the Arrhenius equation [107]:

$$\tau^{-1} = \tau_0^{-1} \exp\left(-\frac{E_\mathrm{a}}{\mathrm{k_B T}}\right). \tag{4.2}$$

Here, τ_0^{-1} is the rate constant of the dissipation mechanism, E_a is the activation energy, and $\mathrm{k_B}$ is Boltzmann's constant. At the dissipation peak, $\omega\tau = 1$, which, combined with equation 4.2, gives the convenient linear relation:

$$\ln(\omega) = \ln(\tau_0^{-1}) - \frac{E_\mathrm{a}}{\mathrm{k_B}} T^{-1}. \tag{4.3}$$

Thus, plotting the natural logarithm of the mode frequency against the inverse of the temperature at the loss peak should yield a line with the slope defined by the activation energy of the process and an intercept defined by the rate

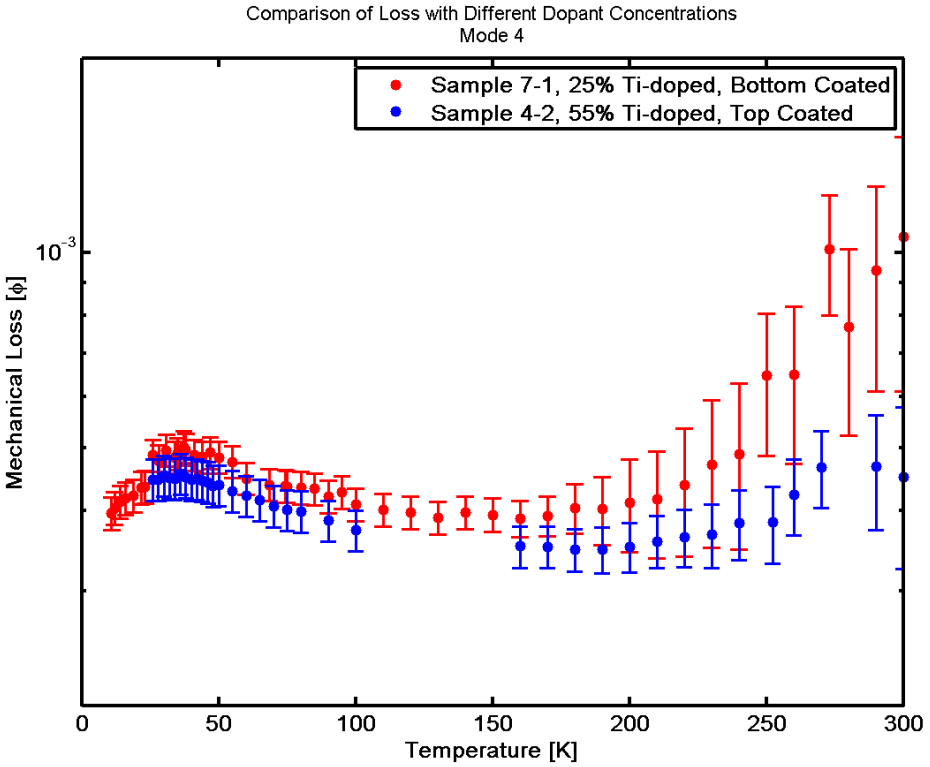

Figure 4.10: Calculated coating mechanical loss for the fourth bending mode of samples 7-1 and 4-2. A broad loss peak below 100 K, centred around 30 K, is visible.

constant.

In order to find the location of the loss peak, a fourth-order polynomial was fit to the mechanical loss data for each mode at temperatures below 100 K. Peak positions were found by calculating the lowest temperature where the derivative of the polynomial was equal to zero. The fourth-order polynomial was found to fit well to data within this temperature range and to give reasonable measurements for the position of the first peak. Uncertainties in the peak position were found by subtracting the fit polynomial from the data, calculating the mean and standard-deviation of the residuals, and building 1000 'noisy' models by generating Gaussian noise to add back to the original fit. These noisy models were then fit using the same technique as the original

Table 4.4: Located loss peak temperatures and frequencies used in calculating the activation energy and rate constant.

Sample 7-1		
Mode	T_{peak} [K]	Frequency [Hz]
1	34.5 ± 1.6	75
3	41.1 ± 0.8	1416
4	41.2 ± 1.1	2769
5	44.6 ± 3.3	4557
7	41.5 ± 1.6	9477
Sample 4-2		
Mode	T_{peak}	Frequency [Hz]
3	15.0 ± 36.4	911
4	30.1 ± 2.3	1786
5	24.2 ± 2.3	2952
6	25.7 ± 2.0	4404
7	29.0 ± 5.9	6142
8	33.2 ± 3.8	8166

model, and the variation in peak position recorded. Using this method, it was possible to find the peak position for most modes.

A plot of a typical fit to the data can be seen in figure 4.11. The results of all three modes are given in table 4.4. Using only modes 3, 4, and 5 to calculate the Arrhenius relation gives the Arrhenius plots shown in figures 4.12 and 4.13. Data from sample 7-1 give a good linear relationship with activation energy $E_a = 47.4 \pm 64.5$ meV and a rate constant of $\tau_0 = 1.39 \pm 0.08 \times 10^{-10}$ s. Sample 4-2 does not appear to give a sensible result, with $E_a = -4.0 \pm 2.9$ meV and $\tau_0 = 4.03 \pm 3.28 \times 10^{-4}$ s. This can be compared to the activation energy of the loss peak found in pure tantala heat-treated to 600° C, where the activation energy was found to be $E_a = 28.6 \pm 1.2$ meV, and the rate constant $\tau_0 = 5.9 \pm 0.2 \times 10^{-12}$ [106]. The loss peak measured in the referenced paper, however, was much sharper and with higher loss, so it is not unexpected that the activation energy and rate constant found for sample 7-1 would be similar but not equal.

The fits might be improved upon with more points for fitting the Arrhenius

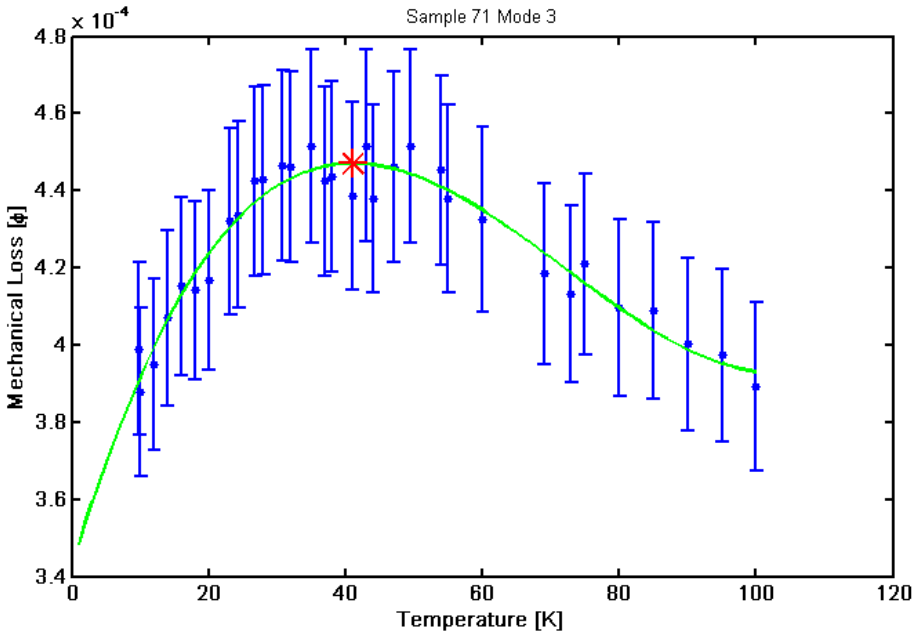

Figure 4.11: Example fourth-order polynomial fit to loss data below 100 K. The red asterisk shows the location of the peak. In this example, uncertainty in the peak position is smaller than the marker.

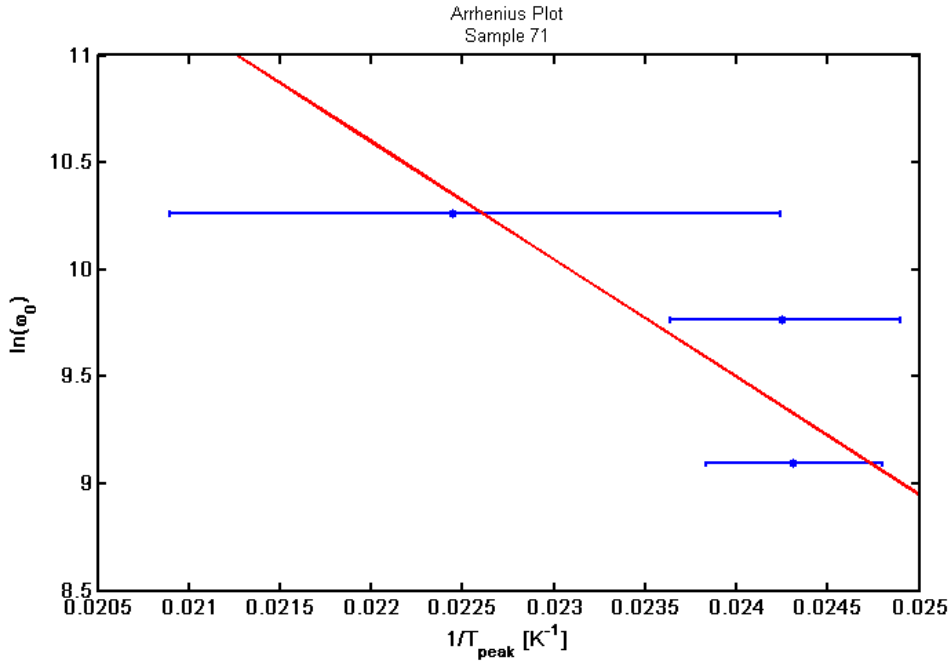

Figure 4.12: Arrhenius plot of data from modes 3, 4, and 5 of sample 7-1.

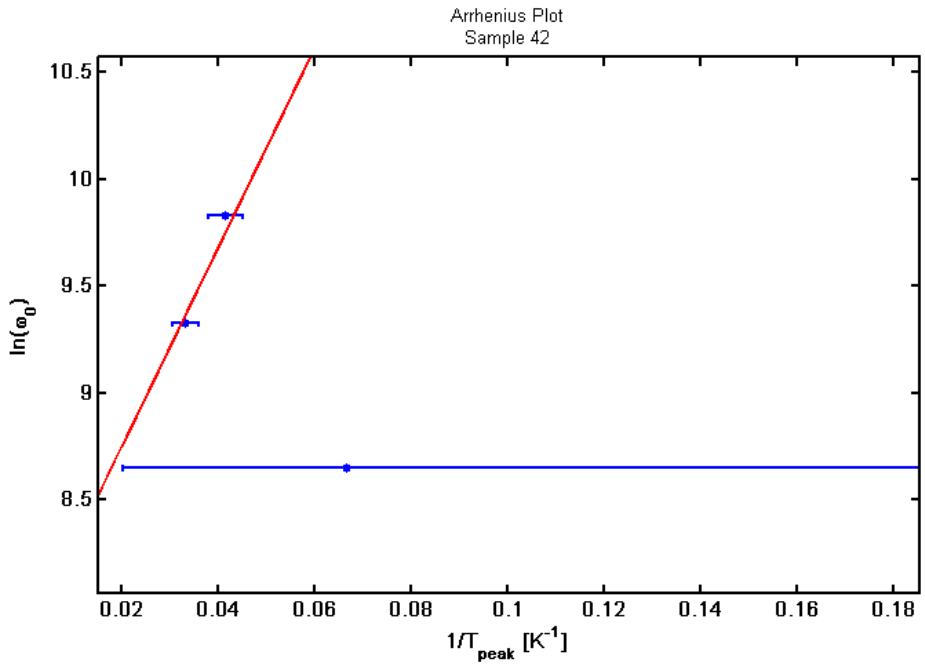

Figure 4.13: Arrhenius plot of data from modes 3, 4, and 5 of sample 4-2.

relation. In order to achieve this, the coating mechanical loss below 100 K was calculated using additional modes of the coated cantilevers for which there were no matching data from the uncoated cantilever. This was done in the same way as discussed in Section 4.3.1, but using the nearest-frequency mode for the uncoated sample. In this way, the loss for modes 6, 7, and 8 of sample 4-2, and mode 7 of sample 7-1 were calculated using mode 5 of sample 4-9 for the uncoated data, and the loss of mode 1 of sample 7-1 was calculated using mode 3 of sample 4-9. This was deemed reasonable, as there appears to be little variation in the mechanical loss of sample 4-9 with frequency at temperatures below 100 K, and the uncoated loss is so low at these temperatures that the mechanical loss of the coated samples is almost entirely dominated by the coating loss. The peak locations for the additional modes are also shown in table 4.4.

Figures 4.14 and 4.15 give the Arrhenius plots using all the modes given in table 4.4. For sample 7-1, the fit line gives an activation energy of $E_{\mathrm{a}} =$

61.9±24.0 meV and a rate constant of $\tau_0 = 1.90 \pm 0.28 \times 10^{-12}$ s. The addition of additional data, especially the mode 1 peak location, has allowed the activation energy to be better constrained, however, the rate constant appear to be highly variable due to its logarithmic dependence on the y-intercept of the fit line. The fit for sample 4-2 appears to be slightly improved, giving a more realistic and better constrained activation energy of $E_a = 3.8 \pm 0.9$ meV however, the rate constant is still difficult to interpret, having a value of $\tau_0 = 0.94 \pm 1.51 \times 10^{-5}$ s.

At this point, the data from sample 7-1 appears to be consistent with similar measurements and without need of further analysis on this front. The data from sample 4-2 remains difficult to interpret due to the low activation energy and high rate constant found by the fits. The difficulty appears to arise from sample 4-2 having fewer loss measurements at the temperatures of interest. This can be seen best in figure 4.16, which shows the calculated coating mechanical loss measured for the third bending mode of sample 4-2. The peak of the loss appears at lower temperatures than the measured loss data, yielding large uncertainties. A similar example can be seen in figure 4.17, showing data from the fourth bending mode of sample 4-2. In this case, the peak found from the fit appears within the measured loss data, however, the data show no low-temperature fall-off to match the green fit line. This may indicate that the lowest temperature points bias the fit, and subsequently miss-identify the peak location.

The modes given as examples above are the two worst cases of these problems for sample 4-2, so it is not unreasonable to consider the Arrhenius plot for sample 4-2 without these points. This is given in figure 4.18. The figure shows a much better fit which gives an activation energy of $E_a = 7.3 \pm 1.2$ meV and a rate constant of $\tau_0 = 1.47 \pm 2.78 \times 10^{-6}$ s. It seems as though the data from sample 4-2 will not yield a result as reliable as that of sample 7-1. However, the data do suggest that the Activation energy for highly titania-doped tan-

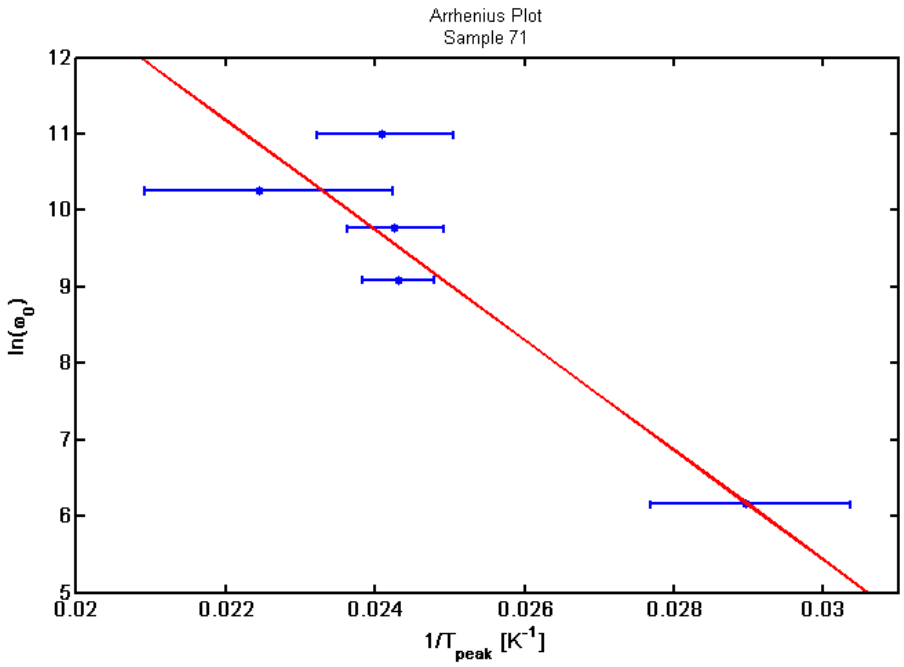

Figure 4.14: Arrhenius plot of data from all modes given in table 4.4 for sample 7-1.

tala (sample 4-2, 55%) is lower than that of 25% titania-doped tantala (sample 7-1).

4.5 Conclusions

The mechanical loss of 25 and 55% titania-doped tantala thin-film coatings deposited by ion beam sputtering has been measured for samples with no heat-treatment. Measurements were made from coatings deposited on both etched and polished surfaces, and found to have little variation in mechanical loss with surface preparation. Furthermore, when compared to the mechanical loss of 300° C heat-treated pure tantala coatings [109], as in figure 4.19, the titania doping and additional heat-treatment does not appear to have any significant effects on the mechanical loss at low temperatures. Further analysis of the broad loss peak centred around 30 K in sample 7-1 shows the activation energy and rate constant for the loss mechanism to be similar to that of a sharper

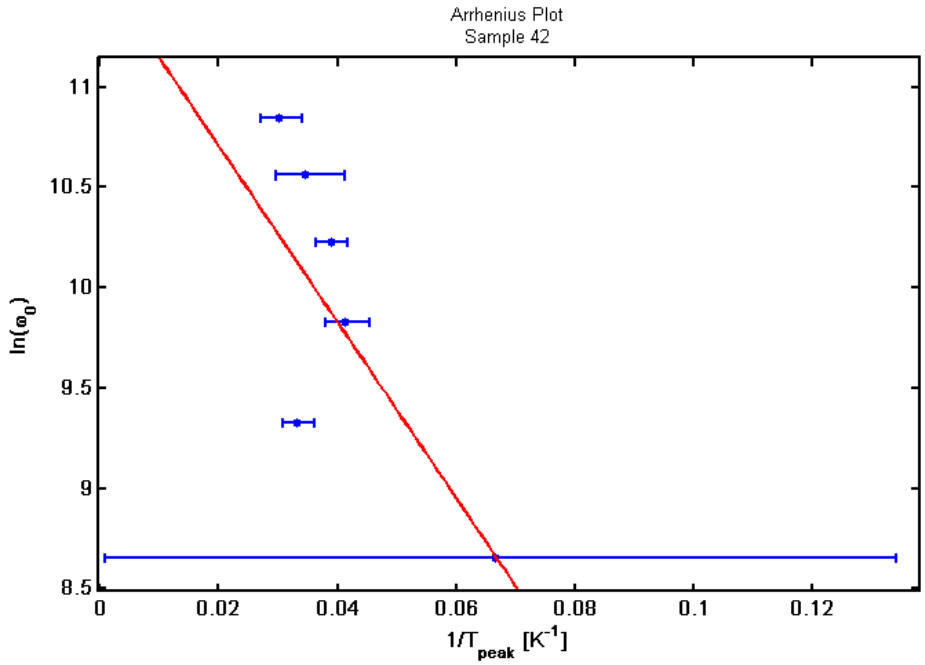

Figure 4.15: Arrhenius plot of data from all modes given in table 4.4 for sample 4-2.

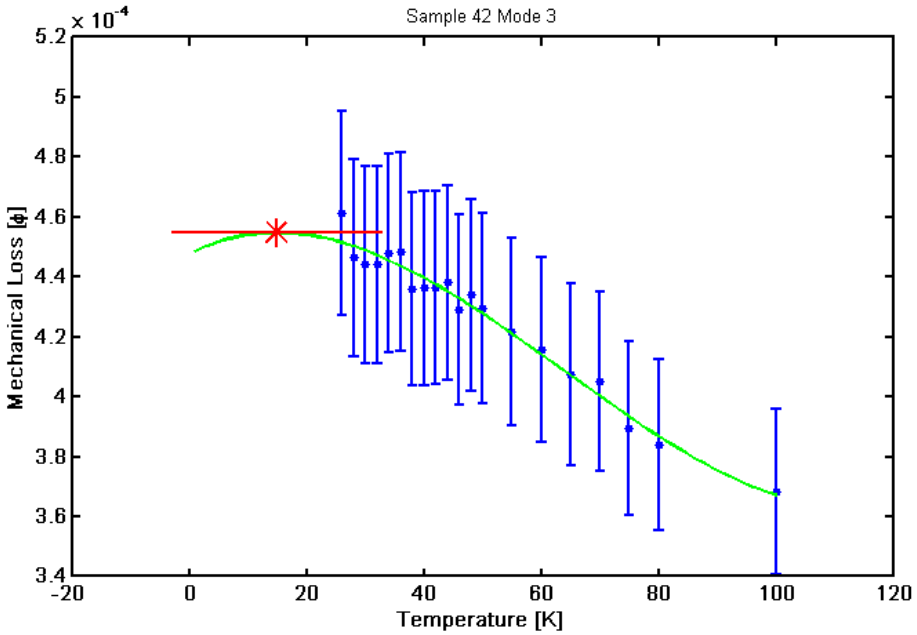

Figure 4.16: Example fourth-order polynomial fit to loss data below 100 K for sample 4-2, mode 3. The red asterisk shows the location of the peak outside the measured data.

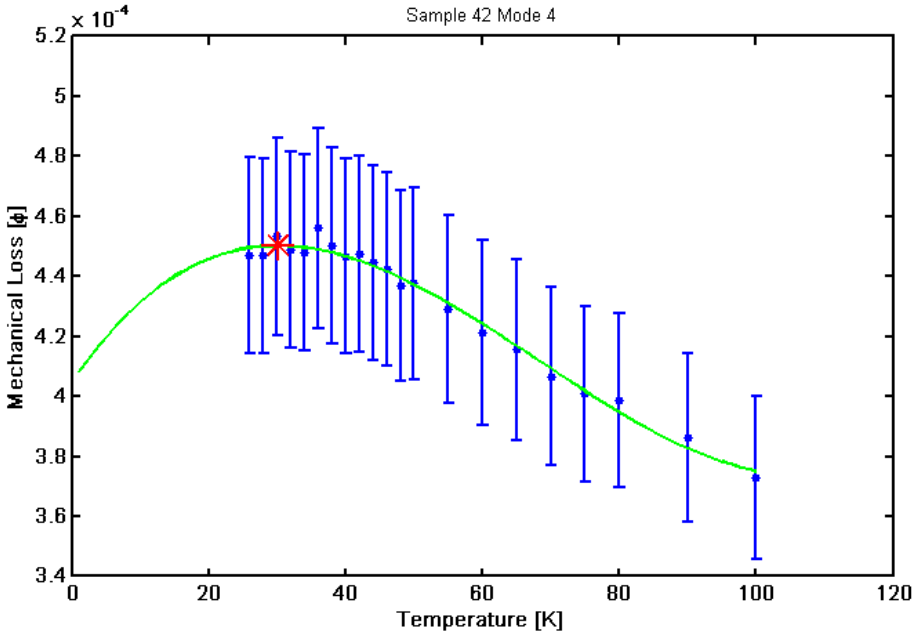

Figure 4.17: Example fourth-order polynomial fit to loss data below 100 K. The red asterisk shows the location of the peak. The low-temperature fall-off does not appear in the measured data, and the lowest-temperature measured points may bias the fit.

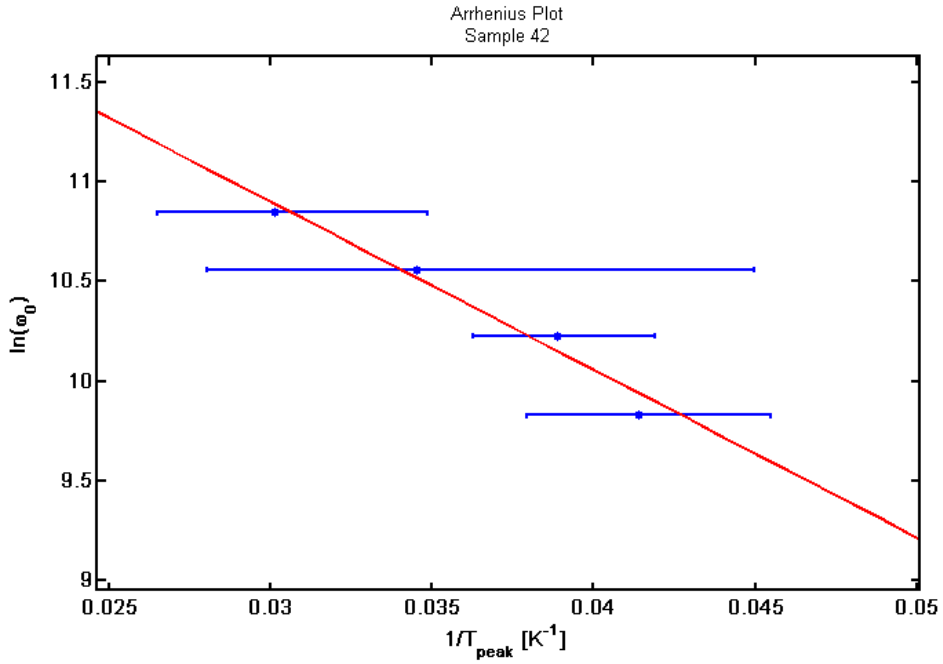

Figure 4.18: Arrhenius plot of data from modes 5, 6, 7, and 8 of sample 4-2.

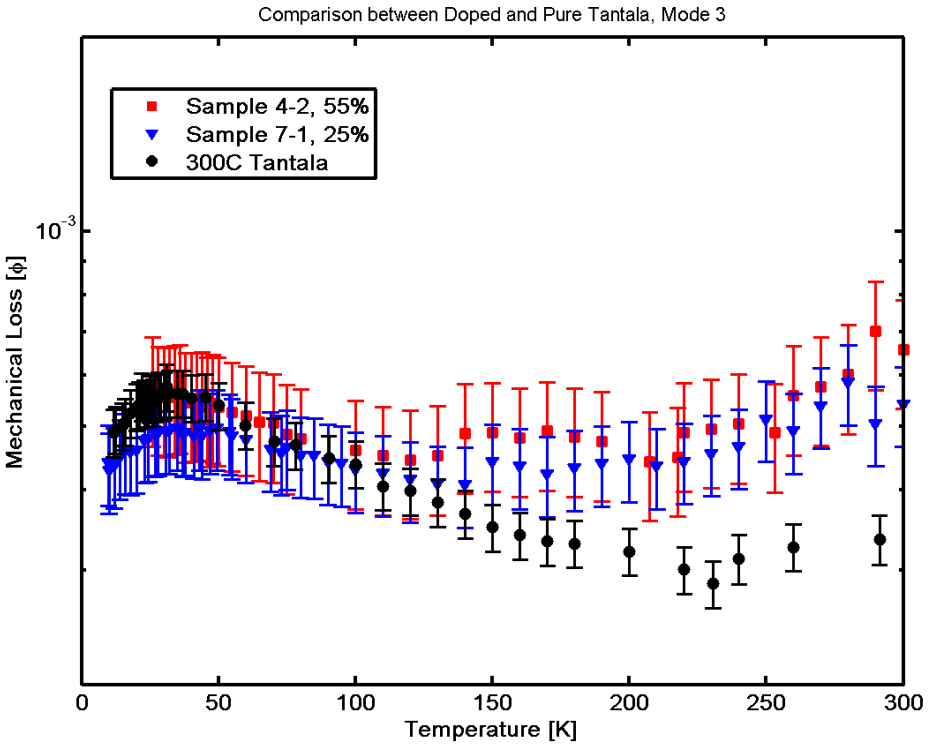

Figure 4.19: Comparison of the mechanical loss measured for pure tantala [109], 25 and 55% titania-doped tantala (this work) for the third bending mode, $f \sim 1000$ Hz.

peak found in 600° C heat-treated pure and 14.5% titania-doped tantala [106], but with a higher activation energy. Analysis of the loss peak in sample 4-2 was inconclusive, but seems to indicate a much lower activation energy.

Chapter 5

Thin-film Young's Modulus Measurements Using Nano-Indentation

It is apparent from the previous two chapters that a good knowledge of the coating Young's modulus is necessary to evaluate the coating loss. Young's moduli are measured most commonly on bulk samples of a material, and it is not a given that the mechanical properties of a material in the form of thin film coatings will be same as the bulk material. Therefore, it is necessary to measure the coating Young's moduli directly. As the coatings are only a few hundred nanometers thick, it is important to use a small-scale method of measuring the Young's modulus. Nano-indentation is one such method that is fairly well established.

Nano-indentation is a method of measuring the elastic and plastic properties of a material by pressing a stiff tip into the surface of a material using controlled forces and penetration depths. The depth of penetration and the force on the tip are recorded, and the material responses are extracted from the force-depth relationship. Further processing is required to extract the elastic properties of the substrate from those of the coating by measuring the proper-

ties at a range of depths and extrapolating the modulus-depth relation to zero depth using a model of the coating-substrate system.

This chapter presents nano-indentation measurements on a number of materials deposited for mechanical loss studies as materials of interest to the gravitational wave community. The first section, 5.1, introduces nano-indentation and the extraction of a modulus using the Oliver and Pharr method [136]. Section 5.2 describes the samples used in the indentation measurements. The experimental method and apparatus are described in section 5.3, and the analysis of the indentation measurements are presented in section 5.4. The final results are given in section 5.5, and the findings are discussed in the final section, 5.6.

5.1 Introduction

Nano-indentation is a technique developed to measure the mechanical properties of small volumes of materials in a simple fashion [137]. It measures properties by making indentations at the nanometre scale and recording the load, P, and displacement, h, response as the indenter is driven into and withdrawn from the material. An example of a nano-indentation load-displacement curve can be seen in figure 5.1. In this example, the indent is made using the standard loading-hold-unloading cycle. A load is applied to the indentation tip, forcing it into the sample and increasing the displacement. During the loading phase, work is done as the sample is both elastically and plastically deformed. During the hold phase, the force is held constant, but the sample continues to deform due to creep effects which arise due to the movement of the material within the specimen under high pressure. During the unloading phase, the load is reduced and the indentation tip is withdrawn from the sample. This phase is characterized by only having an elastic response, and so it is often the unloading phase that is analysed in order to gain knowledge about

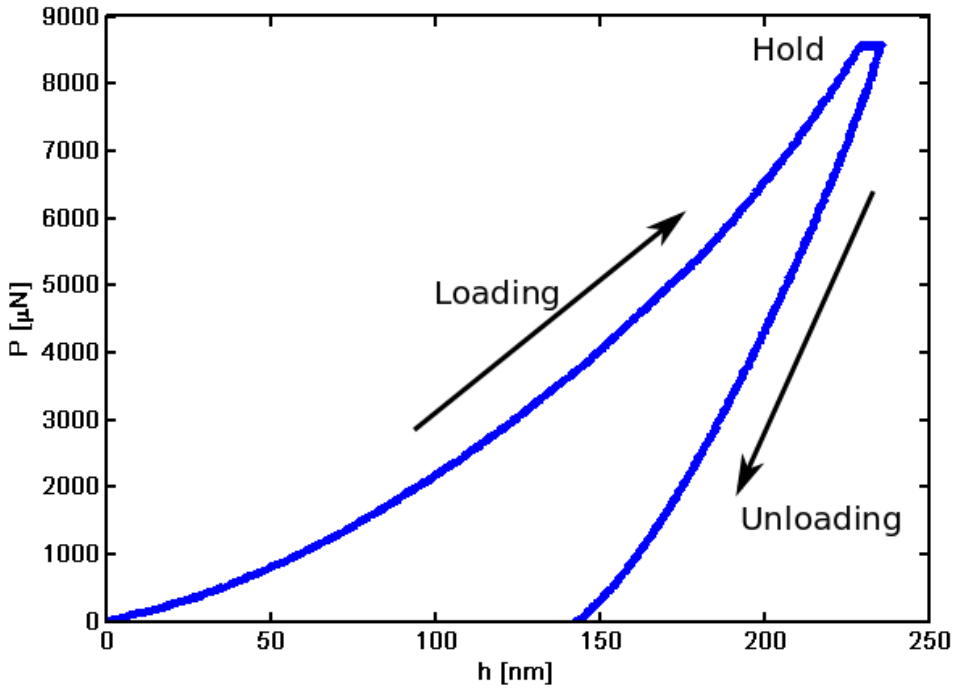

Figure 5.1: Example of a 'Load-Displacement' plot made using nano-indentation during a standard loading-hold-unloading cycle. The vertical axis is the force exerted by the indentation tip, or load (P), and the horizontal access is the displacement (h) of the tip into the surface of the sample.

the elastic properties of the material. The area under the curve is the work done in deforming the sample, and can also be analysed [138].

A schematic of a nano-indentation apparatus is given in figure 5.2. Designs vary between manufacturer, but in most cases, the load is applied using magnetic or electrostatic repulsion, and displacement is sensed using a parallel plate capacitor. In many cases, additional load may be applied through the use of piezoelectric materials mounted below the sample or above the tip. These combined features allow for load sensitivities less than 100 nN and sub-nanometre displacement sensitivities [139]. The indentation tip is usually a Berkovich indenter, characterized by its three-sided pyramidal shape with a face angle of 68°. For nano-indentation, indenters are constructed of single-crystal diamonds for their hardness. The tip radius of a new Berkovich indenter

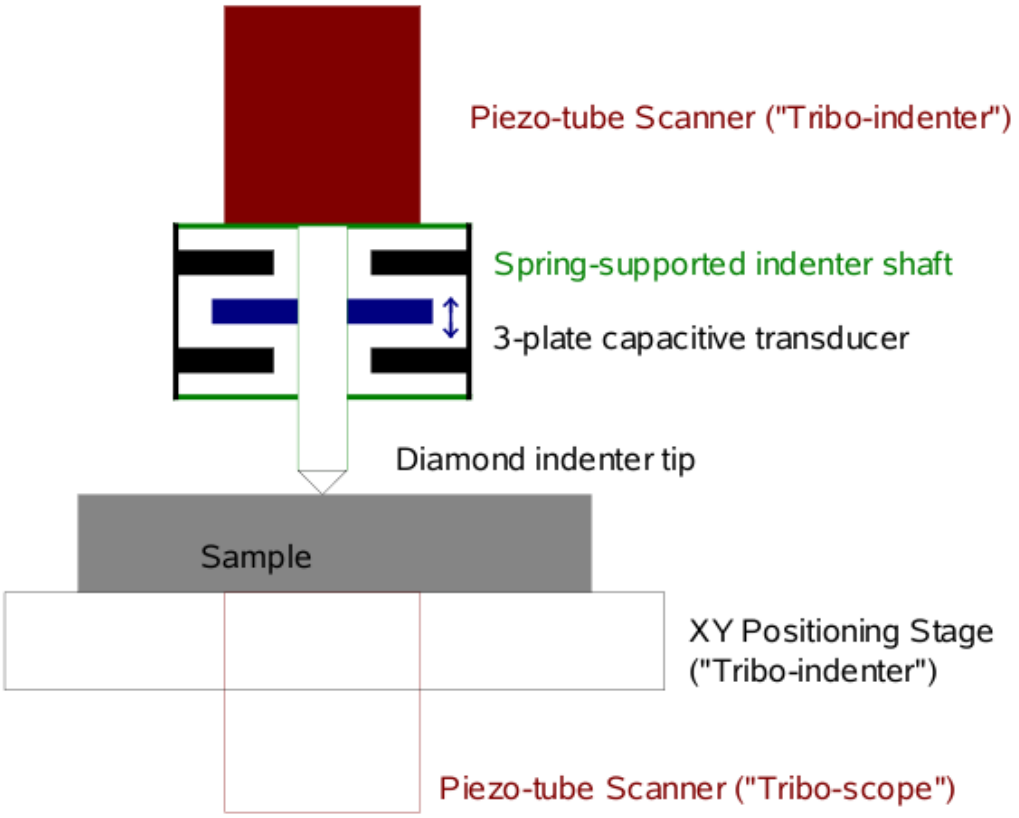

Figure 5.2: Schematic representation of a Hysitron nano-indentation machine. Recreated with permission from [141].

is in the order of 50-150 nm [140].

5.1.1 Extraction of Young's Modulus from Indentation Using the Oliver and Pharr Method

Various methods have been developed to extract the elastic modulus from indentation data [136; 142; 143]; however, the method of Oliver and Pharr [136; 144] is the most commonly used. Once the load-displacement data is recorded, the elastic modulus is determined from

$$E^* = \frac{\sqrt{\pi}}{2}\frac{dP}{dh}\frac{1}{\sqrt{A}}, \tag{5.1}$$

where A is the projected area of contact under load, dP/dh is the slope of the load-displacement curve at the beginning of the unloading phase, and E^* is the combined modulus of the sample and indenter:

$$\frac{1}{E^*} = \frac{1-\nu_{\mathrm{i}}^2}{E_{\mathrm{i}}} + \frac{1-\nu_{\mathrm{s}}^2}{E_{\mathrm{s}}}. \tag{5.2}$$

Here, E is the Young's modulus, and ν is the Poisson's ratio of the sample and indenter, marked with subscripts 's' and 'i', respectively.

The value of dP/dh is generally extracted from the data by fitting an the empirically-derived equation

$$P = \alpha(h - h_{\mathrm{f}})^m, \tag{5.3}$$

to the unloading portion of the curve. Here, α and m are the fitting constants, and h_{f} is the displacement at zero load on the unloading curve (seen in figure 5.3). Once fit, the derivative of the P-h relation is taken at the maximum value of h, $h_{\max}$ to give the value of dP/dh.

Next, it is necessary to measure the projected area of contact, A. For a perfect Berkovich indenter, the area function is [136]:

$$A = 24.5h_{\mathrm{c}}^2, \tag{5.4}$$

where h_{c} is known as the 'contact depth', calculated as,

$$h_{\mathrm{c}} = h_{\max} - \epsilon\frac{P_{\max}}{dP/dh}, \tag{5.5}$$

where $P_{\max}$ is the maximum load and ϵ is a semi-empirical value that takes into account the shape of the indenter and non-uniformities in the material response. ϵ is modelled to be 0.72, but is generally taken to be 0.75 to further account for non-uniformities [140].

Of course, the indenter tip is not a perfect Berkovich shape. A perfect

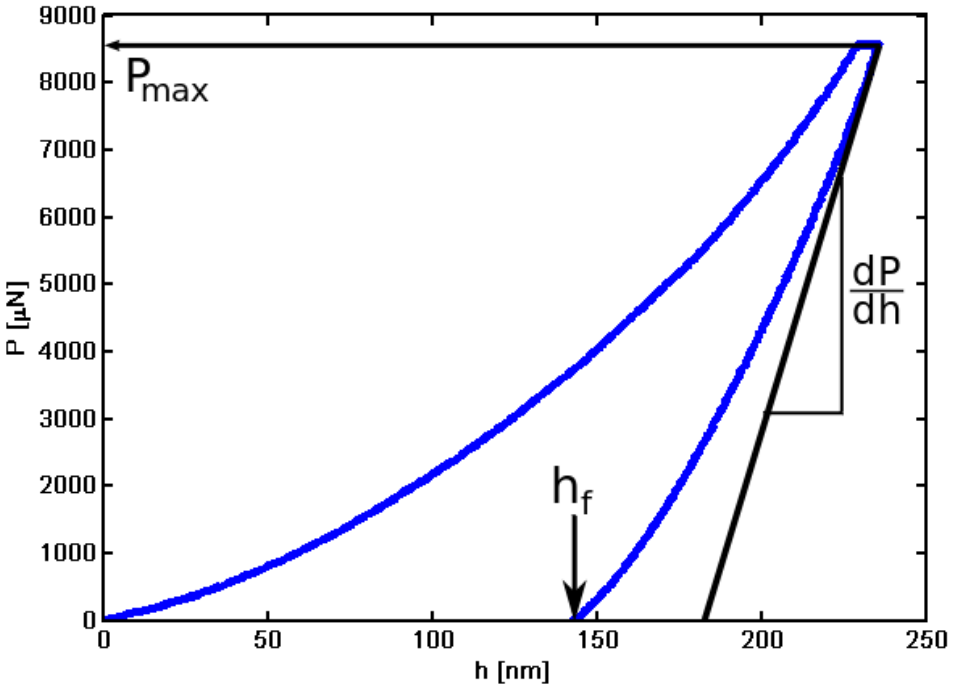

Figure 5.3: Example of an indent showing important measured parameters.

Berkovich would have zero radius of curvature at very small penetration depths. The ideal geometry often breaks down near the very tip, where tip rounding has occurred. This can be through the regular use of the indenter tip or just from the manufacturing process. Instead, an area relation of the following form is used [136]:

$$A = C_1 h_c^2 + C_2 h_c + C_2 h_c^{1/2} + C_4 h_c^{1/4} + \dots \tag{5.6}$$

Here, C_1 is usually a number close to 24.5, and the remaining constants are fit to indents made into samples of known modulus at different depths in order to account for tip rounding.

5.1.2 Separating Coating Modulus from Effective Modulus using the Song and Pharr Model

For a thin coating on much thicker substrate, if the Young's moduli of the coating and substrate differ, the modulus measured using the Oliver and Pharr method will vary with indentation depth [145]. This is due to the increasing influence of the substrate as the load is increased. In order to minimise this influence, it is often suggested that indents be made such that $h_{\max}$ is less than 10% of the thickness of the coating, t_c [136]. While this is generally acceptable for coatings greater than about a micrometre, it is not practical on thinner coatings where the errors in the area function and surface defects begin to have an effect at very small indentation depths [140].

The number of models developed to extract the coating modulus, E_c, from the combined modulus, E', measured for a coating-substrate system are too numerous to present here. However, reference [137] does an excellent job of covering many of them. In most models, the moduli can be separated using the relation:

$$E' = E_s + (E_c - E_s)\Phi(x), \tag{5.7}$$

where E_s is the substrate modulus, and $\Phi(x)$ is a weighting function characterized by the relative penetration, x. In this case, $\Phi = 1$ indicates zero penetration, and $\Phi \to 0$ for large depths where the modulus is dominated by the substrate. This provides a simple linear relationship for fitting the combined modulus versus depth data that is measured in the indentation process. A plot of the combined modulus versus the weighing function will give a linear relationship with the y-intercept of E_s, and a slope of $E_c - E_s$. In comparing the efficacy of each model, it was found, again in [137], that the model developed by Gao [146] provided the most accurate results. It was later found, however, that a model developed by Song and Pharr [147], but based on Gao's model, provided even better results [148]. It is this model, henceforth called the Song and Pharr model, which is used in this study and is described here.

In the Gao model, The Young's modulus of the film-substrate system measured at a specific depth is calculated for a thin layer on a infinitely thick substrate. The resulting equation for the Young's modulus is given as:

$$E'(x) = E_s + (E_c - E_s)I_0(x). \tag{5.8}$$

Here, E' is the Young's modulus of the film-substrate system measured at a specific depth, characterized by the variable x. E_s and E_c are the Young's moduli of the substrate and film, respectively, $I_0(x)$ is a function that weighs the effect of the substrate on the combined modulus, making equation 5.8 equivalent to equation 5.7 with $\Phi(x) = I_0(x)$. x is defined as $x = t/a$, where a is the radius of a circle with the equivalent area as the projected area of indent, $\pi a^2 = A(h_c)$, and t is the thickness of the film. I_0 is defined as:

$$I_0 = \frac{2}{\pi}\arctan(x) + \frac{1}{2\pi(1-\nu)}\left[(1-2\nu)x\ln\left(\frac{1+x^2}{x^2}\right) - \frac{x}{1+x^2}\right], \tag{5.9}$$

where ν is a Poisson's ratio between those of the coating and substrate, as equation 5.9 was derived under the assumption that the coating and substrate

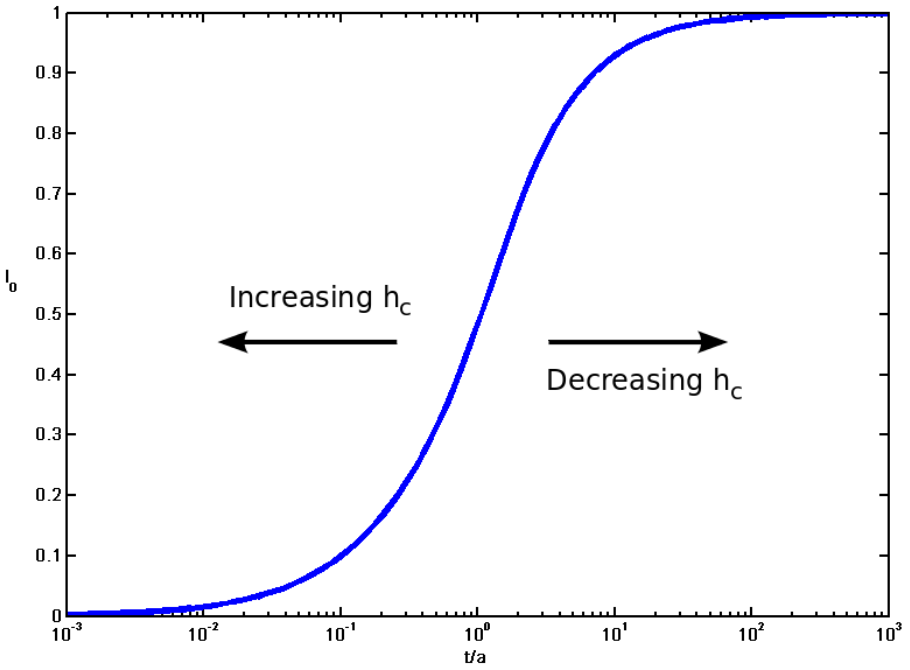

Figure 5.4: Plot of equation 5.9, where $x = t/a$.

have equivalent moduli [146]. In practice, the Poisson's ratio for amorphous oxides is generally in the range of 0.2-0.4, and the effect of varying ν within this range changes the value of I_0 by less than 8%. In the measurements below, $\nu = 0.2$, as the Poisson ratios are expected to lie between those of silica ($\nu = 0.17$ [129]) and silicon ($\nu \sim 0.27$ [112]). A plot of the value of I_0 versus x can be seen in figure 5.4. This figure also shows that an increasing h_c decreases the value of x and drives $I_0 \to 0$, demonstrating that a deep indent will yield the Young's modulus of the substrate, while a shallow indent drives $I_0 \to 1$ and yields a modulus close to that of the coating.

The Song and Pharr model is largely based on the Gao model, but with one important distinction. In the Song and Pharr model, it is recognized that moduli add like springs in a series, but with similar weighting. Song's

equivalent to equation 5.8 is:

$$\frac{1}{E'} = \frac{1}{E_\mathrm{s}} + \left(\frac{1}{E_\mathrm{c}} - \frac{1}{E_\mathrm{s}}\right) I_0. \tag{5.10}$$

This is similar to equation 5.7, but with the moduli inverted. In the similar manner as equation 5.7, a plot of E'^{-1} against I_0 for a number of indents made at different depths will yield a linear relationship with y-intercept of E_s^{-1} and slope of $E_\mathrm{c}^{-1} - E_\mathrm{s}^{-1}$.

Finally, it was noted in reference [148] that the models give the closest extrapolation of the coating modulus if instead of using $x = t/a$, a value of $x = (t - h_\mathrm{c})/a)$. This is intuitively understandable, as the effect of the substrate should scale with the distance from the applied load to the substrate, which will not be the full thickness of the substrate, especially when $t/a \simeq 1$. However, this approximation does not apply when $h_\mathrm{c} > t$, as negative values of x are unphysical. At large values of h_c, I_0 is already approaching zero, and the effect of the coating modulus is too small to be extracted. Thus, it is favorable to get a wide range of indentation depths, but for the extrapolation of the coating modulus, small values of h_c are preferable. Fortunately, for the measurements in this study, h_c does not exceed 40% of t.

5.2 Sample Preparation

Various samples of pure tantala and titania-doped tantala, as well as hafnia and amorphous silicon (a-Si) were indented in order to find their Young's moduli. Coatings were applied to both silica and silicon substrates. A list of the samples measured can be seen in table 5.1. Coatings were deposited on two different substrates: silica witness samples (SiO_2) and silicon (Si) cantilevers. The silica witness samples are fused silica discs 1 inch in diameter and 1/4 inch thick produced to accompany silicon cantilevers used in loss measurements like those in chapters 3 and 4 and are used in additional measurements of optical

and mechanical properties. The witness samples are coated in the same coating chamber as the cantilevers, and undergo the same heat-treatments. This allows the characterization of the coatings even through destructive means without losing the samples used for measurements of mechanical loss. The witness samples used for nano-indentation were often half- or quarter-disks, as other portions had been used in other measurements, like the TEM investigations seen in section 3.6.1. The silicon cantilevers are the same as those described in section 3.4, with the [100] crystalline axis perpendicular to the coated surface. The silicon samples were often the broken remains of coated cantilevers already measured for mechanical loss, as nano-indentation does not require large samples.

Film thicknesses were reported by the coating vendors to be 500 ± 2 nm in all cases except those of the hafnia samples deposited on silicon, whose reported thickness was 465 ± 5 nm, and the silica deposited on silica, which was 2 μm thick. Thicknesses were measured by ellipsometry by the coating vendors. All films were amorphous, with the exception of the hafnia samples, which were partially crystalline (see section 3.6.1).

Before measurement, samples were mounted on steel mounting disks approximately 1 cm in diameter using a cyanoacrylate adhesive, more commonly known as 'Super Glue'. Super glue is known to be a reliable and stiff method for affixing samples [149]. The metallic disks allow the samples to be mounted to the nano-indentation stage using magnetic attraction.

5.3 Experimental Method

Samples were measured using a Hysitron TI-700 Ubi with a Berkovich pyramidal tip. The tip area function and indentation machine compliance were measured and maintained at regular intervals to give correct modulus and hardness measurements on fused silica and single-crystal aluminum samples.

Table 5.1: Samples measured using nano-indentation to determine the coating Young's modulus. Heat-Treatments labelled 'AD' are 'As Deposited'. Samples are generally deposited at a temperature ≈100° C.

Coating	Substrate	Heat-Treatment [° C]
Ta_2O_5	SiO_2	300
Ta_2O_5	SiO_2	400
Ta_2O_5	SiO_2	600
Ta_2O_5	SiO_2	800
Ta_2O_5	Si	300
Ta_2O_5	Si	400
Ta_2O_5	Si	600
25% Ti:Ta_2O_5	SiO_2	AD
25% Ti:Ta_2O_5	SiO_2	300
25% Ti:Ta_2O_5	SiO_2	400
25% Ti:Ta_2O_5	SiO_2	600
55% Ti:Ta_2O_5	SiO_2	AD
55% Ti:Ta_2O_5	SiO_2	300
55% Ti:Ta_2O_5	SiO_2	400
55% Ti:Ta_2O_5	SiO_2	600
HfO_2	SiO_2	AD
HfO_2	Si	150
a-Si	Si	300
SiO_2	SiO_2	600

Table 5.2: Number of indents made at each position and the number of positions indented for each sample made during the first visit to Cambridge.

First Visit		
Sample	Indents/Position	# Positions
AD HfO_2 on SiO_2	9	1
600° 55% Ti:Ta_2O_5 on SiO_2	9	1
600° 25% Ti:Ta_2O_5 on SiO_2	9	1
600° SiO_2 on SiO_2	9	3
300° Ta_2O_5 on SiO_2	25	2
400° Ta_2O_5 on SiO_2	25	2
600° Ta_2O_5 on SiO_2	25	2
800° Ta_2O_5 on SiO_2	25	2
300° Ta_2O_5 on Si	25	2
400° Ta_2O_5 on Si	25	2
600° Ta_2O_5 on Si	25	2
800° Ta_2O_5 on Si	25	2

Indents were made using a load-controlled load-hold-unload cycle. In the loading section of the cycle, the tip is brought into contact with the sample, and the load is applied over a period of 5 seconds until it reaches the maximum applied load. The maximum load is held during the hold portion of the cycle for 10 seconds, and the load is removed over a period of 5 seconds during the unloading cycle. At any one location on a sample, a number of indentations were made, either 9 or 25, with the maximum load at each successive indent decreasing by an equivalent amount from 1000 to 100 μN, and groups of indents were made on multiple positions on the sample surface. Tables 5.2 and 5.3 give information on the number of indents and positions made for each sample over two measurement periods.

The control software for the nanoindenter performs the Oliver and Pharr analysis on the force-penetration data as the measurements are made. This is done by fitting the exponential function in equation 5.3 to the top 95% of the data from the unloading part of the cycle to get dP/dh and h_c, and using h_c in the pre-calibrated function for $A(h_c)$, the combined modulus, E^* is calculated using equation 5.1. The machine analysis returns the values of

Table 5.3: Number of indents made at each position and the number of positions indented for each sample made during the second visit to Cambridge

Second Visit		
Sample	Indents/Position	# Positions
300° Ta_2O_5 on SiO_2	25	3
400° Ta_2O_5 on SiO_2	25	3
600° Ta_2O_5 on SiO_2	25	3
800° Ta_2O_5 on SiO_2	25	3
AD 25% Ti:Ta_2O_5 on SiO_2	25	3
300° 25% Ti:Ta_2O_5 on SiO_2	25	2
400° 25% Ti:Ta_2O_5 on SiO_2	25	3
600° 25% Ti:Ta_2O_5 on SiO_2	25	6
AD 55% Ti:Ta_2O_5 on SiO_2	25	3
300° 55% Ti:Ta_2O_5 on SiO_2	25	3
400° 55% Ti:Ta_2O_5 on SiO_2	25	3
600° 55% Ti:Ta_2O_5 on SiO_2	25	3
150° HfO_2 on Si	25	2
300° a-Si on Si	25	2

h_c, $A(h_c)$, dP/dh, E^*, and the parameter values from the fit of equation 5.3. Many of these values are used in applying the Song and Pharr model.

5.4 Analysis

If one were to look only at the measured Young's modulus at each contact depth for a stiff coating applied on a compliant substrate, as in the case of the coatings on silica, the increasing effect of the substrate with increased depth would be apparent. This can be seen in figure 5.5, where the measured modulus for 300° C heat-treated un-doped tantala on a silica substrate is plotted against the contact depth for each of the 25 indents applied at one location. It is important to notice that the indent with the lowest contact depth does not fit the trend found in the other indents. This is most likely due to the failure of the calibrated area function at low contact depths. When the Song and Pharr model is applied to the data, as in figure 5.6, the low depth point (now at $I_0 \sim 1$) greatly affects the fit and pulls the film modulus towards an unlikely

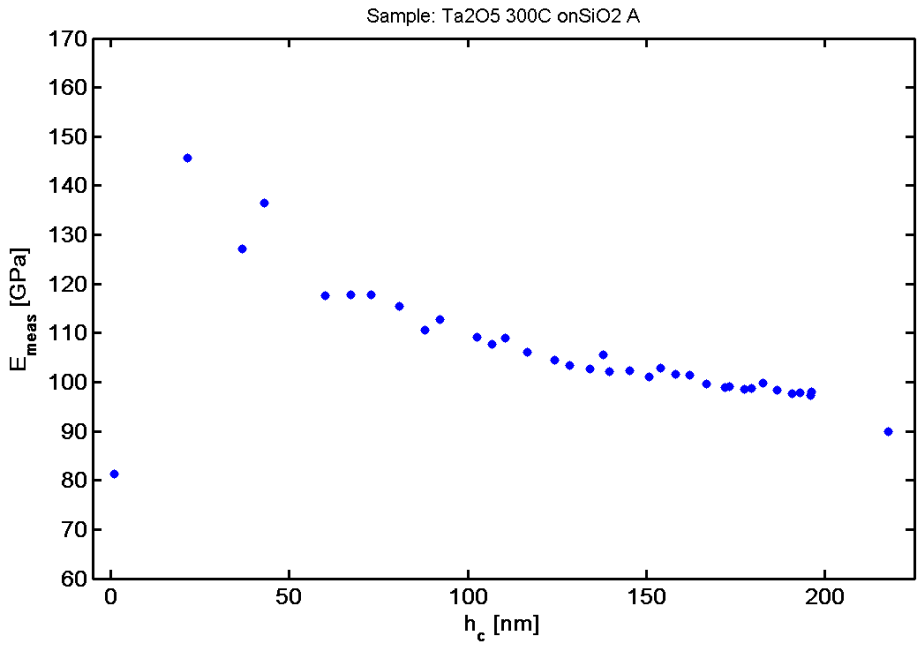

Figure 5.5: Measured Young's modulus versus contact depth for indents made at one location on 300° C heat-treated un-doped tantala on a silica substrate.

value.

In order to avoid this effect, the lowest-force indent was removed from the set of indents made at each location. This gives significant improvement to the model fits, as seen in figure 5.7, as well as the calculated film modulus and it's uncertainties. The Young's modulus of the coating is taken from value of the linear fit at $I_0 = 1$, and the modulus of the substrate is given by the inverse of the y-intercept of the fit. Uncertainties for measurements of individual locations are the one standard-deviation uncertainties in the linear fits to these data.

As there may be some uncertainty in the true thickness and Poisson's ratios of the films, the data were fit using a range of values for comparison. In fitting the model, the thicknesses of the 500 nm thick coatings were varied from 450 nm to 550 nm, and the film moduli were found to vary by less than the uncertainties in the model fit over this range, showing that the method is fairly insensitive to variation in film thickness on this scale. The Poisson's ratio of

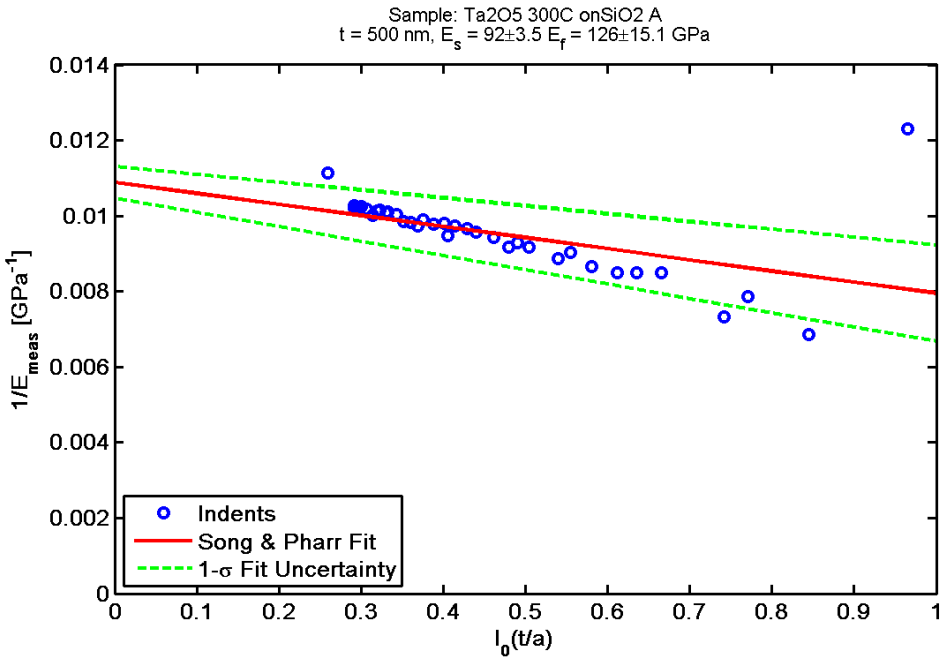

Figure 5.6: Measured Young's modulus versus the Gao $I_0(t/a)$ function calculated for all indents made at one location on 300° C heat-treated un-doped tantala on a silica substrate.

the films was initially set at 0.20 for all samples aside from the silica sample, which was set at 0.17 as the Poisson's ratio of silica films as there is evidence that they have a value close to that of bulk silica [150; 151]. Fits were made varying the Poisson's ratio over the range of 0.15 to 0.30, and the extracted Young's moduli varied by about 7% in all cases over this range, so values quoted below are calculated using a Poisson's ratio of 0.20.

Once moduli were extracted for each position on each coating, the coating modulus was calculated by taking the mean of the modulus at each position, weighted by the square inverse of its fit uncertainty, e.g. $W_i = 1/\sigma_i^2$. The uncertainty in this mean is simply the inverse of the sum of the weights, $\sigma_{\bar{X}}^2 = 1/\Sigma W_i$. This is the material modulus and uncertainty that is quoted in the Results.

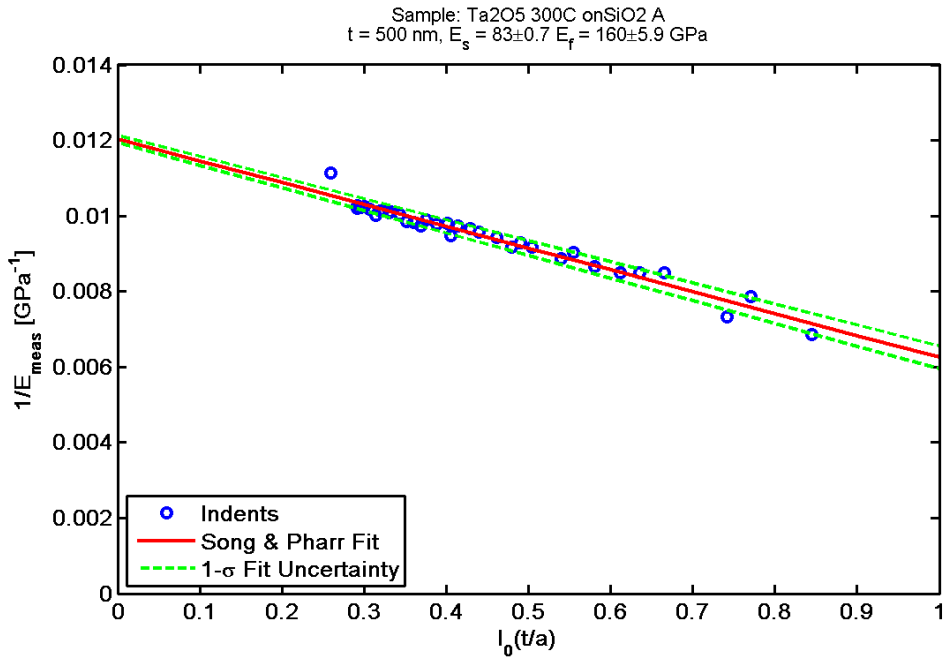

Figure 5.7: Measured Young's modulus versus the Gao $I_0(t/a)$ function calculated for all indents with the exception of the lowest-depth indent. Indents were made at one location on 300° C heat-treated un-doped tantala on a silica substrate.

5.5 Results

5.5.1 Silica

The first sample that should be discussed is the 2 μm thick coating of silica deposited on silica. This sample was deposited for two reasons; to determine the efficacy of the indentation method, and if possible, to ensure that silica deposited by ion-beam sputtering has the same Young's modulus as bulk silica. The Song and Pharr fit to the indents gives a film modulus of $E_c = 76 \pm 5.8$ GPa. This compares well with the bulk value of silica, 72 GPa [152], as well as indentation measurements of other silica coatings deposited by various techniques which give Young's moduli in the range of 70-80 GPa [153]. This value, obtained using only 9 indents in one location, gives evidence that the method can give results within 10% of the true Young's modulus of the coating. However, the coating is very thick in comparison to the other coatings studied

here, and the deepest indent was only ≈8% of the coating thickness. In the thinner samples, where indents are as much as 40% of coating thickness, the substrate effects will be more pronounced.

5.5.2 Un-doped Tantala

The extracted Young's moduli for all positions measured on the un-doped tantala samples are given in table 5.4. Measurements were made on at least two positions on each sample. The modulus for each position, as well as the weighted mean and uncertainty in the mean of all moduli from each sample are given in the table. The means are plotted in figure 5.8.

From the plot, there is a clear trend in the data for films on both substrates; as the heat-treatment increases, the Young's modulus is reduced. The 800° C heat-treated sample appears to deviate from this trend, but these samples have been shown to have undergone a crystalline transition [109]. In fact, tantala coatings are known to become polycrystalline at temperatures above 650° C [154]. Unfortunately, no information on the Young's modulus of polycrystalline tantala was found in the literature. The remaining values can be compared to existing measurements of the Young's modulus of amorphous tantala deposited by various means. One interesting comparison is with [155], which shows a similar trend in Young's modulus versus ion beam energy in dual ion beam sputtered tantala. There is evidence that increased ion energy and heat treatment invoke similar effects, increased surface motility of the deposited molecules, in increasing the density of films [154]. Microindentation measurements of similar films prepared by the same coating vendor give Young's modulus measurements of 140 ± 10 GPa [110], which agrees very well with the values presented here. Finally, Young's moduli measured by nanoindentation of ion assisted deposited, magnetron sputtered, dual ion beam sputtered, and plasma enhanced chemical vapour deposited coatings all give moduli in the region of 125-145 GPa [153].

From the data, it appears as though the moduli of coatings deposited on silicon have higher moduli than those deposited on silica. While substrates can have effects on the deposited films [154], the silicon substrates have a thin layer of thermally-grown silicon oxide on the surface, which should effectively emulate a silica surface during deposition. Instead, the lower moduli of the films deposited on silica substrates could be caused by the insensitivity of the Song and Pharr model to a stiff film on a compliant substrate [156]. As the ratio of the Young's moduli of tantala and silica appears to be ∼2, finite element models predict that the modulus extracted using the Song and Pharr model would be under-estimated by approximately 5% [156]. In comparing moduli of the 300, 400, and 600° C coatings on silica and silicon, the samples with the silica substrates are 5%. 6%, and 2% lower than their silicon substrate counterparts, respectively. This suggests that future measurements of these materials should be made on less compliant substrates, such as silicon. It should also be noted in the following sections that coatings measured on silica substrates will have reported moduli that may be lower than their true values by similar amounts.

Table 5.4: Results of indent analysis on various heat-treated samples of un-doped Ta_2O_5 on silica and silicon substrates. A Young's modulus, E_c, and its 1-σ uncertainty, σ_{E_c}, as derived from the Song and Pharr model fit for each position that was indented on the surface of the sample.

Sample	Position	E_c [GPa]	σ_{E_c} [GPa]
300° C on silica	1	153	5
	2	151	5.2
	3	159	4.8
	4	177	17.2
	5	160	7.8
	Mean:	156	2.7

Continued on next page

Table 5.4 – continued from previous page

Sample	Position	E_c [GPa]	σ_{E_c} [GPa]
300° C on silicon	1	159	20.3
	2	169	20.6
	Mean:	164	14.5
400° C on silica	1	146	2.1
	2	139	2
	3	141	3.2
	4	133	2.3
	5	146	4.3
	Mean:	140	1.1
400° C on silicon	1	155	4.4
	2	140	5.4
	Mean:	149	3.4
600° C on silica	1	134	1.9
	2	138	2.8
	3	141	3.4
	4	136	2.6
	5	135	3.2
	Mean:	136	1.2
600° C on silicon	1	150	9.4
	2	138	4.2
	Mean:	140	3.8
800° C on silica	1	180	33.5
	2	167	10.7
	3	167	10.7
	4	151	16.4

Continued on next page

Table 5.4 – continued from previous page

Sample	Position	E_c [GPa]	σ_{E_c} [GPa]
	5	191	29.7
	Mean:	166	6.6

5.5.3 25% Titania-doped Tantala

Results from indentations into 25% titania-doped tantala coatings are shown in table 5.5 and figure 5.9. Aside from the 400° C heat-treated sample, the moduli follow a similar trend to that seen in pure tantala, but with a lower modulus at 300° C heat-treatment. The 600° C heat-treated sample has a very similar modulus to that of the un-doped tantala at similar heat-treatment. The literature does not contain much information on the Young's modulus of titania-doped tantala coatings, however, the values measured here compare well to those of pure tantala listed above. Nanoindentation measurements of magnetron sputtered titania-doped films were made in [157]. The moduli measured there for tantala films doped with 17 and 40 atomic % titanium were 129 ± 7 and 137 ± 5 GPa, respectively. However, the moduli measured were similar for all doping concentrations, and the authors determined the modulus of all samples to be ∼134 GPa.

Table 5.5: Results of indent analysis on various heat-treated samples of 25% TiO_2-doped Ta_2O_5 on silica and silicon substrates. A Young's modulus, E_c, and its 1-σ uncertainty, σ_{E_c}, as derived from the Song and Pharr model fit for each position that was indented on the surface of the sample.

Sample	Position	E_c [GPa]	σ_{E_c} [GPa]
AD on Silica	1	143	3.1
	2	166	9.1
			Continued on next page

Table 5.5 – continued from previous page

Sample	Position	E_c [GPa]	σ_{E_c} [GPa]
	3	149	6.4
	Mean:	146	2.7
300° C on Silica	1	139	2.0
	2	141	3.2
	Mean:	140	1.7
400° C on Silica	1	145	5.7
	2	146	4.6
	3	163	8.5
	Mean:	148	3.3
600° C on Silica	1	134	1.5
	2	132	4.3
	3	137	4.8
	4	133	3.9
	5	137	3.8
	6	136	2.7
	7	151	18.6
	Mean:	135	1.1

5.5.4 55% Titania-doped Tantala

Results from indentations into 55% titania-doped tantala coatings are shown in table 5.6 and figure 5.10. As in the 25% titania-doped samples, if one ignores the modulus of the 400° C heat-treated sample, there is a clear trend in the modulus versus heat-treatment data. However, in this case, the modulus increases with heat-treatment. These samples are mostly titania, so it is perhaps better to compare these values to the modulus of amorphous tita-

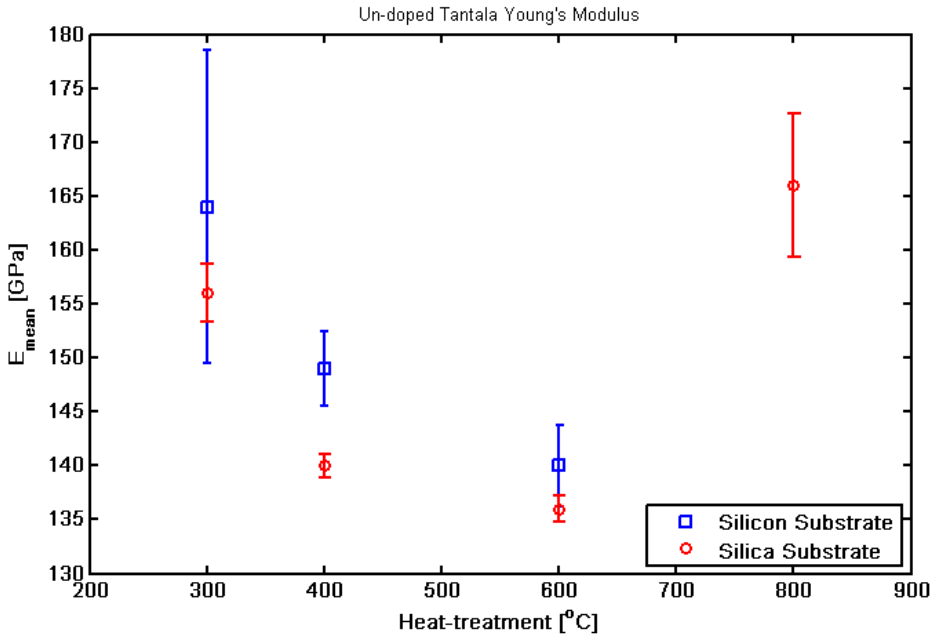

Figure 5.8: Mean Young's moduli of undoped tantala, plotted for samples of different heat-treatment.

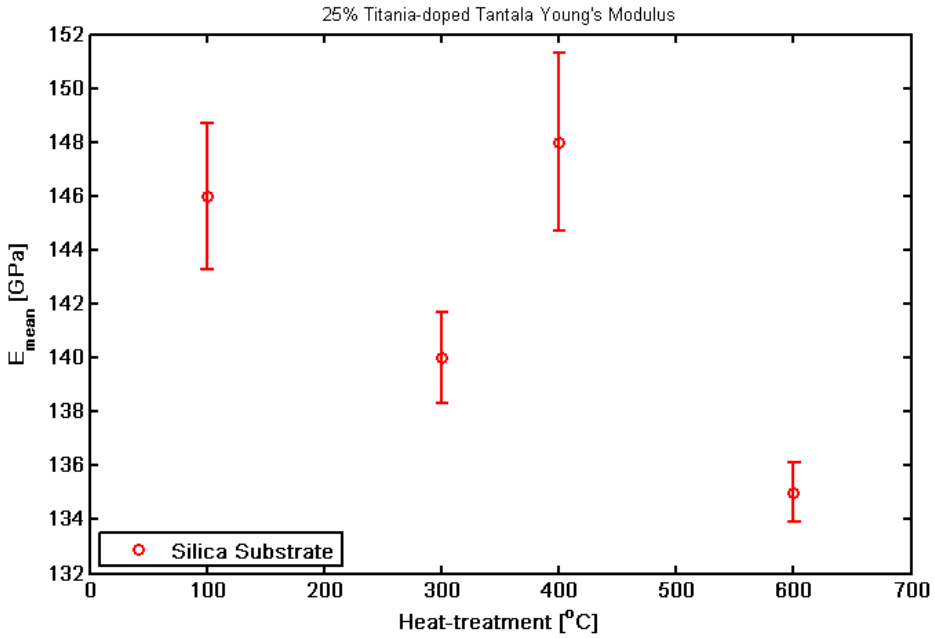

Figure 5.9: Mean Young's moduli of 25% titania-doped tantala, plotted for samples of different heat-treatment.

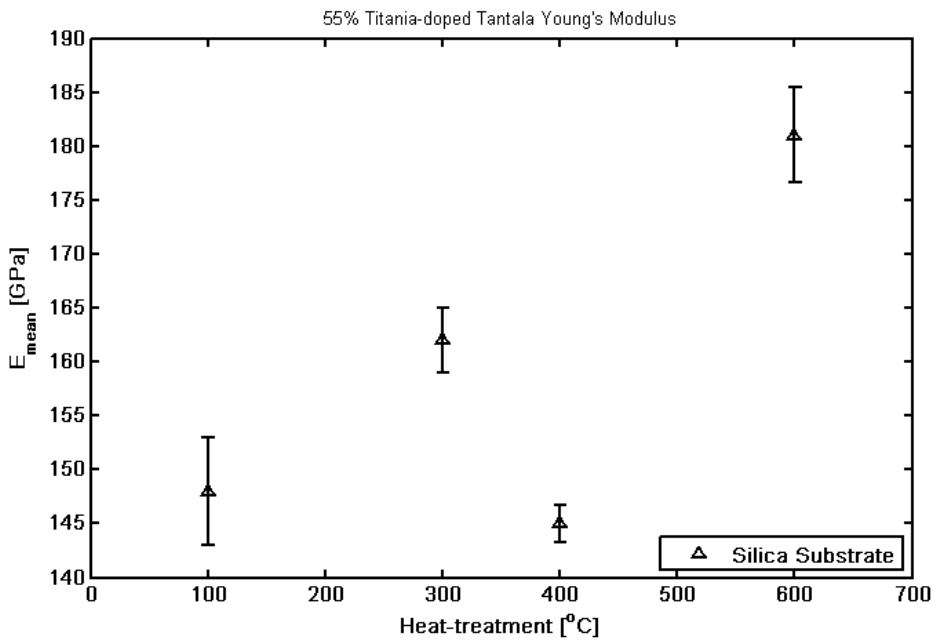

Figure 5.10: Mean Young's moduli of 55% titania-doped tantala, plotted for samples of different heat-treatment.

nia. Unfortunately, there appear to be few values for the Young's modulus of amorphous titania films in the literature. The values that do exist are not for titania deposited by ion beams sputtering, which was the deposition method for the films studied here. This appears to be due to the tendency of titania to crystallize at low temperatures [158]. Moduli for amorphous titania films deposited by a wide array of deposition techniques [158; 159; 160; 161; 153] give a wide range of moduli, generally from 120-170 GPa. The data presented here roughly agree with this range. It should be noted that many of the papers cited measured coatings that were porous and therefore would be expected to have a lower Young's modulus than that of the more dense ion beam sputtered coatings measured here, so it is not unreasonable to compare these values to those higher in the range. They can even be compared to crystalline titania, which has been measured to be as high as 290 GPa for a single crystal of rutile titania [162].

Table 5.6: Results of indent analysis on various heat-treated samples of 55% TiO_2-doped Ta_2O_5 on silica and silicon substrates. A Young's modulus, E_c, and its uncertainty from the Song and Pharr model fit, σ_{E_c} has been calculated for each poistion that was indented on the surface of the sample.

Sample	Position	E_c [GPa]	σ_{E_c} [GPa]
AD on Silica	1	147	10.4
	2	157	9.9
	3	144	7.0
	Mean:	148	5.0
300° C on Silica	1	234	31.8
	2	182	6.3
	3	155	3.5
	Mean:	162	3.0
400° C on Silica	1	140	3.4
	2	146	2.1
	3	155	6.1
	Mean:	145	1.7
600° C on Silica	1	177	7.4
	2	175	6.3
	3	204	10.8
	4	197	62.6
	Mean:	181	4.4

5.5.5 a-Si and Hafnia

Very few indents were made into the amorphous silicon and hafnia samples, so their measurements are only approximate. Two locations were measured on one sample of amorphous silicon deposited on a crystalline silicon substrate and heat-treated at 300° C. The Song and Pharr moduli for these two points

are 147±6.0 and 146±7.6 GPa, whose weighted mean gives a value of 147±4.7 GPa. This can be compared to modulus measurements of amorphous silicon and hydrogenated amorphous silicon thin films prepared by other methods, which give a range of moduli of 100-120 GPa ([163; 164; 165] and references therein). Once again, the coatings in the references were generally of a higher porosity than those measured here, and may be expected to have a lower Young's modulus.

Two hafnia samples were measured; one position was measured using only nine indents onto as-deposited hafnia on a silica substrate, and two positions were measured using 25 indents each onto 150° C heat treated hafnia on a silicon substrate. The first set of indents give a modulus of 208 ± 92 GPa, and the second set of indents give values of 219 ± 32.8 and 216 ± 19.0 GPa. If the three positions are combined to give an average value for all the Hafnia samples measured, the weighted mean would be 216±16.2 GPa. The excess scatter and uncertainty in the results may be due to the semi-crystalline structure of the coatings. Young's modulus measurements of similar coatings are uncommon, but [166] gives the Young's modulus and Poisson's ratio of bulk monoclinic hafnia as 240 GPa and 0.30, respectively, for low porosity samples. Using the same Poisson's ratio to calculate the Young's modulus from the biaxial moduli given in [167], values of 287, 182, and 214 GPa can be obtained for bulk monoclinic, reactive electron-beam evaporated monoclinic coatings, and amorphous plasma ion-assisted deposited coatings, respectively.

5.6 Conclusion

Nanoindentation measurements have been made on a number of ion beam sputtered coatings, mostly amorphous oxides, with the intention of measuring their Young's moduli. These measurements have been successfully made, and all of the values compare well with existing literature. Additionally, the tantala data show trends in Young's modulus as a function of heat-treatment.

It was found that increased heat treatment decreased Young's modulus in both un-doped and 25% titania-doped tantala, with the exception of the 800° C heat-treated un-doped tantala, which had undergone crystallization, and the 400° C heat-treated titania-doped tantala, which varied for unknown reasons. An opposite trend was found for the 55% titania-doped tantala, which exhibited increased Young's modulus with increased heat-treatment, once again, with the exception of the 400° C heat-treated sample. The variation of the 400° C heat-treated titania-doped samples is puzzling. As both samples were prepared by the same vendor as part of the same order, it is possible that these samples were heat-treated together, and there may have been a problem with the heat-treatment. Comparing the data from all titania dopings, as in figure 5.11, it can be seen that the 400° C heat-treated samples give identical Young's moduli as their non-heat-treated counterparts. Figure 5.11 plots all tantala measurements made on silica substrates for comparison.

Finally, the indent into the silica coating shows that one can expect the indentation measurements to be accurate to approximately 10%. The errorbars in the plots above are the statistical uncertainties from the fits to the Song and Pharr models, which are generally only a few percent of the measured value. It should also be kept in mind that the stiff samples measured on the silica substrates may systematically underestimate the coating moduli by $\sim$5%.

Fully understanding the effects of titania doping on the Young's modulus of tantala requires further study, as does the effects of heat treatment. Future experiments will utilize the stiffer silicon substrates and coating modulus extraction will utilize the Song and Pharr model expanded by Hay [156]. The effects of titania doping can be further studied using intermediate doping concentrations. In order to resolve discrepancies in the 400° C heat-treated titania-doped samples, they should be re-measured, and compared to new, nominally identical samples, or possibly re-heated and measured again. The Young's moduli measured here can also be analysed using effective medium

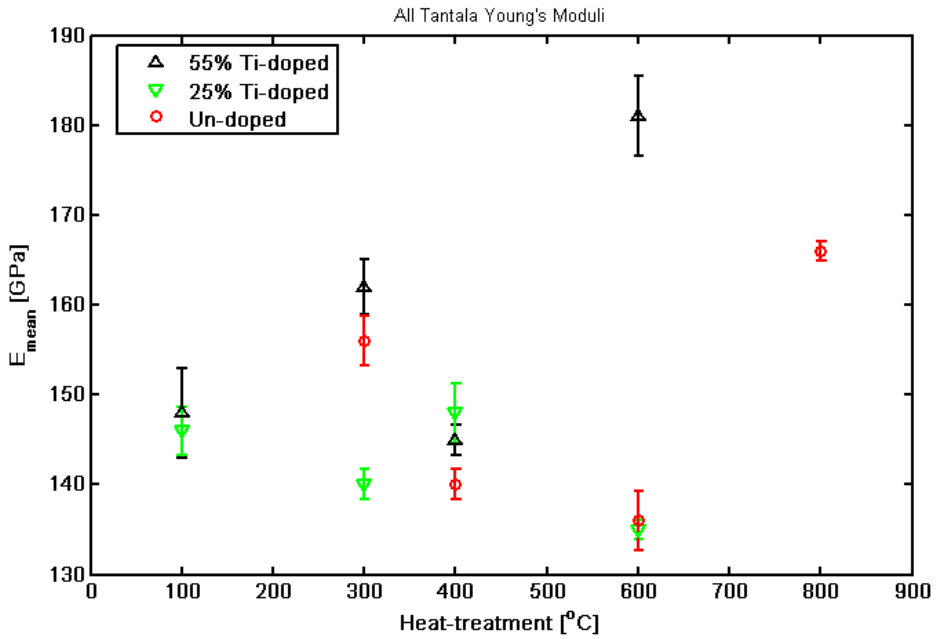

Figure 5.11: Mean Young's moduli of all tantala samples measured on silica substrates, plotted for samples of different heat-treatment. The sample heat treated at 800° C was found to be poly-crystalline, all others are amorphous.

theory [168; 169] in order to extract moduli of both tantala and titania from measured titania-doped tantala moduli.

The knowledge of these data are of value to the gravitational wave detection community in two important ways. First, in order to effectively measure the mechanical loss of a coating material, as in Chapters 3 and 4, and also in calculating the coating thermal noise in the interferometer, as in Chapter 2. Secondly, the measuring and understanding the effects of doping and heat-treatment on the Young's moduli of coating materials can lead to better understanding of the mechanisms that affect the mechanical properties of these materials–including their mechanical loss–which may lead to the prediction of optimum coatings and treatments to further reduce thermal noise in gravitational wave interferometers.

Chapter 6

Measurements of Coating Stress and Thermal Expansion Coefficient Using Stoney's Relation

It is possible to extract additional useful information about the thermo-mechanical properties of the ion beam sputtered coatings discussed in the previous chapters using the same cantilever samples. The measurement and analysis of the temperature dependence of the stress applied to the substrate by the coating, visible through the bending of the substrate, can yield information about the Young's modulus, thermal expansion coefficient, and Poisson's ratio of the coating material. Information about the stress itself can also be helpful in understanding the behaviour of the coatings in an interferometric gravitational wave detector.

This chapter presents the development of an apparatus for measuring the bending in a cantilever substrate brought about by the stress applied by a coating. The chapter begins with an introduction to the stresses that exist in the coating/substrate system, and their relation to the substrate curvature

using Stoney's relation [170] in section 6.1. The development of a simple apparatus for measuring the curvature of a cantilever is given in section 6.2. The measured samples are described in section 6.3, and the results of these measurements are presented in section 6.5. A final discussion, detailing improvements to the apparatus and the development of a finite element model for verification of the results, is given in section 6.6.

6.1 Introduction

When a coating is applied to a substrate, stress can arise due to densification of the coating after deposition and differences in coefficients of thermal expansion and epitaxy between the coating and substrate [171]. This stress applies a force on the edges of the substrate which leads to biaxial compression and bending of the substrate [172]. The stress in the coating can be determined from the radius of curvature, R, of the coated substrate using the modified Stoney's equation [170; 172]:

$$\sigma_{\text{coating}} = \frac{1}{6} B_{\text{s}} \frac{t_{\text{s}}^2}{t_{\text{c}}} \left(\frac{1}{R} - \frac{1}{R_0} \right), \tag{6.1}$$

where t_{c} and t_{s} are the thickness of the coating and substrate, respectively, R_0 is the radius of curvature of the substrate before coating, and B_{s} is the biaxial modulus of the substrate. A positive stress is defined as tensile by convention. For sufficiently flat cantilevers, R_0 can be assumed to be infinite. The biaxial modulus is defined for any material as,

$$B = \frac{Y}{1 - \nu}, \tag{6.2}$$

where Y is the Young's modulus, and ν is the Poisson's ratio of the material.

The coating stress can be considered to be composed of two components: the intrinsic stress of deposition, σ_{I}, and the thermal stress, σ_{T}, due to the

mismatch between the coefficients of thermal expansion between the coating and substrate:

$$\sigma_{\text{coating}} = \sigma_{\text{I}} + \sigma_{\text{T}}(T). \tag{6.3}$$

While the intrinsic stress of deposition is difficult to interpret and may arise from many competing mechanisms [171], the thermal stress is a simple linear function of temperature:

$$\sigma_{\text{T}} = (\alpha_{\text{s}} - \alpha_{\text{c}})B_{\text{c}}\Delta T. \tag{6.4}$$

In the above equation, α is the coefficient of thermal expansion, the subscripts c and s denote the coating and substrate, respectively; ΔT is the difference between the measurement temperature (T) and the temperature at deposition or heat-treatement (T_0), $\Delta T = T - T_0$.

Combining equations 6.3 and 6.4 the relationship between total stress and temperature,

$$\sigma_{\text{coating}} = \sigma_{\text{I}} + (\alpha_{\text{s}} - \alpha_{\text{c}})B_{\text{c}}\Delta T, \tag{6.5}$$

shows that the measurement of total stress in the coating as a function of temperature should yield a linear relationship with the y-intercept equal to the intrinsic stress in the coating, and the slope giving information on the coefficient of thermal expansion, Young's modulus, and Poisson's ratio of the coating material. The measurements of total coating stress can be made using the modified Stoney's relation given above, equation 6.1.

Combining equations 6.1 and 6.5, assuming R_0 is infinite, and solving for the temperature dependence of the radius of curvature gives,

$$R^{-1} = C\sigma_{\text{I}} + C(\alpha_{\text{s}} - \alpha_{\text{c}})B_{\text{c}}\Delta T, \tag{6.6}$$

showing the same linear dependence of R^{-1} to variations in temperature as

the stress, where C is simply a constant defined as:

$$C \equiv \frac{6t_c}{B_s t_s^2}. \tag{6.7}$$

It is therefore only necessary to measure the radius of curvature of a coated cantilever at varying temperatures in order to determine the mechanical properties and intrinsic stress of the coating.

6.2 Experiment

A simple apparatus was designed in order to measure the radius of curvature of coated cantilever samples like those used in chapters 3 and 4. In this apparatus, shown schematically in figure 6.2, a laser beam is separated into two parallel beams using a beam-splitter and 45° mirror, separated by a distance, x. These beams are reflected from the cantilever, one very near the clamped base of the cantilever, and the other from the tip. These two beams are reflected from the sample and are incident upon a screen placed a distance L from the sample.

The distance between the spots on the screen, D, will be the sum of the original separation of the beams and the deviation caused by the curvature of the cantilever: $D = x + \delta$, where D is negative if the beams cross between the sample and the screen. Therefore, if D is negative or less than x, the beams are convergent, and the sample is concave (as drawn in figure 6.1); if D is greater than x, then the beams are divergent, and the sample is convex. If the displacement of the sample tip, y is small relative to x, the radius of curvature of the sample can be calculated using the relation:

$$R = 2Lx/\delta. \tag{6.8}$$

This allows the calculation of a more direct measurement of the important physical properties by combining equations 6.6 and 6.8 to yield a relation

based upon the deflection of the beam on the screen:

$$\delta = H\sigma_{\mathrm{I}} + H(\alpha_{\mathrm{s}} - \alpha_{\mathrm{c}})B_{\mathrm{c}}\Delta T. \tag{6.9}$$

In this case, H is another constant defined as:

$$H \equiv 2LxC = \frac{12Lxt_{\mathrm{c}}}{B_{\mathrm{s}}t_{\mathrm{s}}^2}. \tag{6.10}$$

Once again, the relationship is linear and yields the intrinsic stress and mechanical properties through a simple measurement.

The setup constructed for measuring the coating stress as a function of temperature is shown in figure 6.2. In it, a laser beam is emitted from a simple hand-held laser; the beam is split into two by a beamsplitter with the first beam travelling onward to the base of the cantilever. The second beam is reflected by a mirror placed on a movable stage so that it is made parallel to the first beam but incident upon the tip of the cantilever. The cantilever was clamped within a heated and insulated box and adjusted so that the beam that reflected from the base of the cantilever was directed back towards the laser, but vertically displaced so that it fell upon a screen directly behind the laser and 5.2 metres away from the sample. The maximum horizontal deflection of the first beam was less than one degree of arc.

In order to ensure that the two beams were aligned parallel to one another, the beam separation was measured directly after the beamsplitter and directly before the sample box, a distance of $\sim$1.25 metres. Over this distance, the separation of the laser beams was adjusted to vary by less than 2 mm. In addition, when a flat mirror was placed in the position of the sample box, the reflected spots were found to deviate by less than 3mm over the total distance of approx 7.5 metres. This indicates a deviation from parallel of less than 0.03 degrees of arc.

The method of determining the radius of curvature of the sample was tested

using mirrors of known radii in place of the cantilevers. Four spherical mirrors, all with approximately 60 cm radii, were measured in the thermal bending setup as well as with a spherometer. Bending measurements taken at two different initial beam separations, $x = 1.50$ cm and $x = 3.85$ cm, gave values within ± 3 cm of the spherometer data, or 5%.

The temperature of the cantilevers was controlled using a heated box, pictured with the lid and insulation removed in figure 6.3. The box was composed of thick copper and was heated using two 12 Ω resistors. A similarly-shaped copper lid was constructed with a narrow slot to allow the passage of the laser beams. The slot was covered with a thin layer of plastic to prevent loss of air from the box without disturbing the passage of the beams. Finally, the entire box, with the exception of the laser slot, was covered with a layer of polystyrene insulation approximately 2.5 cm thick. The temperature could be controlled by adjusting the power to the resistors to be in the range of 0 to 25 W, allowing the temperature to vary from room temperature to $> 100^\circ$ C without significant sensitivity to variations in the external environment. The samples were measured in a temperature-controlled room where the ambient temperature remained at $22 \pm 2^\circ$ C.

The temperature close to the point at which the sample was held was measured using a PT-100 temperature sensor connected to a Lakeshore 340 temperature controller, which also powered the heating resistors. The temperature sensor was calibrated in liquid nitrogen, boiling water, and freezing water, and was found to be accurate to ∼0.5 K. The sample was clamped between two blocks of aluminium, and the temperature sensor was embedded in one of the blocks near the base of the sample using varnish. The sample and clamp were not in direct contact with the heating box, and heating was done primarily through contact with the air within the box.

The temperature was monitored so that no radius of curvature measurement was made until the temperature was stable to within one degree per hour.

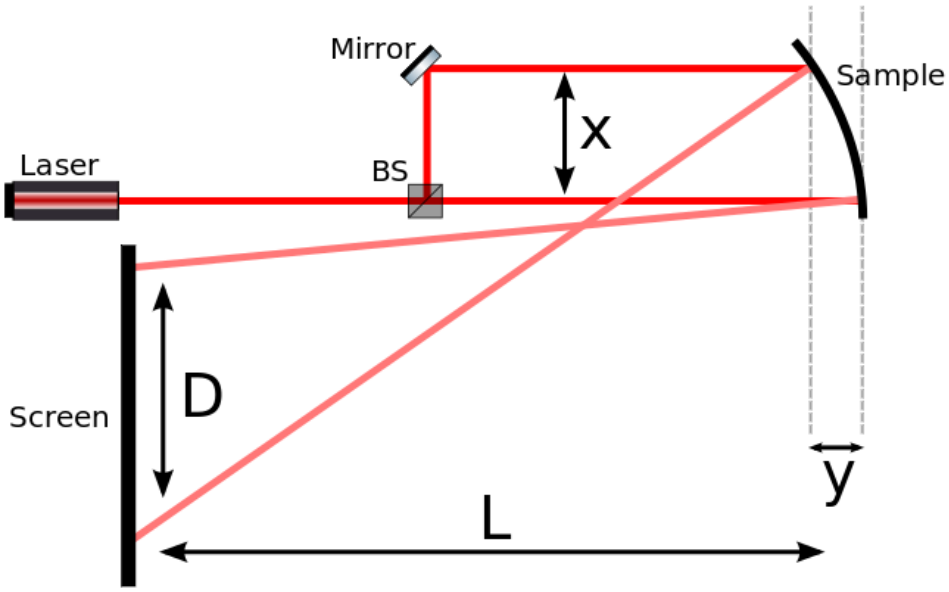

Figure 6.1: Diagram of the thermal bending experimental setup. The measurement of the spot separation, D, is dependent on the displacement of the cantilever tip, y. The Diagram is not to scale.

After a change in temperature associated with a change in the power to the heating resistors, approximately one hour would elapse before the temperature was stabilized, at which point the beam separation at the screen was measured, and the power to the resistors was again adjusted. A series of measurements made with an uncoated silicon cantilever with a temperature sensor attached to the cantilever tip showed that the sensor within the clamp gives the same value as the sensor on the cantilever tip to within one Kelvin at all heater powers.

6.3 Samples

The samples studied are of the same types as those used in chapters 3 and 4. They are composed of silicon cantilevers with a thin, ∼500 nm, amorphous coating applied to one side. The samples measured were coated with hafnia

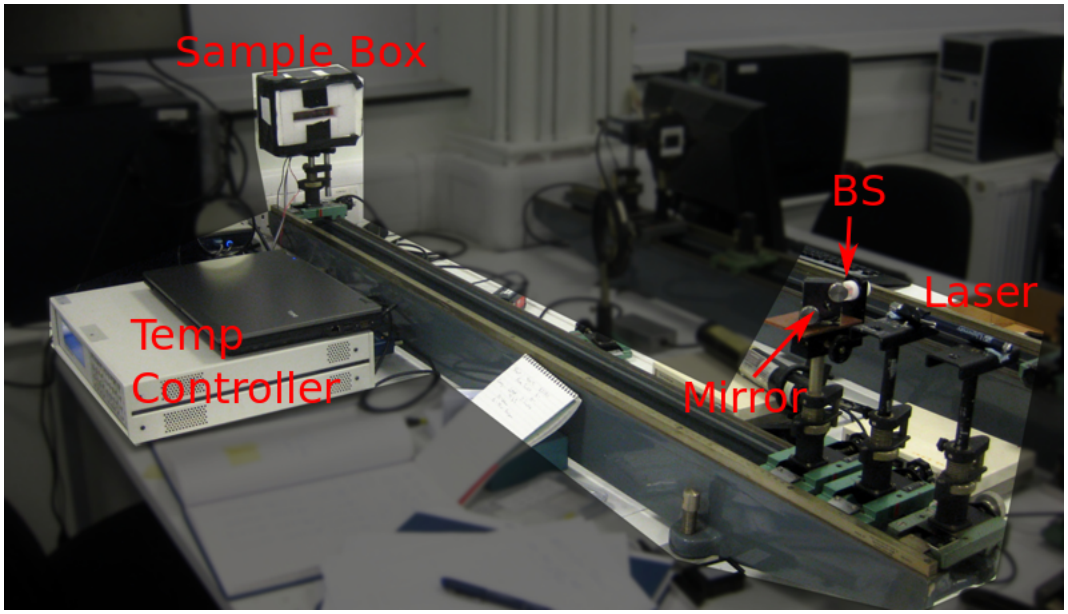

Figure 6.2: Picture of the thermal bending experimental setup with relevant components highlighted. The screen is located behind and above the laser and is not visible on this picture. The screen/sample separation is ∼5 metres.

(HfO_2), or with 25 or 55% titania-doped tantala (Ti:Ta_2O_5), as listed in table 6.1. The table also lists the values unique to each sample, and sample numbers are the same as those in their relevant mechanical loss measurements from the above chapters. Substrate thickness was measured using the optical profiler discussed in Appendix A. The mean and standard deviation of the cantilever profiles are given in the table and used as the substrate thickness in the analysis. The coating thicknesses were given by the supplier, CSIRO [117] with the exception of samples 7-2 and 7-8, whose coatings were deposited on the opposite side of the cantilever. The process for calculating the thickness of these coatings is discussed for sample 4-2 in section 4.2. The Young's modulus, Y_c, of the coatings was found through nanoindentation, as discussed in chapter 5.

The biaxial modulus, B_c, of each coating was calculated using equation 6.2 and a Poisson's ratio of $\nu = 0.25 \pm 0.05$. While the Poisson's ratios of the coating materials are not well known, the value was chosen to match that of similar materials. The Poisson's ratio of similar dual ion-beam sputtered

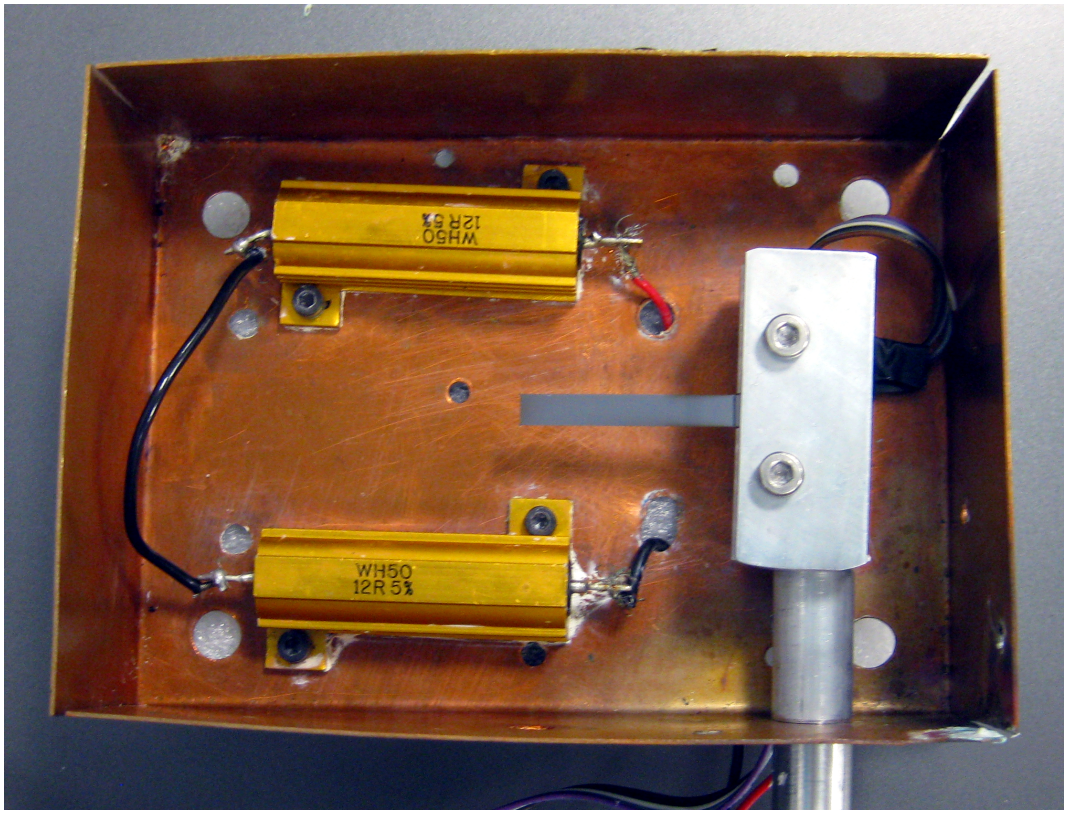

Figure 6.3: Picture of the inside of the sample holder box. The copper box is heated using two resistive heaters. The temperature sensor is mounted through the back of the clamp near the base of the sample.

Table 6.1: Samples measured in the thermal bending apparatus.

Sample	Label	t_s [μm]	t_c [nm]	Y_c [Gpa]	B_c [Gpa]
HfO_2 AD	SN8	114±2	465±2	216±16	281±23
HfO_2 150° C	SN3	124±5	465±2	216±16	281±23
HfO_2 200° C	SN6	121±4	465±2	216±16	281±23
HfO_2 400° C	SN1	121±6	465±2	216±16	281±23
Uncoated 400° C	SN9	100±1	–	–	–
55% Ti:Ta_2O_5 AD	4-1	66±6	500±10	148±5	192±10
55% Ti:Ta_2O_5 300° C	4-3	66±7	500±10	162±3	210±9
55% Ti:Ta_2O_5 400° C	4-5	65±7	500±10	145±2	188±8
55% Ti:Ta_2O_5 600° C	4-7	63±6	500±10	181±4	235±11
25% Ti:Ta_2O_5 AD	7-1	75±5	500±10	146±3	190±8
25% Ti:Ta_2O_5 AD	7-2	57±2	480±10	146±3	190±8
25% Ti:Ta_2O_5 300° C	7-3	74±7	500±10	140±2	182±7
25% Ti:Ta_2O_5 400° C	7-5	74±8	500±10	148±3	192±9
25% Ti:Ta_2O_5 600° C	7-8	73±6	480±10	135±1	175±7

Table 6.2: Values used for all samples measured in the thermal bending apparatus.

Parameter	Value	Reference
B_s [100]	180.3 ± 0.3 GPa	[112]
α_s [110]	$2.59 \pm 0.05 \times 10^{-6}$ K^{-1}	[112]
ν_c	0.25 ± 0.05	see text

tantala given in [155] is 0.27. The Poisson's ratio of a similar coating material, Nb_2O_5, is given in the same reference as 0.20-0.23. This can also be compared to the Poisson's ratio of bulk silica, 0.17 [152]. The Poisson's ratio of bulk monoclinic hafnia is estimated to be ≈0.30 [166]. Values for bulk samples of polycrystalline tantala tend to be in the region of 0.23 [129]. In general, it can be said that the Poisson's ratio of amorphous metal oxides fall within the region of 0.2-0.3. Additional values that are similar for all samples are given in table 6.2.

The uncoated cantilever from the Hafnia loss measurements, SN9, was also measured in order to test the assumption that the initial curvature of the samples is negligible. This sample was uncoated but had the thermal oxide that

all samples possessed (∼30 nm), as well as a thin coating of silicon nitride (∼8 nm) on the top surface (see discussion in section 3.4) possessed by all the hafnia-coated samples. If there was a non-negligible curvature, or if the curvature changed significantly during heating, the analysis would need adjustment. The uncoated sample was found to have a radius of curvature of >79 meters with no variation due to temperature changes. This can be compared to measurements of other samples, which had radii in the range of 2-10 meters. If one assumes all cantilevers had this initial curvature, it would effect the stress measurements by reducing the measured stress by ∼2 MPa; this is a negligible correction.

6.4 Analysis

The measurement of the samples involves heating the sample to a stable temperature and then noting the separation of the beam spots of the screen. A line is then fit to the separations plotted against the temperature. The slope of the fit line contains information about the coefficient of thermal expansion of the coating material, and the y-intercept of the fit line gives information about the intrinsic stress in the material. An example of this can be seen in figure 6.4.

The fit line in figure 6.4 is described by equation 6.9. Taking the slope of the line, it is simple to calculate the product $(\alpha_s - \alpha_c)B_c$. In the absence of any knowledge of the biaxial modulus of the coatings, to proceed further would require the use addition samples having the same coating applied to substrates of a different material [173]. In the case where such samples are not available, as in this study, the combined values can be plotted as in figure 6.5, where the blue line represents the allowed values of B_c and α_c given the slope of the fit line. However, if the Young's modulus of the coatings is known, e.g., from the measurements in chapter 5; and one knows or assumes a Poisson's ratio, as

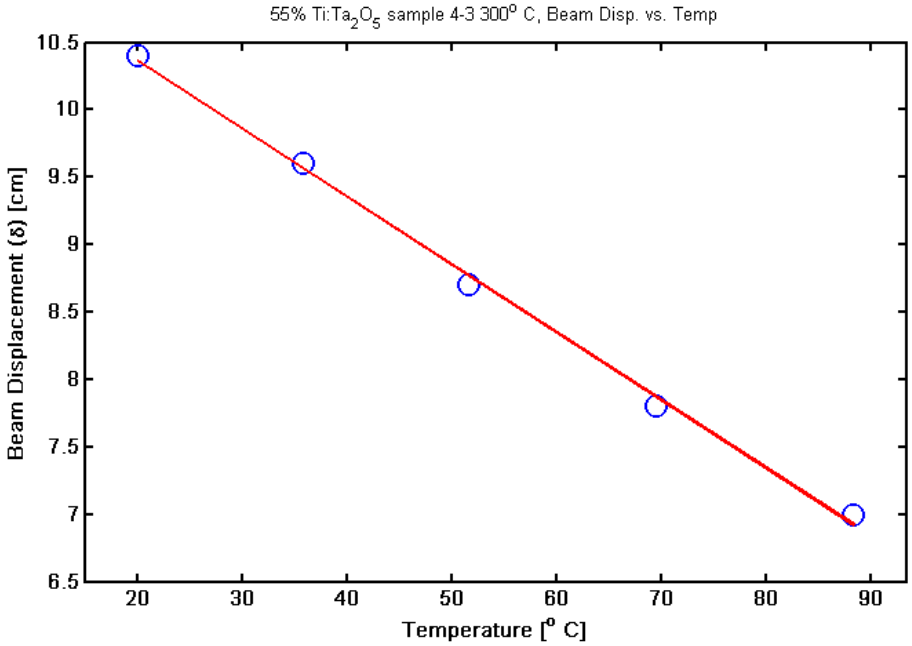

Figure 6.4: Typical plot of beam displacement (δ) versus temperature. Uncertainties in beam displacement are generally on the order of 0.5 cm, but are dependent on the size of the reflected beam spots.

discussed above; the coefficient of thermal expansion for the coating material can be extracted, as shown in figure 6.5.

It is also possible to calculate the stress in the sample at each temperature to yield the relation in equation 6.5. The intrinsic stress in the coating can be calculated equivalently from a fit to this relation, as in figure 6.6, or directly from equation 6.9. These stress calculations have much larger uncertainties which are dominated by the systematic uncertainty in the thicknesses of the coating and substrate. It is apparent from the deviation from the straight line in the figure that the statistical uncertainties are much lower. These relations allow the calculation of the room temperature stress, as well as the intrinsic stress in the coating, calculated as the value of the stress in the coating at its heat-treatment temperature.

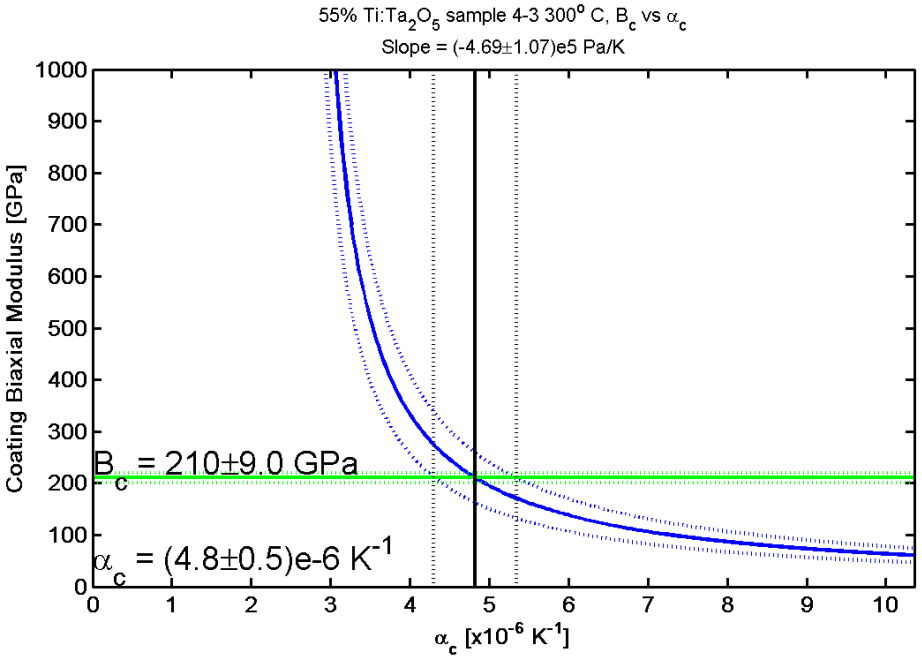

Figure 6.5: Plot of the allowed values of B_c and α_c given the fit line from figure 6.4 (blue line). The biaxial modulus from table 6.1 (green line), allows the extraction of a value for the coefficient of thermal expansion (black line).

6.5 Results and Discussion

There are two types of result that can be drawn from the above analysis: a measurement of the thermal expansion coefficient of the coating material, and a measurement of the intrinsic stress in the coatings. The former is derived from the slope of the δ-ΔT relationship, and this slope is fairly insensitive to the various uncertainties in the measurements. It is however, affected by uncertainties in the Young's modulus and Poisson's ratio of the coating material. The intrinsic stress in the coatings is far more uncertain, and the results discussed below are largely qualitative. Finally, it can be noted that there was no hysteresis found between the heating and cooling cycles of any measurement, indicating that the low ($\sim$100° C) maximum temperature did not effect the material properties of any of the samples.

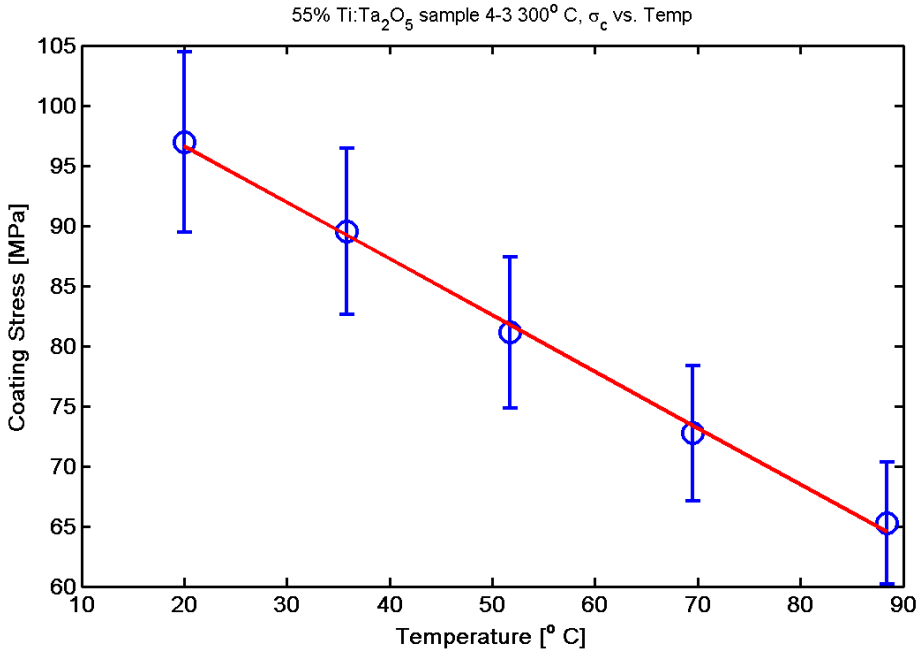

Figure 6.6: Plot of tensile stress versus temperature with accompanying fitted line. The uncertainties shown here contain all but the systematic uncertainty in substrate thickness, which may alter the stresses by as much as 20%. However, even this uncertainty is contained within the errors of figure 6.5. The fit line is equivalent to that seen in figure 6.4.

6.5.1 Coefficient of Thermal Expansion

The coefficients of thermal expansion for the coatings are given in table 6.3 and are plotted in figures 6.9, 6.7, and 6.8. The uncertainties in the figure for the moduli come from the statistical uncertainty from the fit of the δ-T relation (figure 6.4) and the systematic uncertainty in the physical properties of the samples.

The values for Young's modulus of the coatings are taken from the nanoindentation measurements of the coating materials on silica, discussed in chapter 5. As discussed in that chapter, the moduli measured for coatings applied to silica substrates may be under-estimated by ∼5%. If the Young's moduli are increased by 5% in the calculation of the coefficients of thermal expansion, the resulting coefficients are decreased by <3%.

The Poisson's ratio of the coating material is a parameter that is poorly known. The ratios have not been well measured, but are assumed to be in the range of $0.2 \leq \nu_c \leq 0.3$. Decreasing the Poisson's ratio of the coating material to 0.2 from 0.25 results in an increase in the calculated coefficient of thermal expansion of as much as 5%. Increasing the Poisson's ratio to 0.3 has the opposite effect.

The thickness of the substrates carries some uncertainty, and this will have some effect on the calculated coefficients of thermal expansion. From the optical profiler measurements of the samples, as discussed in section 3.4, the substrate thickness varies by more than 10% over the length of some samples. For the calculations here, the mean thickness of the substrates was used in calculations of the coating coefficients of thermal expansion and stress. However, it is useful to note that if the thickness used in the calculations is varied by 10%, there is a similar variance of 10% in the calculated coefficient of thermal expansion.

Table 6.3: Coefficients of thermal expansion derived from thermal bending measurements.

Hafnia	
Sample	α_c [$\times 10^{-6}$ K^{-1}]
SN1	5.9±0.6
SN3	6.1±0.7
SN6	6.9±0.7
SN8	8.4±1.2
55% Titania-doped Tantala	
Sample	α_c [$\times 10^{-6}$ K^{-1}]
4-1	5.1±0.5
4-3	4.8±0.5
4-5	5.2±0.6
4-7	4.7±0.5
25% Titania-doped Tantala	
Sample	α_c [$\times 10^{-6}$ K^{-1}]
7-1	3.9±0.4
7-2	4.0±0.2
7-3	3.6±0.3
7-5	4.3±0.5
7-8	4.0±0.3

6.5.1.1 Titania-doped Tantala

The coefficients of thermal expansion for both of the titania doping concentrations, shown in figures 6.7 and 6.8, appear to give similar results. The plots suggest that there is no obvious trend in the coefficient of thermal expansion of the coatings with heat-treatment temperature. Also plotted as red lines are the weighted means of the coefficients. For the 55% titania-doped tantala, the mean coefficient of thermal expansion is $(4.9 \pm 0.3) \times 10^{-6}\mathrm{K}^{-1}$, and for the 25% titania-doped samples, the mean is $(3.9 \pm 0.1) \times 10^{-6}\mathrm{K}^{-1}$. These values can be compared to the reported coefficient of thermal expansion of pure tantala coatings deposited by dual ion-beam sputtering in [155], which gives a value of $4.4 \times 10^{-6}\mathrm{K}^{-1}$. Measurements of the coefficient of thermal expansion of bulk tantala give values of $6.7 \times 10^{-6}\mathrm{K}^{-1}$ for sintered bars [160], and $3.0 \times 10^{-6}\mathrm{K}^{-1}$ for chemically vapour deposited β-Ta_2O_5 [174], and $2.06 \times 10^{-6}\mathrm{K}^{-1}$ and $2.45 \times 10^{-6}\mathrm{K}^{-1}$ for α- and β-Ta_2O_5 respectively [129]. The values measured here are of similar or moderately greater values than those in the literature, which may be due to the effects of the titania dopant.

Doping tantala with other materials, such as niobia and alumina, appears to have significant effects on the coefficient of thermal expansion [175], however, there are no measurements of this effect from titania. There also appears to be little information in the literature on the coefficient of thermal expansion of amorphous titania coatings. Measurements of bulk polycrystalline samples give a value of $8.2 \times 10^{-6}\mathrm{K}^{-1}$ [176]. Similar values for the thermal expansion parallel to the principal axis are measured in [177] for rutile and anatase titania, giving values of 7.8 and $9.0 \times 10^{-6}\mathrm{K}^{-1}$, respectively. However, the same paper measures the thermal expansion perpendicular to the principal axis of anatase material as only $3.8 \times 10^{-6}\mathrm{K}^{-1}$. Additionally, the coefficient of thermal expansion of the rutile material has been measured to be $8.19 \times 10^{-6}\mathrm{K}^{-1}$ in [178]. From these numbers it is apparent that titania has a much higher coefficient of thermal expansion than tantala, consistent with the finding that

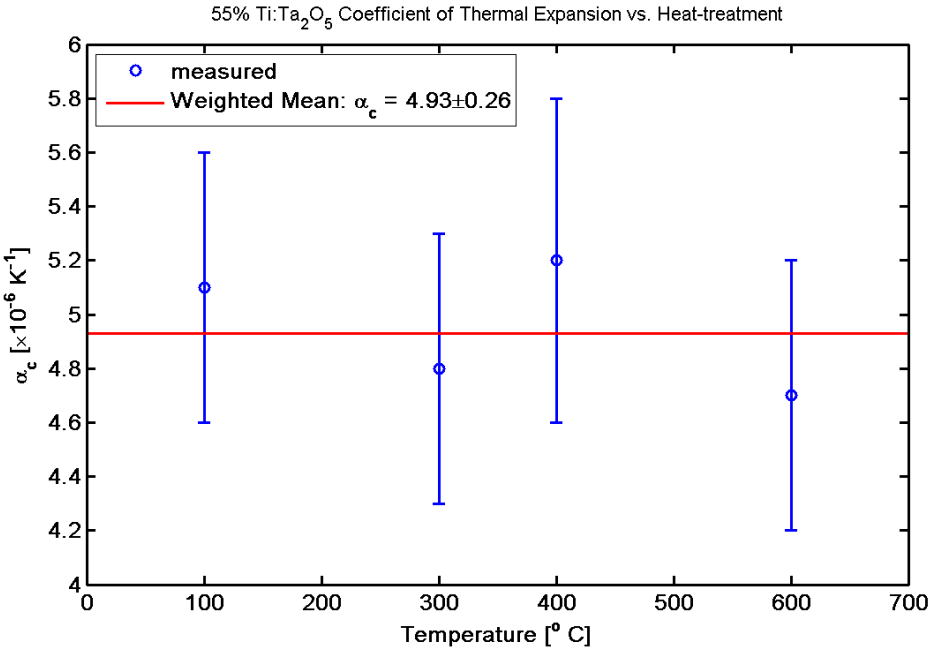

Figure 6.7: Plot of measured coefficient of thermal expansion for 55% titania-doped tantala coatings versus heat-treatment temperatures. The 'As-Deposited' coating is considered heat-treated at 100° C, the substrate temperature during deposition.

the 55% titania-doped tantala has a higher thermal expansion than the 25% titania-doped tantala.

6.5.1.2 Hafnia

The calculated coefficients of thermal expansion for the hafnia coatings are plotted against heat-treatment temperature in figure 6.9. From the points, it is apparent that there is a trend of increasing coefficient of thermal expansion with increased heat-treatment. The weighted least-squares fit is plotted against the measured values in the figure. The linear fit gives a relation of $\alpha_c = (5.0 \pm 0.2) + (0.009 \pm 0.001) \times T$, where α_c is measured in 10^{-6} K^{-1} and T is measured in Celsius degrees.

As discussed in section 3.6.1, the hafnia coatings appear to be partially crystalline, so it is possible that the increasing coefficient of thermal expansion may be evidence of increasing crystallisation. However, it was not obvious from

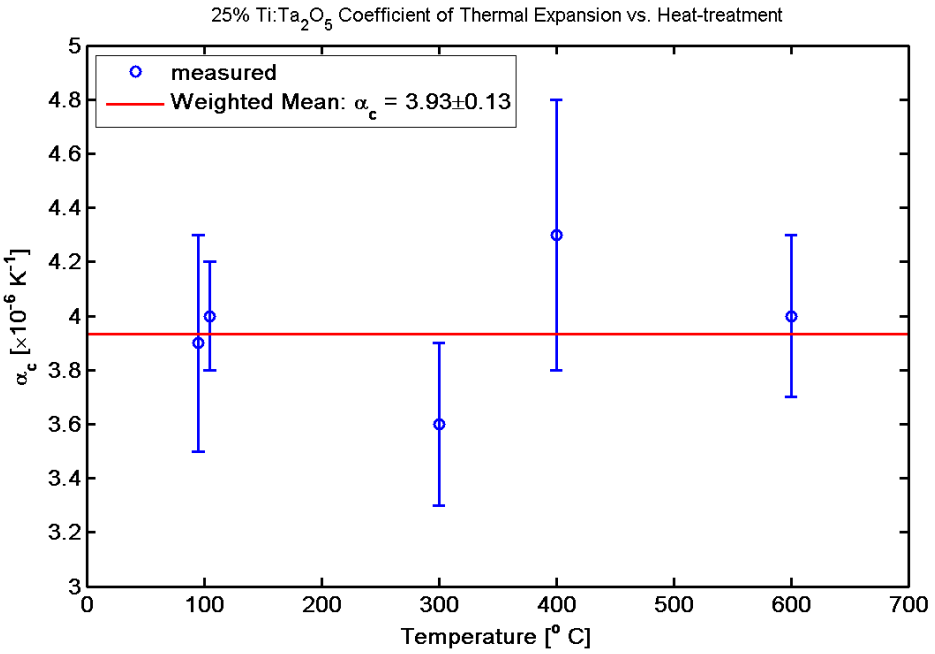

Figure 6.8: Plot of measured coefficient of thermal expansion for 25% titania-doped tantala coatings versus heat-treatment temperatures. The 'As-Deposited' coating is considered heat-treated at 100° C, the substrate temperature during deposition. The two 'As Deposited' values are offset from each other for clarity.

TEM images of the samples, seen in figure 3.22, that those samples treated at higher temperatures had such increases in crystallisation.

In the calculation of the coefficients of thermal expansion for the hafnia coatings, a constant value for the Young's modulus was used. It is also possible that the trend in coefficient of thermal expansion is due to a hidden decrease in Young's modulus. Such a trend was seen in the nanoindentation data for the pure tantala coatings in chapter 5, but there was not enough data to find a similar trend in hafnia. Instead, the modulus used was the mean of indents taken from two different samples.

The values measured here can be compared to values measured for bulk monoclinic hafnia samples, as very few other measurements of the thermal expansion coefficient of hafnia have been made. The coefficient of thermal expansion of these materials is found to be $6.12 \times 10^{-6}\mathrm{K}^{-1}$ in [179] and $5.8 \times 10^{-6}\mathrm{K}^{-1}$ in [180]. These measurements were both made of cylindrical bars of pressed and sintered hafnia. The sintering temperatures were all greater than 1400° C. There are no studies comparing the effects of such low heat-treatments on thin films of hafnia. However, the two values found in the literature are comparable to those measured for the low-temperature heat-treated samples.

6.5.2 Intrinsic Stress

Using the line fits to the calculated stress versus temperature points, it is possible to extract some useful information regarding the intrinsic stress in the coatings. As mentioned above, these results have larger errors due to the systematic uncertainties in the film and substrate thicknesses, especially the thickness of the substrate, as the calculated stress has an inverse-squared dependence on this value, and our substrates were found to have variable thicknesses, as discussed in Appendix A. A change in the thickness of the substrates used in the calculations by 10% leads to a change in the measured stress by 20%.

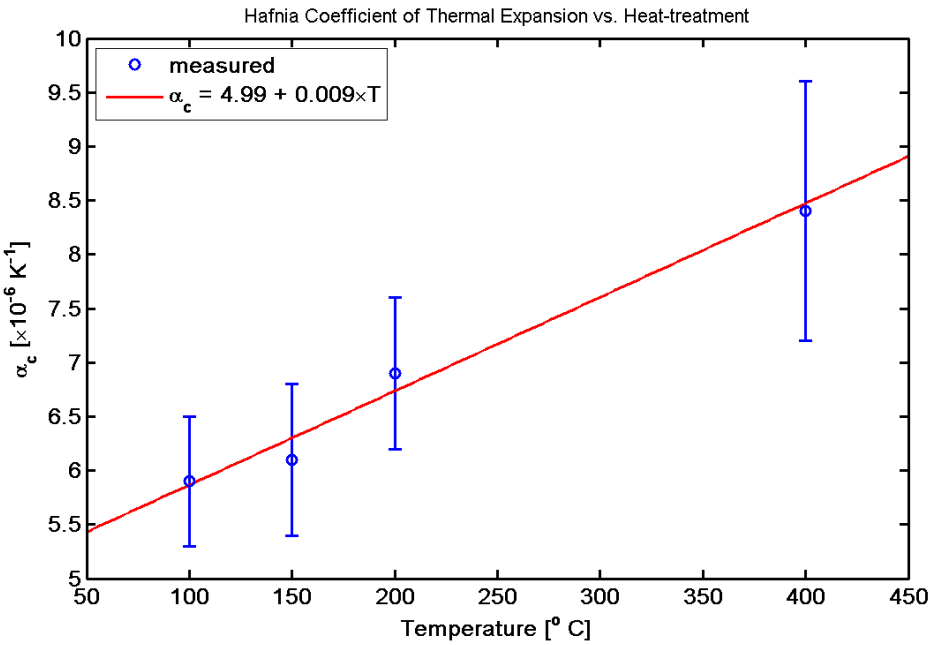

Figure 6.9: Plot of measured coefficient of thermal expansion for hafnia coatings versus heat-treatment temperatures. The 'As-Deposited' coating is considered heat-treated at 100° C, the substrate temperature during deposition.

With the above uncertainties kept firmly in mind, it is interesting to calculate the temperature at which the coatings would be stress free. This is done by taking the fit to the stress/temperature data, as in figure 6.6, and extrapolating the trend to zero stress. The results of this calculation can be seen in table 6.4.

There do not appear to be any clear trends among the hafnia samples. The unphysical temperatures indicate that the stress in the hafnia coatings is dominated by the intrinsic stress in the coatings. If the stress/temperature trend is extrapolated to the temperature of heat-treatment, it is compressive and approximately 1100, 1300, 1600, and 400 MPa for the AD, 150, 200, and 400° C heat-treatments, respectively. This indicates a trend of increasing compressive stress with heat-treatment until the 400° C treatment, which appears to greatly reduce the stress.

The zero-stress temperatures for the 55% titania-doped tantala samples

Table 6.4: Temperatures at which the coatings are stress-free, extrapolated from the measured stress/temperature relationships.

Hafnia		
Sample	Heat-Treatment [°C]	Zero Stress Temp. [°C]
SN8	AD	-541±101
SN3	150	-1096±202
SN6	200	-1059±143
SN1	400	-11±9
55% Ti-doped Ta_2O_5		
Sample	Heat-Treatment [°C]	Zero Stress Temp. [°C]
4-1	AD	-215±54
4-3	300	226±40
4-5	400	553±118
4-7	600	740±151
25% Ti-doped Ta_2O_5		
Sample	Heat-Treatment [°C]	Zero Stress Temp. [°C]
7-1	AD	-381±106
7-2	AD	-663±96
7-3	300	250±67
7-5	400	538±145
7-8	600	235±42

give the most interesting trend. The As-Deposited sample has a negative temperature, which demonstrates that it is dominated by a compressive intrinsic stress. The other samples all have zero stress temperatures very near their heat-treatment temperatures. In fact, the relationship between the heat-treatment temperature and the zero-stress temperature for these three samples has a slope of 1.3±0.5, where a slope of 1 would indicate that they are equivalent. This supports the assumption that the heat-treatment relieves the intrinsic stress in the coating [119]. It is interesting to note that the stress is released even at the lower 300° C heat-treatment.

A similar trend can be seen in the 25% titania-doped tantala samples. The As-Deposited samples are again under compressive stress and dominated by the intrinsic stress. The 300 and 400° C coatings both have zero-stress temperatures that include their heat-treatment temperatures; however, the 600° C heat-treated sample varies greatly. It is believed that samples 7-2 and 7-8 are especially poor samples, due to their uncertain deposition on the 'top' side of the cantilever (see discussion in section 4.2). Due to the uncertainty in the thickness and uniformity of the coatings, it is difficult to ensure that the coatings meet the assumptions necessary for Stoney's equation to be valid, and the results for these samples must therefore be regarded with considerable caution.

6.6 Additional Work

After the completion of the above measurements, it was decided that an improved apparatus and better understanding of the bending mechanism would be useful. To that end, the apparatus was rebuilt, and work was begun on modelling a coated cantilever using the ANSYS finite element analysis software.

Table 6.5: Measured coefficients of thermal expansion from the original thermal bending experiment, α_A, and from the new apparatus, α_B.

Sample	α_A [$\times 10^{-6}$ K^{-1}]	α_B [$\times 10^{-6}$ K^{-1}]
SN1	5.9±0.6	6.4±0.6
SN3	6.1±0.7	6.6±0.6
SN6	6.9±0.7	6.0±0.6
4-3	4.8±0.5	4.3±0.4
4-5	5.2±0.6	5.0±0.6
7-5	4.3±0.5	3.9±0.3

6.6.1 New Apparatus

The new apparatus was built with special attention to automating the data-taking procedure. This included the addition of a digital camera to image the laser spots on the screen, and software written in LabView to control both the camera and the temperature of the sample. The apparatus was rebuilt using a higher-powered laser to increase the visibility of the laser spots on the screen, which is now positioned 6 metres from the sample. The automation software allows for smaller temperature steps due to the reduced need for operator interaction. After the temperature has stabilized, as discussed in section 6.2, the digital camera records an image of the laser spots along with a calibration ruler on the screen. The separation of the beams can then be extracted using any image-processing software.

The new apparatus has been used to re-measure some of the samples discussed above. The results are shown in table 6.5. The results agree with those measured using the previous setup to within the quoted uncertainties, showing the reproducibility of the results. However, it is interesting to note that the trend in the hafnia results, discussed in section 6.5.1.2, is not clear from the new results. This is most likely due to a sparsity of data, and a solid conclusion remains to be found. The new apparatus is now being used to measure new samples.

6.6.2 Modelling

In order to understand the effects of having a substrate with variable thickness on the coefficient of thermal expansion measured above, and any effects due to the deviation of a perfect cantilever, e.g., the clamping block, a finite element model of a coated cantilever was constructed using the ANSYS Workbench software. The model is constructed from 2-D plane elements which allow large deformations and strains, required for displacement >10% of the body thickness. The cantilever was modelled having substrate dimensions of 34 mm long and 50 μm thick with a clamping block on one end measuring 10mm long and 0.5 mm thick and the entire substrate is composed of crystalline silicon with Young's modulus of 166 GPa, Poisson's ratio of 0.28, and coefficient of thermal expansion of 2.6×10^{-6} K^{-1}. The coating is modelled as a surface 34 mm long and 500 nm thick, attached to the bottom edge of the cantilever. The coating is given the mechanical properties of an ideal 'tantala' with Young's modulus of 140 GPa, Poisson's ratio of 0.23, and coefficient of thermal expansion of 4.3×10^{-6} K^{-1}. The model is set so that at 0° C, the coating has no stress. The top surface of the clamping block is held fixed. A sketch of the cantilever model is shown in figure 6.10.

Using the above values and equations 6.1 and 6.4, a temperature change of $\Delta T = 80°$ C would give a thermal stress of $\sigma_{\mathrm{T}} = -24.7$ MPa, which would cause the radius of curvature of the coated cantilever to be $R = -7.77$ meters, which would cause the free end of the cantilever to be deflected vertically by -74.4 μm. Where the negative sign indicates that the stress is compressive and the cantilever is bent away from the coated side.

The characteristic size of the mesh elements for the coating and substrate could be independently adjusted, and their values were found to have an impact on the curvature and stress in the model. A search for the optimal parameter combination was carried out using a grid search of the parameter space of 10 to 50 μm for the substrate element size in steps of 10 μm, and 1 to 10 μm for

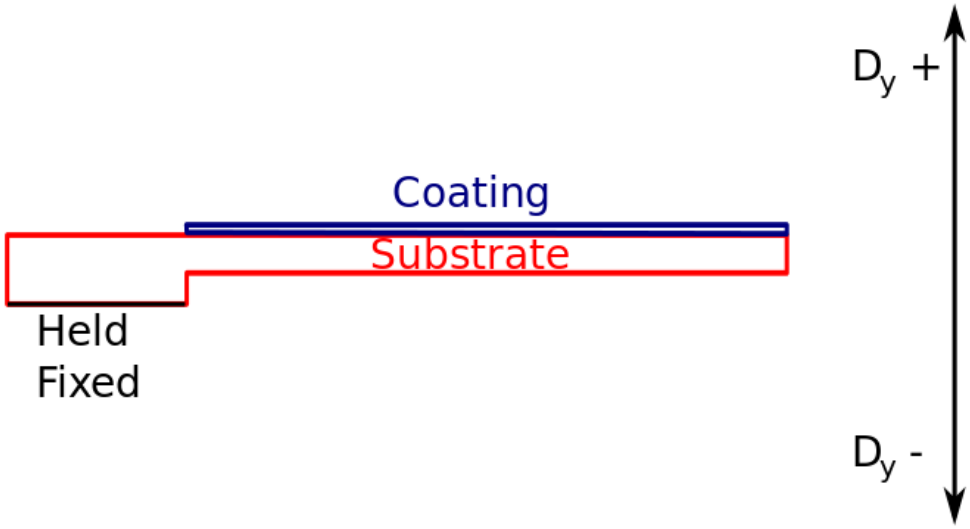

Figure 6.10: Schematic of the model used in the ANSYS software. This drawing is not to scale.

the coating element size in steps of 1 μm.

The optimal parameter combination was decided by minimizing the difference between the model and analytically calculated cantilever deflection and radius of curvature. Using this method, it was found that a substrate element size of 20 μm and a coating element size of 9 μm gives the best agreement with the radius of curvature. A comparison of the expected and model values is given in table 6.6. The radius of curvature measurements were made by extracting the vertical displacement of each node location along the coating's long edge and fitting a circle to the displacement and node location data. The vertical displacement of the free end of the cantilever is simply the vertical displacement of the node on the coating corner farthest from the clamping block. The stress in the coating was measured using the normal stress tool in ANSYS and probed at a location near the centre of the coating, far from the clamping block and free end. However, the stress was constant throughout the

Table 6.6: Radius of curvature (R), coating stress (σ_{T}), and deflection of the cantilever free end (D_{y}) calculated using Stoney's equation (Theory) and the ANSYS model.

	Theory	Model
R [m]	-7.77	-7.78
σ_{T} [MPa]	-24.7	-18.4
D_{y} [μm]	-74.4	-80.5

coating material with the exception of the ends of the coating, as expected for a 2-D model of a homogeneous coating deposited on a substrate [171].

That the vertical displacement does not match the fit radius may indicate that the model is not actually circular in shape, however, the R^2 goodness of fit value for the radius of curvature fits are generally around 1.0005, indicating that a circle is an excellent descriptor of the cantilever shape. In calculating the expected value of the vertical offset from the theory, it is assumed that the centre of the cantilever lies directly above or below the point where the cantilever contacts the clamping block, displaced vertically by the radius of curvature. In the circular fit to the model data, however, the best fit has a small, $\sim$2 mm, horizontal offset on the centre of the circle, indicating that the cantilever is rotated in the model. This is most likely due to the stress acting upon the stationary clamping block. Once this is accounted for, the vertical offset of the cantilever end matches the theory to $\pm$0.5%. However, making this correction still requires the full displacement data for fitting the centre coordinates. Future model analysis will have to take the tilt of the cantilever into account.

The stress calculated by the model does not match the theory for one simple reason: the model is two-dimensional, while the theory predicts biaxial bending. The biaxial bending effectively increases the stiffness of the cantilever and produces greater stress. In fact, if the Young's moduli of the coating and substrate are replaced by their biaxial moduli in the model, the calculated film stress agrees with the expected values to $\pm$2%. This change in the model

results in the wrong values for radius of curvature and vertical deflection of the tip. This can be eliminated by building a 3-D model that allows for biaxial bending of the cantilever; however, early tests of this method showed that it requires much smaller mesh sizes and is too computationally expensive for current development.

A more detailed test of the model involves the thermal evolution of the coating/substrate system to see if it responds to additional heat in the same way as predicted by theory. One can plot the expected radius of curvature versus ΔT to see how well they agree. The radius can be modelled at various temperatures and compared to those expected from theory. This comparison is made in figure 6.11. In the plot, the radii of curvature, R, are plotted as $1/R$ to show the linear relationship. These plots show that the full radius of curvature calculated from the model agrees with the expected value to better than 1%.

The agreement between the model radius of curvature and vertical displacement with the predictions made by the theory indicate that the model in its current form can be used to make more sophisticated predictions. Further work on this front may include additional analysis to correct the vertical displacement values, as these are most relevant to the experimental measurements. Once this is completed, the model will be used to test the effects of non-uniform substrate thickness and other areas of uncertainty discovered in the experimental measurements.

6.7 Conclusions

The thermal bending technique uses Stoney's equation to measure the stress in a thin coating deposited on a thicker substrate by measuring the radius of curvature of the coated substrate. The stress is measured at a number of different temperatures in order to determine the biaxial modulus and coefficient of thermal expansion of the coating. An apparatus has been built to measure

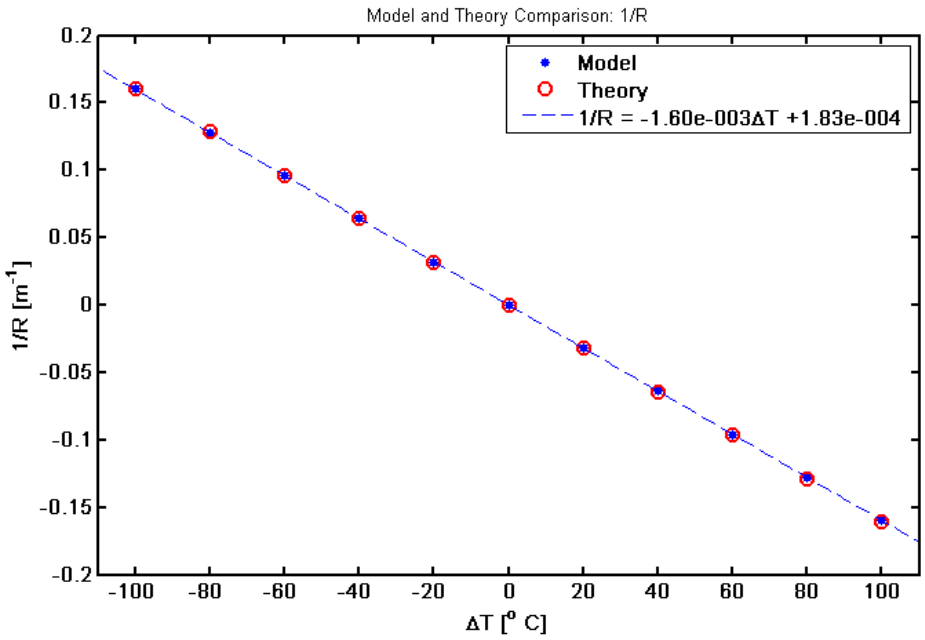

Figure 6.11: Comparison between the modelled and expected (Theory) values of the radius of curvature of the cantilever. The dashed line shows the linear fit to the model values.

the radius of curvature of coated cantilevers at various temperatures between ∼20 and ∼100° C. Measurements have been made on silicon substrates coated with hafnia and 25 and 55% titania-doped tantala heat-treated to various temperatures. The radius of curvature measurements have been combined with the Young's modulus of the coatings measured in chapter 5 in order to extract the coefficients of thermal expansion of the coating materials.

The coefficients of thermal expansion measured for the hafnia coatings with no heat-treatment and 150, 200, and 400° C heat-treatment are not inconsistent with literature values for bulk monoclinic hafnia. The data may also show a positive correlation between heat-treatment and coefficient of thermal expansion, although this is not clear. The coefficients of thermal expansion measured for the titania-doped tantala do not show a similar correlation. Their values are in the same broad range as those found in the literature for similar, but undoped, coatings. Analysis of the stress in the coatings indicates that the stress

in titania-doped tantala coatings is greatly relieved with heat-treatments as low as 300° C. These initial results demonstrate that the simple apparatus can be used to gather valuable information regarding the mechanical and thermal properties of thin coatings using the same cantilevers used in other mechanical property experiments, such as those in previous chapters.

The apparatus has been rebuilt and made more autonomous. Initial measurements from the new apparatus show that it gives comparable results to those of the original. It is currently employed in measurements of more coatings. A modelling process has also been started in order to remove some of the uncertainty associated with the cantilever dimensions. The model was constructed using ANSYS finite element modelling software, and has shown to reproduce the expected curvature in the substrate. Future efforts will improve this model and use it to refine the experimental results.

Chapter 7

Conclusions

Long baseline gravitational interferometers are promising tools for directly detecting gravitational waves from astronomical sources. A network of first-generation interferometric gravitational wave detectors have already been developed and carried out several data-taking runs. While no direct detections were made by these first-generation detectors, their data were used to place new constraints on astrophysical models of gravitational wave sources. Second-generation detectors are currently being commissioned. They utilize numerous improvements that increase their sensitivity by a factor of ten. It is widely expected that these second-generation detectors will make the first direct detection of gravitational waves.

The improvements that have made second-generation interferometric detectors more sensitive have brought to light more fundamental noise sources, such as the thermal noise of the optical coatings used in the mirrors. Improvements in these coatings have already brought sensitivity gains over those used in first-generation detectors; however, third generation detectors will still be limited by coating Brownian noise, especially at their most sensitive frequency bands. Furthermore, future detector designs will seek to reduce Brownian noise by cooling the mirrors to cryogenic temperatures. It is therefore necessary to investigate new optical coating materials and seek to understand the source

of this noise in existing coatings by measuring the mechanical properties that contribute to coating Brownian noise at cryogenic temperatures.

One of the most important material properties that impact the Brownian noise in interferometric gravitational wave detectors is the mechanical loss of the optical coatings. Previous research has shown that the mechanical loss of the high index of refraction component, ion-beam-sputtered (IBS) tantalum pentoxide (Ta_2O_5, or tantala), is the dominating contributor to the coating mechanical loss. A similar high index material, hafnium dioxide (HfO_2, or hafnia), has been investigated as a possible replacement for the tantala. While the room temperature mechanical loss of the hafnia is higher than the tantala, the mechanical loss is lower below $\sim$100 K. Furthermore, it was discovered through transmission electron microscopy measurements that the hafnia coatings were partially crystalline, an effect that has been known to increase loss and degrade optical properties in similar materials. Preventing the crystallisation of the hafnia through the use of dopants such as silicon dioxide is suggested as a follow-up experiment that may yield still lower mechanical loss and better optical properties.

Doping of tantala with titanium dioxide (TiO_2, or titania) at 25 cation % has been shown elsewhere to reduce the mechanical loss of the material by as much as 40%; however, the mechanism for this reduction is still poorly understood. Another treatment that has been shown to effect mechanical loss of tantala is the heat-treatment of the sample after deposition. An investigation of the mechanical loss of tantala coatings doped at 25 and 55 % titania has been performed before the samples have been heat-treated in order to better understand the effects of doping without the added effects of heat-treatment. A further comparison was made between samples with different substrate surface preparations. These investigations indicate that the mechanical loss is dominated by the intrinsic coating mechanical loss independent of whether the substrate surface was polished or etched. At cryogenic temperatures, both

doped samples had losses comparable with 300° C heat-treated un-doped tantala pentoxide.

Other mechanical properties of the coatings are important, both in measuring the mechanical loss, and in calculating thermal noise in the interferometers. Knowing these properties can also aid in understanding the origin of mechanical loss in the coatings by comparison with model predictions. The Young's modulus of IBS tantala has been measured as a function of heat-treatment in undoped, 25%, and 55% titania doped samples using nano-indentation. The Young's modulus of un-doped tantalum dioxide is reduced with increasing heat-treatment until the sample crystallizes between 600 and 800° C. The 25% doped samples exhibit similar trends, while the 55% doped samples have the opposite trend. Additional measurements have given Young's moduli of IBS hafnia and amorphous silicon coatings.

The coefficient of thermal expansion has also been measured for the hafnia and doped tantala coatings. The measurements also allowed an analysis of the stress conditions in the coatings as a function of post-deposition heat-treatment. The coefficient of thermal expansion for the 25 and 55% tantalum dioxide doped coatings did not vary with heat-treatment; however, it did appear to vary for the hafnia coatings. Stress analysis indicates that the as-deposited doped tantala coatings and all of the hafnia coatings have a compressive intrinsic stress. In the tantala coatings, the stress was relieved and with heat-treatment as low as 300° C.

Knowing the mechanical properties will greatly aid in the understanding of thermal noise in interferometers, and the selection of better materials for use in interferometric gravitational wave detectors. Furthermore, the techniques for measuring these properties have been developed and demonstrated, allowing future measurements on other materials. The measurements made here are also applicable outside the field of gravitational wave detection, as these are commonly used optical materials whose mechanical properties are becoming

more important as the field of precision interferometry continues to advance.

Appendix A

Cantilever Thickness Measurements Using the Optical Profiler

The thickness of the cantilevers used in chapters 3, 4, and 6 can be measured directly using an optical profiler, described in [181]. This device, originally designed to image silica fibres for the suspension of the mirrors used in interferometric gravitational wave detectors, uses a 6.15 high-linear-magnification camera to image the object, backlit by a diffuse light source. The 640 $\times$ 480 pixel camera has an image resolution of 1.6 μm per pixel, and the camera resolution is calibrated using a 1 mm $\pm$ 0.12 μm slip gauge.

In measuring a cantilever, the sample is aligned edge-on to the camera. The profiler allows for focusing on the near edge of the cantilever, and the sample can be rotated so that the sample is precisely edge-on to the camera. Repeated measurements of the same sample with re-adjusted camera-sample angles and focus give average values that vary by ± 2 μm, indicating that the measurements are fairly robust against minor variations in these parameters. The profiler works by imaging a small section of the cantilever edge at a time, the software detects the edges of the cantilever along every row of pixels, and

calculates the distance of each edge from the nearest side of the image. The camera is then moved less than a field of view along the cantilever and another image is taken. The edges from each image are aligned along the overlap, giving a continuous dataset of edge locations with each position having multiple measurements.

A.1 Analysis of Profile Data

The profiler control software returns positions of the two edges of the cantilever, measured as distances from a straight line at some arbitrary distance. It also subtracts these two values to give a thickness for the cantilever measured at all points along the length scanned by the profiler. These data, however, are fairly noisy due to the scatter from the multiple overlapping measurements, as well as dust on the surface of the cantilever, and occasional errors in the edge finding algorithm due to focus or lighting conditions. Therefore, the cantilever thickness was calculated by first down-sampling the position information for the cantilever edges, smoothing them using a weighted local regression algorithm to remove spurious points, and then taking the difference to give a smoothed thickness profile.

An example of the position data taken by the profiler is given in figure A.1. This figure shows the raw data as returned from the profiler. The first step in the analysis is to remove any points on the ends of the cantilever that include the clamping block or the free end. The figure does not show the clamping block, however, the free end is shown by the sharp drop in cantilever edge location on the right side of the plot. This is caused by the edge-finding algorithm locating the edge at the side of the image when there is no edge to locate.

Once the ends of the cantilever are removed, the data are down-sampled. Typical cantilever scans contain more than 40,000 points along each edge, making a direct smoothing process unnecessarily long. The data are down-

sampled to contain only ∼1000 points by choosing every N/1000th point from each data set. Examples of the results from this down-sampling can be seen in figures A.2, A.3, and A.4, where the original data are shown as blue points, and the down-sampled data are shown in red.

The down-sampled data are then smoothed using the MATLAB 'rloess' smoothing algorithm. This algorithm is a local regression using weighted linear least squares and a second degree polynomial model, it assigns zero weight to data outside six mean absolute deviations. The examples of the smoothing results can be seen in figures A.2, A.3, and A.4 as the thick black line.

The thickness along the cantilever, an example of which is shown in figure A.4, is calculated by subtracting the down-sampled and smoothed profiles of the two sides. Figure A.4 shows the thickness of the cantilever if the raw data were simply subtracted (blue points), if the down-sampled data were subtracted (red points), and the difference of the smoothed points (black line). The greater variation seen in the blue and red points is an effect of the pixel resolution of the camera, as each horizontal 'line' of points is separated from the ones above and below it by 1.6 μm. This represents a variation of ∼1 pixel in the edge-finding algorithm on repeated measurements of the same point.

It is interesting to study the edge profiles in figures A.2 and A.3, to compare the two sides of the cantilevers. The cantilevers are fabricated by etching from one side of a silicon wafer that has been polished on both sides [182]. This leaves one side 'etched' with the clamping block protruding, and the other side remains 'polished' and flat. The coatings are usually applied to the polished side. For the figures mentioned above, the edge profiles are constructed by subtracting a least-squares fit line from the edge positions returned by the profiler. This removes the slope, and gives the variation of the points around some central value. It is obvious from these figures that, at least for the hafnia SN9 cantilever, most of the variation in the thickness comes from variation on the etched side. In fact, this appears to be the case in all the profiled

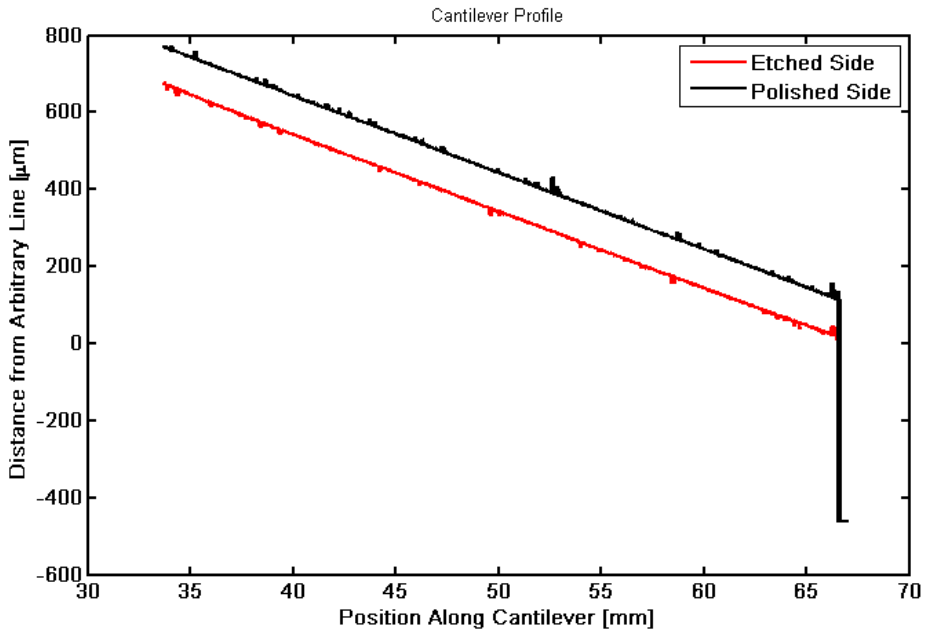

Figure A.1: Profiler scan of the hafnia SN9 cantilever. Position along the cantilever is measured from an arbitrary position. The vertical axis is the distance from an arbitrary straight line to the edge of the cantilever. In this figure, the clamping block would be located on the left side of the plot, and the end of the cantilever is represented by the sharp edge on the right side of the plot.

cantilevers.

A.2 Profiler Results

The results from the profiler measurements can be seen in table A.1. This table shows the mean thickness of each sample, the standard deviation of the thickness measurements, and the maximum variation along the cantilever. All values are calculated from the smoothed, down-sampled thickness calculations. The mean thickness was calculated by averaging all thickness measurements made along the length of each cantilever. The standard deviation is the standard deviation of these points. The maximum variation is calculated by subtracting the smallest thickness from the largest. Together, these can give a rough estimate of the thickness and uncertainty of the cantilevers. It is inter-

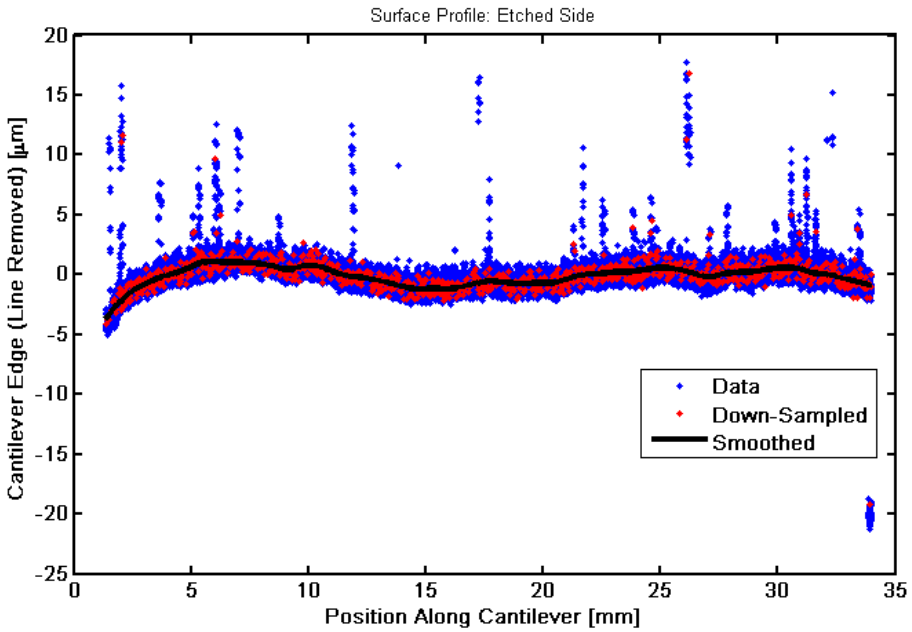

Figure A.2: Profile of the etched surface of the hafnia SN9 cantilever with fit line subtracted. This shows the variation of the cantilever's etched surface around its mean position with any slope removed. Negative values are towards the centre of the cantilever.

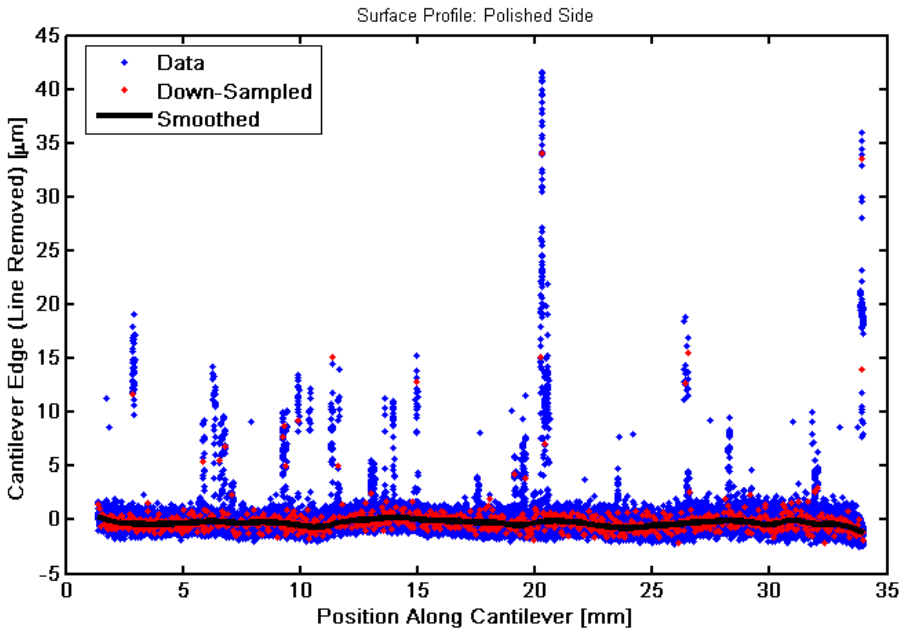

Figure A.3: Profile of the polished surface of the hafnia SN9 cantilever with fit line subtracted. This shows the variation of the cantilever's etched surface around its mean position with any slope removed. Negative values are towards the centre of the cantilever.

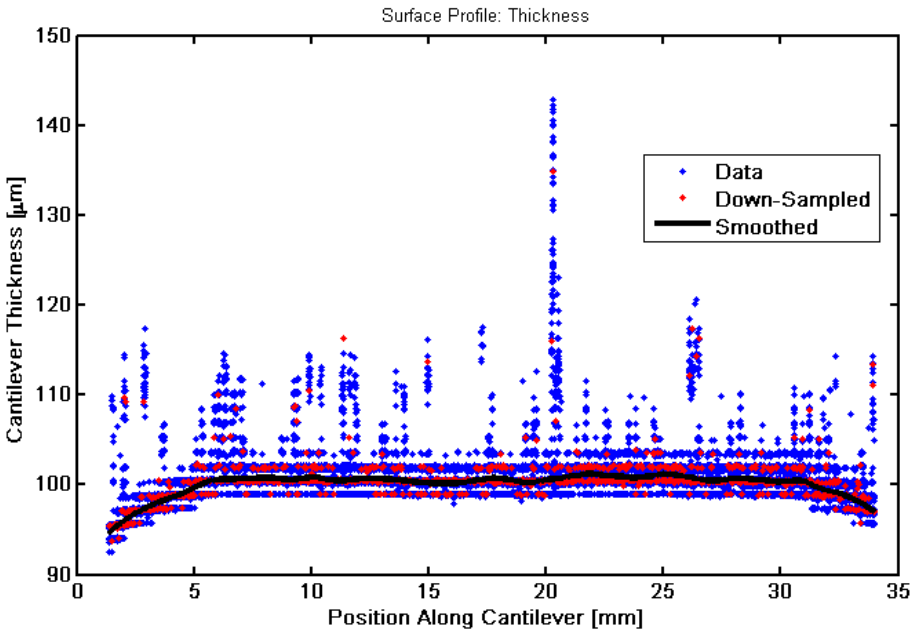

Figure A.4: Thickness of the hafnia SN9 cantilever calculated by subtracting the positions of the two cantilever edges.

esting to note that the average maximum variation for the hafnia cantilever set (labelled SN#) is 20 μm, while the average maximum variation for the titania-doped tantala cantilever set (labelled #-#) is 21 μm. Such a similarity is surprising because there is a factor of two difference in the thickness of these two sets of cantilevers. One would expect the increased time taken to etch the thinner cantilevers would result in greater variation.

Table A.1: Mean thickness, standard deviation, and maximum variation for all samples measured using the profiler.

Sample	Mean Thickness [μm]	Std [μm]	Max Variation [μm]
SN1	121	6	32
SN2	126	4	21
SN3	123	5	23
SN4	120	5	31
SN5	124	3	20
SN6	121	3	16
SN7	122	3	18
SN8	113	2	18
SN9	100	1	6
SN10	118	4	23
SN11	121	6	28
SN12	126	2	7
4-1	65	5	21
4-2	53	2	13
4-3	66	6	23
4-5	65	6	23
4-7	62	5	19
4-9	56	4	15
7-1	74	6	25
7-2	57	2	9
7-3	73	7	29
7-5	76	7	29
7-7	71	5	21

Bibliography

[1] A Einstein. Die Grundlage der allgemein Relativitatstheorie. *Annalen der Physik*, 49:769, 1916.

[2] PR Saulson. *Fundamentals of Interferometric Gravitational Wave Detectors*. World Scientific, Singapore, 1994.

[3] J Weber. Detection and generation of gravitational waves. *Physical Review*, 117:306–313, 1960.

[4] RL Garwin and JL Levine. Single gravity-wave detector results contrasted with previous coincident detections. *Physical Review Letters*, 31:176–180, 1979.

[5] A Abramovici, WE Althouse, RWP Drever, Y Gürsel, et al. LIGO: The Laser Interferometer Gravitational-Wave Observatory. *Science*, 256(5055):325–333, 1992.

[6] F Acernese et al. The status of VIRGO. *Classical and Quantum Gravity*, 23:S63–S69, 2006.

[7] H Lück et al. Status of the GEO detector. *Classical and Quantum Gravity*, 23:S71–S78, 2006.

[8] B Willke et al. The GEO-HF project. *Classical and Quantum Gravity*, 23:S207, 2006.

[9] K Kuroda et al. Japanese large-scale interferometers. *Classical and Quantum Gravity*, 19:1237, 2002.

[10] M Punturo et al. The Einstein Telescope: a third-generation gravitational wave observatory. *Classical and Quantum Gravity*, 27(19):194002, 2010.

[11] K Kuroda and the LCGT Collaboration. Status of LCGT. *Classical and Quantum Gravity*, 27(8):084004, 2010.

[12] KAGRA. Kagra website. `http://gwcenter.icrr.u-tokyo.ac.jp/en/`, August 2012.

[13] B Kocsis and A Loeb. Brightening of an accretion disk due to viscous dissipation of gravitational waves during the coalescence of supermassive black holes. *Physical Review Letters*, 101:041101, 2008.

[14] JH Taylor, RA Hulse, LA Fowler, GE Gullahron, and JM Rankin. Further observations of the binary pulsar PSR 1913 + 16. *The Astrophysical Journal*, 206:L53–L58, 1976.

[15] CM Will. The confrontation between general relativity and experiment. *Living Reviews in Relativity*, 9(3), 2006.

[16] RP Feynman, FB Morinigo, WG Wagner, and B Hatfield. *Feynman Lectures on Gravitation*. Westview, Boulder, CO, 2003.

[17] I Martin. *Studies of materials for use in future interferometric gravitational wave detectors*. PhD thesis, University of Glasgow, 2009.

[18] BS Sathyaprakash and BF Schutz. Physics, astrophysics and cosmology with gravitational waves. *Living Reviews in Relativity*, 12(2), 2009.

[19] BF Schutz. Determining the Hubble constant from gravitational wave observations. *Nature*, 323(6086):310–311, 1986.

[20] A Buonanno, GB Cook, and F Pretorius. Inspiral, merger, and ring-down of equal-mass black-hole binaries. *Physical Review D*, 75:124018, 2007.

[21] BJ Owen and BS Sathyaprakash. Matched filtering of gravitational waves from inspiraling compact binaries: Computational cost and template placement. *Physical Review D*, 60:022002, 1999.

[22] H Dimmelmeier, CD Ott, H-T Janka, A Harek, and E Müller. Generic Gravitational-Wave Signals from the Collapse of Rotating Stellar Cores. *Physical Review Letters*, 98:251101, 2007.

[23] E Müller. Gravitational waves from Core Collapse Supernovae. In J.-A. Marek and J.-P. Lasota, editors, *Proceedings of the Les Houches School of Physics, held in Les Houches, Haute Savoie, 26 September - 6 October, 1995*, pages 273–308, Cambridge, 1997. Cambridge Contemporary Astrophysics, Cambridge University Press.

[24] M Punturo, M Abernathy, F Acernese, B Allen, et al. The third generation of gravitational wave observatories and their science reach. *Classical and Quantum Gravity*, 27(8):084007, 2010.

[25] L Lindblom, BJ Owen, and G Ushomirsky. Effect of a neutron-star crust on the r-mode instability. *Physical Review D*, 62(8):084030, 2000.

[26] Y Wu, CD Matzner, and P Arras. R-Modes in Neutron Stars with Crusts: Turbulent Saturation, Spin-down, and Crust Melting. *The Astrophysical Journal*, 549:1011–1020, 2001.

[27] C Cutler. Gravitational waves from neutron stars with large toroidal B fields. *Physical Review D*, 66(8):084025–+, 2002.

[28] L Bildsten. Gravitational radiation and rotation of accreting neutron stars. *The Astrophysical Journal Letters*, 501:L89–L93, 1998.

[29] BF Schutz. Gravitational wave astronomy. *Classical and Quantum Gravity*, 16(12A):A131–A156, 1999.

[30] C Van Den Broeck. The gravitational wave sepctrum of non-axisymmetric, freely precessing neutron stars. *Classical and Quantum Gravity*, 22:1825–1839, 2005.

[31] J Abadie, B Abbott, R Abbott, M Abernathy, et al. Beating the spin-down limit on gravitational wave emission from the Vela pulsar. *Astropysical Journal*, 737(2):93, 2011.

[32] J Abadie, B Abbott, R Abbott, M Abernathy, et al. First search for gravitational waves from the youngest known neutron star. *Astrophysical Journal*, 722(2):1504–1513, 2010.

[33] B Abbott, R Abbott, R Adhikari, P Ajith, et al. Beating the spin-down limit on gravitational wave emission from the Crab pulsar. *The Astrophysical Journal Letters*, 683(1):L45, 2008.

[34] B Allen. The stochastic gravity-wave background: Sources and detection. In J-A Marck and J-P Lasota, editors, *Relativistic Gravitation and Gravitational Radiation*, page 373. Cambridge University Press, Cambridge, 1997.

[35] B Abbott, R Abbott, R Adhikari, J Agresti, et al. Searching for a stochastic background of gravitational waves with the laser interferometer gravitatiobal-wave observatory. *The Astrophysical Journal*, 659:918–930, 2007.

[36] G Steigman. Primordial nucleosynthesis in the precision cosmology era. *Annual Review of Nuclear and Particle Science*, 57:463–491, 2007.

[37] ME Gertsenshteĭn and VI Pustovoĭt. On the Detection of Low-Frequency Gravitational Waves. *Soviet Journal of Experimental and Theoretical Physics*, 16:433, 1963.

[38] FAE Pirani. On the physical significance of the riemann tensor. *Acta Physica Polonica*, 15:389, 1956.

[39] R Weiss. Electromagnetically Coupled Broadband Gravitational Antenna. Technical report, MIT, 1972.

[40] M Pitkin, S Reid, S Rowan, and J Hough. Gravitational Wave Detection by Interferometry (Ground and Space). *ArXiv e-prints*, 2011.

[41] RA Serway and JW Jewett. *Physics for Scientists and Engineers*. Cengage Learning, 2010.

[42] G Losurdo et al. Active control hierarchy in Virgo superattenuator: The role of the inverted pendulum. In E Coccia and G Veneziano and G Pizzella, editor, *Second Edoardo Amaldi Conference on Gravitational Wave Experiments*, page 334, 1998.

[43] J Winterflood and DG Blair. Ultra-Low Frequency Pre-Isolation in Three Dimensions. In E Coccia and G Veneziano and G Pizzella, editor, *Second Edoardo Amaldi Conference on Gravitational Wave Experiments*, page 485, 1998.

[44] MV Plissi, CI Torrie, ME Husman, NA Robertson, KA Strain, H Ward, H Lück, and J Hough. GEO 600 triple pendulum suspension system: Seismic isolation and control. *Review of Scientific Instruments*, 71:2539–2545, 2000.

[45] R Abbott, R Adhikari, G Allen, S Cowley, et al. Seismic isolation for Advanced LIGO. *Classical and Quantum Gravity*, 19(7):1591, 2002.

[46] R Spero. Prospects for ground based detectors of low frequency gravitational radiation. *AIP Conference Proceedings*, 96(1):347–350, 1983.

[47] SA Hughes and KS Thorne. Seismic gravity-gradient noise in interferometric gravitational-wave detectors. *Physical Review D*, 58:122002, 1998.

[48] M Beker, G Cella, R DeSalvo, M Doets, et al. Improving the sensitivity of future GW observatories in the 1–10Â Hz band: Newtonian and seismic noise. *General Relativity and Gravitation*, 43:623–656, 2011. 10.1007/s10714-010-1011-7.

[49] K Danzmann and A Rüdiger. LISA technology-concept, status, prospects. *Classical and Quantum Gravity*, 20(10):S1, 2003.

[50] S Hild, M Abernathy, F Acernese, P Amaro-Seoane, et al. Sensitivity studies for third-generation gravitational wave observatories. *Classical and Quantum Gravity*, 28(9):094013, 2011.

[51] A Nowick and B Berry. *Anelastic Relaxation in Crystalline Solids*. Academic Press, New York, 1972.

[52] WA Edelstein, J Hough, JR Pugh, and W Martin. Limits to the measurement of displacement in an interferometric gravitational radiation detector. *Journal of Physics E: Scientific Instruments*, 11(7):710, 1978.

[53] J Hough, H Walther, BF Schutz, J Ehlers, H Welling, IF Corbett, and V Kose. Proposal for a joint German-British interferometric gravitational wave detector. Technical report, Max-lanck-Insitut fur Quantenoptik Report, 1989.

[54] CM Caves. Quantum-mechanical radiation-pressure fluctuations in an interferometer. *Physical Review Letters*, 45:75–79, 1980.

[55] R Loudon. Quantum limit on the Michelson interferometer used for gravitational-wave detection. *Physical Review Letters*, 47:815–818, 1981.

[56] CM Caves. Quantum-mechanical noise in an interferometer. *Physical Review D*, 23:1693–1708, 1981.

[57] K McKenzie, DA Shaddock, DE McClelland, BC Buchler, and PK Lam. Experimental demonstration of a squeezing-enhanced power-recycled Michelson interferometer for gravitational wave detection. *Physical Review Letters*, 88:231102, 2002.

[58] H Billing, K Maischberger, A Rudiger, R Schilling, L Schnupp, and W Winkler. An argon laser interferometer for the detection of gravitational radiation. *Journal of Physics E: Scientific Instruments*, 12(11):1043, 1979.

[59] RWP Drever, GM Ford, J Hough, IM Kerr, AJ Munley, JR Pugh, NA Robertson, and H Ward. A Gravity-Wave Detector Using Optical Cavity Sensing. In E.Schmutzer, editor, *General Relativity and Gravitation 1980*, page 265, 1983.

[60] RWP Drever et al. Gravitational wave detectors using laser interferometers and optical cavities: Ideas, principles and prospects. In P Meystre and MO Scully, editors, *Quantum optics. Experimental gravity, and measurement theory*, NATO Advanced Science Institutes (ASI) Series B: Physics, Proceedings of the NATO Advanced Study Institute, held in Bad Windsheim, Germany, August 16-29, 1981. New York: Plenum Press, 1983.

[61] BJ Meers. Recycling in laser-interferometric gravitational-wave detectors. *Physical Review D*, 38:2317–2326, 1988.

[62] KA Strain and BJ Meers. Experimental demonstration of dual recycling for interferometric gravitational-wave detectors. *Physical Review Letters*, 66:1391–1394, 1991.

[63] G Heinzel, KA Strain, J Mizuno, KD Skeldon, B Willke, W Winkler, R Schilling, A Rüdiger, and K Danzmann. Experimental demonstration of a suspended dual recycling interferometer for gravitational wave detection. *Physical Review Letters*, 81:5493–5496, 1998.

[64] K Goda, O Miyakawa, EE Mikhailov, S Saraf, R Adhikari, K McKenzie, R Ward, S Vass, AJ Weinstein, and N Mavalvala. A quantum-enhanced prototype gravitational-wave detector. *Nature Physics*, 4:472–476, 2008.

[65] J Harms, Y Chen, S Chelkowski, A Franzen, H Vahlbruch, K Danzmann, and R Schnabel. Squeezed-input, optical-spring, signal-recycled gravitational-wave detectors. *Physical Review D*, 68:042001, 2003.

[66] H Vahlbruch, S Chelkowski, B Hage, A Franzen, K Danzmann, and R Schnabel. Coherent control of vacuum squeezing in the gravitational-wave detection band. *Physical Review Letters*, 97:011101, 2006.

[67] BP Abbott et al. LIGO: the Laser Interferometer Gravitational-Wave Observatory. *Reports on Progress in Physics*, 72(7):076901, 2009.

[68] J Giaime, P Saha, D Shoemaker, and L Sievers. A passive vibration isolation stack for LIGO: Design, modeling, and testing. *Review of Scientific Instruments*, 67(1):208 –214, 1996.

[69] GM Harry et al. Advanced LIGO: the next generation of gravitational wave detectors. *Classical and Quantum Gravity*, 27(8):084006, 2010.

[70] G Ballardin, L Bracci, S Braccini, C Bradaschia, et al. Measurement of the VIRGO superattenuator performance for seismic noise suppression. *Review of Scientific Instruments*, 72(9):3643–3652, 2001.

[71] F. Acernese et al. Advanced Virgo Baseline Design. Technical report, The Virgo Collaboration, 2009. Available from https://tds.ego-gw.it/itf/tds/file.php?callFile=VIR-0027A-09.pdf.

[72] The Virgo Collaboration. Advanced virgo baseline design, May 2009. note VIR-027A-09.

[73] H Grote and the LIGO Scientific Collaboration. The GEO 600 status. *Classical and Quantum Gravity*, 27(8):084003, 2010.

[74] Ryutaro Takahashi and the TAMA Collaboration. Status of TAMA300. *Classical and Quantum Gravity*, 21(5):S403, 2004.

[75] K Arai, R Takahashi, D Tatsumi, K Izumi, the CLIO Collaboration, and The LCGT Collaboration. Status of japanese gravitational wave detectors. *Classical and Quantum Gravity*, 26(20):204020, 2009.

[76] The ET Science Team. Einstein gravitational wave Telescope conceptual design study. `https://tds.ego-gw.it/ql/?c=7954`, December 2011.

[77] M Evans, S Ballmer, M Fejer, P Fritschel, G Harry, and G Ogin. Thermo-optic noise in coated mirrors for high-precision optical measurements. *Physical Review D*, 78:102003, 2008.

[78] R Brown. A Brief account of microscopical observations made in the months of June, July and August 1827 on the particles contained in the pollen of plants. 1828.

[79] A Einstein. Über die von der molekularkinetischen Theorie der Wärme geforderte Bewegung von in ruhenden Flüssigkeiten suspendierten Teilchen. *Annalen der Physik*, 322(8):549–560, 1905.

[80] Callen HB and RF Greene. On the theorem of irreversible thermodynamics. *Physical Review*, 86:702–710, 1952.

[81] PR Saulson. Thermal noise in mechanical experiments. *Physical Review D*, 42:2437–2445, 1990.

[82] CM Zener and S Siegel. Elasticity and anelasticity of metals. *The Journal of Physical and Colloid Chemistry*, 53(9):1468–1468, 1948.

[83] OL Anderson and HE Bömmel. Ultrasonic absorption in fused silica at low temperatures and high frequencies. *Journal of the American Ceramic Society*, 38(4):125–131, 1955.

[84] R. E. Strakna. Investigation of low-temperature ultrasonic absorption in fast-neutron irradiated Sio_2 glass. *Physical Review*, 123:2020–2026, 1961.

[85] D McLachlan Jr. and LL Chamberlain. Atomic vibrations and the melting process in metals. *Acta Metallurgica*, 12(5):571 – 576, 1964.

[86] MR Vukcevich. A new interpretation of the anomalous properties of vitreous silica. *Journal of Non-Crystalline Solids*, 11(1):25 – 63, 1972.

[87] J Reinisch and A Heuer. What Is Moving in Silica at 1 K? A Computer Study of the Low-Temperature Anomalies. *Physical Review Letters*, 95:155502, 2005.

[88] A Gillespie and F Raab. Thermally excited vibrations of the mirrors of laser interferometer gravitational-wave detectors. *Physical Review D*, 52:577–585, 1995.

[89] E Majorana and Y Ogawa. Mechanical thermal noise in coupled oscillators. *Physics Letters A*, 233(3):162 – 168, 1997.

[90] Y Levin. Internal thermal noise in the LIGO test masses: A direct approach. *Physical Review D*, 57(2):659–663, 1998.

[91] F Bondu, P Hello, and J-Y Vinet. Thermal noise in mirrors of interferometric gravitational wave antennas. *Physics Letters A*, 246(3-4):227 – 236, 1998.

[92] YT Liu and KS Thorne. Thermoelastic noise and homogeneous thermal noise in finite sized gravitational-wave test masses. *Physical Review D*, 62:122002, 2000.

[93] N Nakagawa, AM Gretarsson, EK Gustafson, and MM Fejer. Thermal noise in half-infinite mirrors with nonuniform loss: A slab of excess loss in a half-infinite mirror. *Physical Review D*, 65:102001, 2002.

[94] GM Harry et al. Thermal noise in interferometric gravitational wave detectors due to dielectric optical coatings. *Classical and Quantum Gravity*, 19(5):897, 2002.

[95] VB Braginsky and SP Vyatchanin. Thermodynamical fluctuations in optical mirror coatings. *Physics Letters A*, 312(3–4):244 – 255, 2003.

[96] MM Fejer, S Rowan, G Cagnoli, DRM Crooks, A Gretarsson, GM Harry, J Hough, SD Penn, PH Sneddon, and SP Vyatchanin. Thermoelastic dissipation in inhomogeneous media: loss measurements and displacement noise in coated test masses for interferometric gravitational wave detectors. *Physical Review D*, 70:082003, 2004.

[97] VB Braginsky, ML Gorodetsky, and SP Vyatchanin. Thermo-refractive noise in gravitational wave antennae. *Physics Letters A*, 271(5–6):303 – 307, 2000.

[98] Y Levin. Fluctuation–dissipation theorem for thermo-refractive noise. *Physics Letters A*, 372(12):1941 – 1944, 2008.

[99] B Mours, E Tournefier, and J-Y Vinet. Thermal noise reduction in interferometric gravitational wave antennas: using high order tem modes. *Classical and Quantum Gravity*, 23(20):5777, 2006.

[100] V Galdi, G Castaldi, V Pierro, IM Pinto, J Agresti, E D'Ambrosio, and R DeSalvo. Analytic structure of a family of hyperboloidal beams of potential interest for advanced LIGO. *Physical Review D*, 73:127101, 2006.

[101] S Chelkowski, S Hild, and A Freise. Prospects of higher-order Laguerre-Gauss modes in future gravitational wave detectors. *Physical Review D*, 79:122002, 2009.

[102] G Harry, TP Bodiya, and R DeSalvo. *Optical Coatings and Thermal Noise in Precision Measurement*. Optical Coatings and Thermal Noise in Precision Measurement. Cambridge University Press, 2012.

[103] SD Penn et al. Mechanical loss in tantala/silica dielectric mirror coatings. *Classical and Quantum Gravity*, 20(13):2917, 2003.

[104] DRM Crooks, G Cagnoli, MM Fejer, A Gretarsson, et al. Experimental measurements of coating mechanical loss factors. *Classical and Quantum Gravity*, 21(5):S1059, 2004.

[105] IW Martin et al. Measurements of a low-temperature mechanical dissipation peak in a single layer of Ta_2O_5 doped with TiO_2. *Classical and Quantum Gravity*, 25(5):055005, 2008.

[106] IW Martin, E Chalkley, R Nawrodt, H Armandula, et al. Comparison of the temperature dependence of the mechanical dissipation in thin films of ta_2o_5 and ta_2o_5 doped with tio_2. *Classical and Quantum Gravity*, 26(15):155012, 2009.

[107] VB Braginsky, VP Mitrofanov, and VI Panov. *Systems with Small Dissipation*. University of Chicago Press, Chicago, IL, 1985.

[108] HE Bömmel, WP Mason, and AW Warner. Dislocations, relaxations, and anelasticity of crystal quartz. *Physical Review*, 102(1):64–71, 1956.

[109] IW Martin, R Bassiri, R Nawrodt, MM Fejer, et al. Effect of heat treatment on mechanical dissipation in Ta_2O_5 coatings. *Classical and Quantum Gravity*, 27(22):225020, 2010.

[110] M Gross. CSIRO Report 1, Ion Beam Deposited Coatings. `https://dcc.ligo.org/public/0027/T040236/000/T040236-00.pdf`, May 2004. LIGO documnet LIGO-T040236-00-D.

[111] NW McLachlan. *Theory of Vibrations*. Dover, New York, NY, 1952.

[112] R Hull. *Properties of crystalline silicon*. EMIS datareviews series. INSPEC, the Institution of Electrical Engineers, 1999.

[113] DRM Crooks, P Sneddon, G Cagnoli, J Hough, S Rowan, MM Fejer, E Gustafson, R Route, N Nakagawa, D Coyne, GM Harry, and AM Gretarsson. Excess mechanical loss associated with dielectric mirror coatings on test masses in interferometric gravitational wave detectors. *Classical and Quantum Gravity*, 19(5):883, 2002.

[114] A Heptonstall, G Cagnoli, J Hough, and S Rowan. Characterisation of mechanical loss in synthetic fused silica ribbons. *Physics Letters A*, 354(5–6):353 – 359, 2006.

[115] S Reid, G Cagnoli, DRM Crooks, J Hough, P Murray, S Rowan, MM Fejer, R Route, and S Zappe. Mechanical dissipation in silicon flexures. *Physics Letters A*, 351:205–211, 2006.

[116] S Reid. *Studies of materials for future ground-based and space-based interferometric gravitational wave detectors*. PhD thesis, University of Glasgow, 2006.

[117] CSIRO. Australian Centre for Precision Optics. `http://www.acpo.csiro.au/coatingsindex.htm`, September 2010.

[118] S Chao, W-H Wang, M-Y Hsu, and L-C Wang. Characteristics of ion-beam-sputtered high-refractive-index tio2-sio2 mixed films. *Journal of the Optical Society of America A*, 16(6):1477–1483, 1999.

[119] RP Netterfield, M Gross, FN Baynes, KL Green, et al. Low mechanical loss coatings for LIGO optics: progress report. In M. L. Fulton and J. D. T. Kruschwitz, editors, *Society of Photo-Optical Instrumentation Engineers (SPIE) Conference Series*, volume 5870, pages 144–152, 2005.

[120] Mark Gross. Private Communication, 2008.

[121] J Wu and CC Yu. How stress can reduce dissipation in glasses. *Physical Review B*, 84:174109, 2011.

[122] BS Berry and WC Pritchet. Influence of the magnetomechanical pole-effect on the behavior of thin vibrating reeds. *Journal of Applied Physics*, 50(B3):1630–1632, 1979.

[123] A Čadež and A Abramovici. Measuring high mechanical quality factors of bodies made of bare insulating materials. *Journal of Physics E: Scientific Instruments*, 21(5):453, 1988.

[124] J Logan. *An Investigation of Some Mechanical and Optical Properties of Materials for Test Masses in Laser Interferometric Gravitational Wave Detectors*. PhD thesis, University of Glasgow, 1993.

[125] EH Putley and WH Mitchell. The electrical conductivity and hall effect of silicon. *Proceedings of the Physical Society*, 72(2):193, 1958.

[126] FJ Morin and JP Maita. Electrical properties of silicon containing arsenic and boron. *Physical Review*, 96:28–35, 1954.

[127] C Zener. Internal Friction in Solids. I. Theory of Internal Friction in Reeds. *Physical Review*, 52(3):230–235, 1937.

[128] C Zener. Internal Friction in Solids II. General Theory of Thermoelastic Internal Friction. *Physical Review*, 53(1):90–99, 1938.

[129] YS Touloukian and EH Buyco. *Thermophysical Properties of Matter, TPRC data series*. IFI/Plenum, New York, NY, 1970.

[130] CT Kuo, R Kwor, and KM Jones. Study of sputtered HfO_2 thin films on silicon. *Thin Solid Films*, 213:257–264, 1992.

[131] A Markosyan, R Route, H Armandula, and MM Fejer. PCI technique for thermal absorption measurements. `https://dcc.ligo.org/public/0037/G080315/000/G080315-00.pdf`, May 2008. LIGO document LIGO-G080315-00-Z.

[132] SV Ushakov et al. Crystallization in hafnia- and zirconia-based systems. *Physica status solidi (b)*, 241(10):2268–2278, 2004.

[133] R Bassiri. *The atomic structure and properties of mirror coatings for use in gravitational wave detectors*. PhD thesis, University of Glasgow, 2011.

[134] WJ Zhu, T Tamagawa, M Gibson, Furukawa T, and TP Ma. Effect of Al inclusion in HfO_2 on the physical and electrical properties of the dialectrics. *IEEE Electron Device Letters*, 23(11), 2002.

[135] GM Harry, MR Abernathy, AE Becerra-Toledo, H Armandula, et al. Titania-doped tantala/silica coatings for gravitational-wave detection. *Classical and Quantum Gravity*, 24(2):405, 2007.

[136] WC Oliver and GM Pharr. An improved technique for determining hardness and elastic modulus using load and displacement sensing indentation experiments. *Journal of Materials Research*, 7(06):1564–1583, 1992.

[137] J Menčík, D Munz, E Quandt, ER Weppelmann, and MV Swain. Determination of elastic modulus of thin layers using nanoindentation. *Journal of Materials Research*, 12(09):2475–2484, 1997.

[138] SJ Bull. Nanoindentation of coatings. *Journal of Physics D: Applied Physics*, 38(24):R393, 2005.

[139] NA Burnham, RJ Colton, and HM Pollock. Interpretation issues in force microscopy. *Journal of Vacuum Science & Technology A: Vacuum, Surfaces, and Films*, 9(4):2548–2556, 1991.

[140] AC Fischer-Cripps. Critical review of analysis and interpretation of nanoindentation test data. *Surface and Coatings Technology*, 200:4153 – 4165, 2006.

[141] M Oyen. *Ultrastructural Characterization of Time-Dependent, Imhomogeneous Materials and Tissues*. PhD thesis, University of Minnesota, 2005.

[142] J Gubicza, A Juhász, P Arató, P Szommer, P Tasnádi, and G Vörös. Elastic modulus determination from depth sensing indentation testing. *Journal of Materials Science Letters*, 15:2141–2144, 1996.

[143] N Panich and S Yong. Improved method to determine the hardness and elastic moduli using nano-indentation. *KMITL Science Journal*, 5(2):483–492, 2005.

[144] WC Oliver and GM Pharr. Measurement of hardness and elastic modulus by instrumented indentation: Advances in understanding and refinements to methodology. *Journal of Materials Research*, 19(01):3–20, 2004.

[145] R Saha and WD Nix. Effects of the substrate on the determination of thin film mechanical properties by nanoindentation. *Acta Materialia*, 50(1):23 – 38, 2002.

[146] H Gao, C-H Chiu, and J Lee. Elastic contact versus indentation modeling of multi-layered materials. *International Journal of Solids and Structures*, 29(20):2471 – 2492, 1992.

[147] H Song. *Selected Mechanical Problems in Load and Depth Sensing Indentation Testing*. PhD thesis, Rice University, 1999.

[148] A Rar, H Song, and GM Pharr. Assessment of new relation for the elastic compliance of a film-substrate system. *MRS Online Proceedings Library*, 695:L10.10.1, 2001.

[149] M Oyen. Personal Communication, 2011.

[150] T Hanada, Y Bessyo, and N Soga. Elastic constants of amorphous thin films in the systems SiO_2-Al_2O_3 and $AlPO_4$-Al_2O_3. *Journal of Non-Crystalline Solids*, 113(2-3):213 – 220, 1989.

[151] T Hanada, T Shinoda, S Tanabe, and N Soga. Preparation and elastic properties of rf-sputtered amorphous films in the system SiO_2-Y_2O_3. *Journal of the American Ceramic Society*, 78(5):1383–1386, 1995.

[152] Heraeus. Quartz glass for optics: Data and properties. Heraeus internal document, includes mechanical properties of Suprasil-family silica produced by Heraeus.

[153] JE Klemberg-Sapieha, J Oberste-Berghaus, L Martinu, R Blacker, et al. Mechanical characteristics of optical coatings prepared by various techniques: A comparative study. *Applied Optics*, 43(13):2670–2679, 2004.

[154] C Chaneliere, JL Autran, RAB Devine, and B Balland. Tantalum pentoxide (Ta2O5) thin films for advanced dielectric applications. *Materials Science and Engineering: R: Reports*, 22(6):269 – 322, 1998.

[155] E Çetinörgü, B Baloukas, O Zabeida, JE Klemberg-Sapieha, and L Martinu. Mechanical and thermoelastic characteristics of optical thin films deposited by dual ion beam sputtering. *Applied Optics*, 48(23):4536–4544, 2009.

[156] J Hay. Measuring substrate-independent young's modulus. Technical report, Agilent Technologies, 2010. `http://www.nano-tm-agilent.com/nano_data_sheets/AN-MeasSubsIndp_5990-6507EN.PQ.pdf`.

[157] S Mato, G Alcalá, P Skeldon, GE Thompson, AB Mann, D Masheder, H Habazaki, and K Shimizu. Dielectric and mechanical properties of anodic films in the Ta–Ti system. *Surface and Interface Analysis*, 35(5):477–482, 2003.

[158] Y Gaillard, VJ Rico, E Jimenez-Pique, and AR González-Elipe. Nanoindentation of TiO2 thin films with different microstructures. *Journal of Physics D: Applied Physics*, 42(14):145305, 2009.

[159] P Frach, D Glöß, K Goedicke, M Fahland, and W-M Gnehr. High rate deposition of insulating TiO2 and conducting ITO films for optical and display applications. *Thin Solid Films*, 445(2):251 – 258, 2003. <ce:title>Proceedings of the 3rd International Symposium on Transparent Oxide Thin films for Electronics and Optics</ce:title>.

[160] K-R Wu, C-H Ting, J-J Wang, W-C Liu, and C-H Lin. Characteristics of graded TiO2 and TiO2/ITO films prepared by twin DC magnetron sputtering technique. *Surface and Coatings Technology*, 200(20–21):6030 – 6036, 2006.

[161] A Bendavid, PJ Martin, and H Takikawa. Deposition and modification of titanium dioxide thin films by filtered arc deposition. *Thin Solid Films*, 360(1–2):241 – 249, 2000.

[162] K Kurosaki, D Setoyama, J Matsunaga, and S Yamanaka. Nanoindentation tests for TiO2, MgO, and YSZ single crystals. *Journal of Alloys and Compounds*, 386(1–2):261 – 264, 2005.

[163] R Kuschnereit, H Fath, AA Kolomenskii, M Szabadi, and P Hess. Mechanical and elastic properties of amorphous hydrogenated silicon films studied by broadband surface acoustic wave spectroscopy. *Applied Physics A: Materials Science & Processing*, 61:269–276, 1995.

[164] P Hess. Laser diagnostics of mechanical and elastic properties of silicon and carbon films. *Applied Surface Science*, 106(0):429 – 437, 1996. <ce:title>Proceedings of the Second International Conference on Photo-Excited Processes and Applications</ce:title>.

[165] Jr. MM de Lima, RG Lacerda, J Vilcarromero, and FC Marques. Coefficient of thermal expansion and elastic modulus of thin films. *Journal of Applied Physics*, 86(9):4936–4942, 1999.

[166] SL Dole, O Hunter Jr., and CJ Wooge. Elastic properties of monoclinic hafnium oxide at room temperature. *Journal of the American Ceramic Society*, 60(11-12):488–490, 1977.

[167] R Thielsch, A Gatto, and N Kaiser. Mechanical stress and thermal-elastic

properties of oxide coatings for use in the deep-ultraviolet spectral region. *Applied Optics*, 41(16):3211–3217, 2002.

[168] JP Watt, GF Davies, and RJ O'Connell. The elastic properties of composite materials. *Review of Geophysics*, 14(4):541–563, 1976.

[169] D Rousselle, A Berthault, O Acher, JP Bouchaud, and PG Zerah. Effective medium at finite frequency: Theory and experiment. *Journal of Applied Physics*, 74(1):475–479, 1993.

[170] GG Stoney. The tension of metallic films deposited by electrolysis. *Proceedings of the Royal Society of London A*, 82:172–175, 1909.

[171] MF Doerner and WD Nix. Stresses and deformation processes in thin films on substrates. *Critical Reviews in Solid State and Materials Sciences*, 14(3):225–268, 1988.

[172] RW Hoffman. The mechanical properties of thin condensed films. In *Physics of Thin Films*, volume 3. Academic, 1966.

[173] MM de Lima Jr., RG Lacerda, J Vilcarromero, and FC Marques. Coefficient of thermal expansion and elastic modulus of thin films. *Journal of Applied Physics*, 86:4936–4942, 1999.

[174] YW Bae, WY Lee, and DP Stinton. Effects of temperature and reagent concentration on the morphology of chemically vapor deposited β-ta2o5. *Journal of the American Ceramic Society*, 78(5):1297–1300, 1995.

[175] S Wu, H Chan, and M Harmer. Compositional tailoring of the thermal expansion coefficient of tantalum (v) oxide. *Journal of Materials Science*, 41:689–695, 2006.

[176] AR Ruffa. Thermal expansion in insulating materials. *Journal of Materials Science*, 15:2258–2267, 1980.

[177] KVK Rao, SVN Naidu, and L Iyengar. Thermal expansion of rutile and anatase. *Journal of the American Ceramic Society*, 53(3):124–126, 1970.

[178] U Diebold. The surface science of titanium dioxide. *Surface Science Reports*, 48(5–8):53 – 229, 2003.

[179] B Ohnysty and FK Rose. Thermal expansion measurements on thoria and hafnia to 4500° F. *Journal of the American Ceramic Society*, 47(8):398–400, 1964.

[180] CE Curtis, LM Doney, and JR Johnson. Some properties of hafnium oxide, hafnium silicate, calcium hafnate, and hafnium carbide. *Journal of the American Ceramic Society*, 37(10):458–465, 1954.

[181] A Cumming, R Jones, M Barton, G Cagnoli, et al. Apparatus for dimensional characterization of fused silica fibers for the suspensions of advanced gravitational wave detectors. *Review of Scientific Instruments*, 82(4):044502, 2011.

[182] G Mills. Private Communication, 2010.